Journal of South American Earth Sciences 93 (2019) 313–347

Contents lists available at ScienceDirect

Journal of South American Earth Sciences

journal homepage: www.elsevier.com/locate/jsames

Las Cañas plutonic complex: Geodynamic implications during the Famatinian magmatism in northeast of Sierra de San Luis, Argentina

Augusto Morosini[a,b,*], Eliel Enriquez[a,b], Diego Pagano[a], Brian Orozco[a], José Ulacco[a], Alina Tibaldi[b,c], Eber Cristofolini[b,c], Brian Muñoz[a,b], Ariel Ortiz Suárez[a], Verónica Montenegro[b,d], Eloy Sánchez[b,e], Franco Icazatti[a], Raúl Gil[b,f], Esteban Crespo[b,g], Gabriel Ramos[a]

[a] Departamento de Geología, Universidad Nacional de San Luis, Argentina
[b] Consejo Nacional de Investigaciones Científicas y Técnicas (CONICET), Argentina
[c] Departamento de Geología, Universidad Nacional de Río Cuarto, Argentina
[d] Instituto de Investigación en Paleobiología y Geología, Universidad Nacional de Río Negro, Argentina
[e] Departamento de Física, Universidad Nacional de San Luis, Argentina
[f] Departamento de Química, Universidad Nacional de San Luis, Argentina
[g] Departamento de Bioquímica y Cs. Biológicas, Universidad Nacional de San Luis, Argentina

ARTICLE INFO

Keywords:
Petrology
Geochemical process
P-T conditions
Geochronology
Famatinian orogeny

ABSTRACT

Las Cañas Plutonic Complex (LCPC) is a small representative of the Famatinian Ordovician plutonism (470.4 ± 8.1 Ma) located in the northeastern sector of Sierra Grande de San Luis, Argentina. The LCPC was emplaced into a metasedimentary sequence, which reached their metamorphic climax under high-temperature/low-pressure conditions (~680 ± 37 °C and 550 ± 120 MPa). The bodies of the LCPC are zoned by rocks of different compositions that represent ultrabasic, basic, intermediate and acidic trends (hornblendites, gabbros, tonalites, and granodiorites). Their petrological, mineralogical and geochemical characteristics indicate that multiple processes formed them, mainly crystal fractionation of magnesian, calc-alkaline and metaluminous magmas (typical of arc), but also different assimilation degrees of crustal melts from the fusion of metawackes involving AFC processes. Fieldwork (structural and petrological data), the geochemical characteristics of rocks [eg. Low Sr/Y and $(Gd/Yb)_{C-N}$], and thermobarometric results, indicate a relatively shallow fractionalization for the LCPC, which is in line with a pre-collisional arc stage linked to an extensive retro-arc setting for the Famatinian orogeny in Sierra de San Luis.

1. Introduction

Las Cañas mafic-ultramafic intrusive (Ortiz Suárez et al., 2001, 2012) is part of a group of plutons so-called *"Las Cañas Plutonic Complex"* (LCPC). This complex is located on the northeastern part of the Sierra Grande de San Luis (32°33′38″S, 65°24′53.40″W) close to Concarán (San Luis province, Argentina) (Fig. 1a). The LCPC is hosted in a metasedimentary basement corresponding to Conlara Metamorphic Complex (Sims et al., 1998; Sato et al., 2003). Here the metamorphic basement is mainly composed of biotite-quartz schists, locally equivalent to Las Aguadas Metamorphic Complex (Ortiz Suárez, 1988), and of gneisses and migmatites (metatexites and diatexites), whose protoliths seem to be the previously mentioned schists.

Within the Sierra de San Luis, there are many types of plutonic rocks as mafic-ultramafic bodies, tonalitic plutons and acidic intrusives (granodiorites, granites, and pegmatites) which have been related to Famatinian orogeny (Llambías et al., 1998; von Gosen et al., 2002; Sato et al., 2003; Brogioni et al., 2005; López de Luchi et al., 2007; Morosini et al., 2017).

So far, there is no consensus regarding the processes that gave rise to the mafic-ultramafic rocks (e.g. La Jovita-Las Águilas mafic-ultramafic complex) and the intermediate and acidic rocks (tonalitic, granodioritic and granitic plutons), being considered to be related to different times and tectonic settings (Brogioni, 1994; Hauzenberger et al., 2001; Sato et al., 2003; Steenken et al., 2011, Ferracutti et al., 2017, among others). However, new insight from LCPC opens the possibility to link the magmatism associated with the three compositional types of intrusive rocks (basic-ultrabasic, intermediate and acidic), showing a clear interaction between them. Thus, Las Cañas Plutonic Complex (LCPC) could be a key element to understand and reveal the evolution

* Corresponding author. Departamento de Geología, Universidad Nacional de San Luis Ejército de los Andes 950, San Luis, CP: 5700, Argentina.
E-mail address: afmorosi@unsl.edu.ar (A. Morosini).

https://doi.org/10.1016/j.jsames.2019.04.028
Received 16 September 2018; Received in revised form 30 April 2019; Accepted 30 April 2019
Available online 08 May 2019
0895-9811/ © 2019 Elsevier Ltd. All rights reserved.

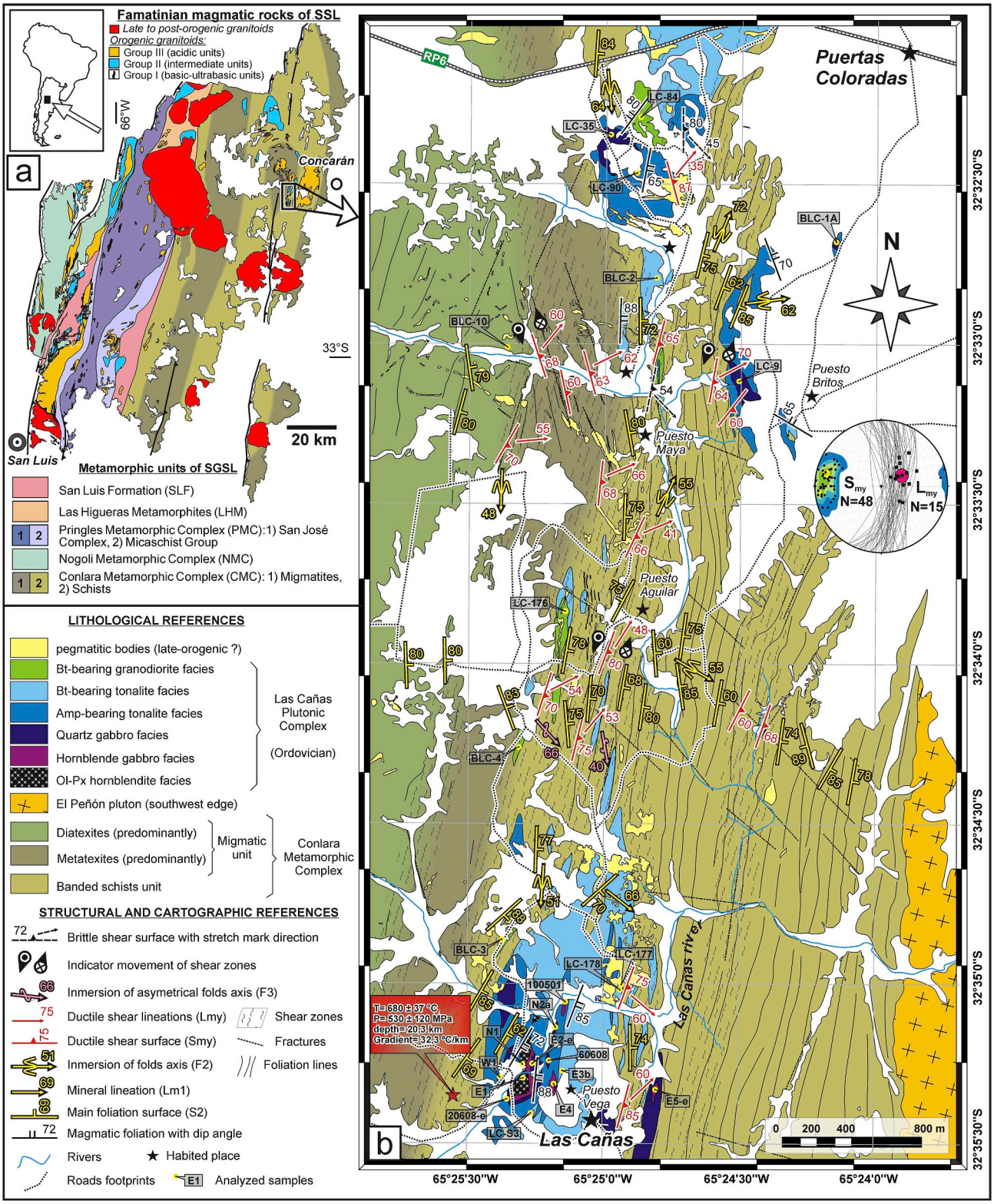

Fig. 1. a) Geological map of the Sierra de San Luis (Morosini et al., 2017) with location of studied area. b) Geological-structural map of LCPC. In stereographic representation (lower hemisphere) S_{my} are poles to plane of shears, L_{my} correspond to stretching lineations in shear zones.

involved in the generation of the different magmatic rocks related to the Famatinian orogeny in Sierra de San Luis.

In order to explain the context in which the LCPC was emplaced and to elucidate the processes that originated it, this paper analyzes the field relationships, petrography, mineral chemistry and whole-rock compositions of the different units. U–Pb laser-ablation quadrupole inductively coupled plasma mass spectrometry (LA-Q-ICPMS) zircon age was determined in one of the most characteristic facies of the LCPC, which allows its connection to other rock types in a regional tectonic context. We also compared the geochemical signature of the studied rocks with the rocks from the deeper Famatinian arc exposed in Sierra de Valle Fértil-La Huerta (Otamendi et al., 2009), as well as with other

magmatic rocks present in Sierra de San Luis (Brogioni et al., 2005; López de Luchi et al., 2007; Morosini, 2011; among others). Finally, we present a new model of interaction between the different types of magmatic rocks in the Ordovician of the Sierra de San Luis.

2. Geological background

The Famatinian magmatic arc, located in the Eastern Sierras Pampeanas, Famatina, Puna and Cordillera Oriental (Argentina), has been object of many studies (Rapela et al., 1992; Pankhurst et al., 1998; Bahlburg, 1998; Coira et al., 1999; Lucassen and Franz, 2005; Otamendi et al., 2009, 2012; Ducea et al., 2010, 2015; Tibaldi et al., 2013; Cristofolini et al., 2014; Morosini et al., 2017). This magmatic arc extends for about 1500 km, being fragmented by tectonic deformation into distinct segments. The magmatic activity of this arc was shut off due to the collision of a Laurentia-derived microcontinent, called either Precodillera or Cuyania (Thomas and Astini, 1996; Ramos, 2004). The collision and its related mountain building stage (ca. 460–400 Ma) that shut off the Famatinian arc, also uplifted, tilted and unroofed the plutonic crust that had built up during the Early and Middle Ordovician (Astini and Dávila, 2004; Collo et al., 2009; Mulcahy et al., 2014; Cristofolini et al., 2014; Thomas et al., 2015). For this reason, it is currently possible to observe a notable change in petrological conditions across the exposed paleo-depths at about 28° S latitude (Lucassen and Franz, 2005; Otamendi et al., 2010). Nowadays, the Sierra de Valle Fértil-La Huerta represents the deepest crustal part of the Famatinian magmatic arc (Otamendi et al., 2008; Tibaldi et al., 2013), while within the Puna region (Coira et al., 1999, 2009; Poma et al., 2004; Kleine et al., 2004; Viramonte et al., 2007) and in the Famatina mountain system (Mannheim and Miller, 1996; Cisterna and Coira, 2014; Armas et al., 2018) shallower plutonic and eruptive igneous rocks are interbedded with sedimentary rocks.

Ducea et al. (2015) interpreted that the Famatinian arc was active in flare-up mode, for a relatively short period of time (~20 Myr), and that it was formed by a combination of subarc mantle-derived gabbroic magmas and melt-fertile suite generated from metasedimentary materials, affirming that there is no evidence for the existence of a cratonic lower crust. The sedimentary sequence (over which the deeper Famatinian arc developed) was deposited during Middle and Upper Cambrian, in a marine marginal-basin (Cristofolini et al., 2012); although it could also involve part of the previously passive-margin basin (Ducea et al., 2015) regionally known as Puncoviscana Formation (Turner, 1960; Aceñolaza and Aceñolaza, 2005) and their high-grade equivalents.

The Sierra de San Luis (SSL) located in the southwestern sector of Eastern Sierras Pampeanas (Caminos, 1979) is considered part of the Famatinian orogen. However, contrary to the geology preserved to the northwest, in the typical arc sections (e.g. Sierras de Valle Fértil, Ulapes, Chepes, etc), the SSL is dominated by metamorphic rocks, where only about 20% is composed of plutonic rocks (Ortiz Suárez et al., 1992; Llambías et al., 1998; Sato et al., 2003; Brogioni et al., 2005; López de Luchi et al., 2007). Mainly SSL's metamorphic basement has been divided into three principal NNE trending metamorphic complexes, named Nogolí (NMC), Pringles (PMC), and Conlara (CMC) (Sims et al., 1998), which are separated by two narrow low-grade metamorphic belts, named by Prozzi and Ramos (1988) as San Luis Formation (SLF) (Fig. 1a). The NMC, PMC and SLF have Cambrian sedimentation ages, between 530 and 510 Ma (Sims et al., 1998; Steenken et al., 2006, Drobe et al., 2009, 2011), whereas in the CMC, the depositional age of the sedimentary protoliths was determined in ~580 Ma (Drobe et al., 2009) and ~550 Ma (Rapela et al., 2015).

The CMC (host rock of the Las Cañas Plutonic Complex) is mainly composed of biotite-quartz schists, gneisses, and migmatites, and in some places outcropping tourmalinites, calc-silicate rocks and amphibolites, that are related to tungsten mineralizations (López de Luchi et al., 2003, and reference therein). Also, in the CMC, numerous pegmatitic bodies of varying dimensions (1–200 m in width) that are part of the Conlara Pegmatitic District (Rossi, 1966) are common.

The predominant schists of CMC could be part of the "banded schists", which have a broad regional distribution in the Eastern Sierras Pampeanas and would be an early equivalent of the Puncoviscana Formation developed in the NW region of Argentina (Martino et al., 2009; Drobe et al., 2009; at references therein).

There is no clear polimetamorphism occurrence within the CMC, and so far only two ages have been identified (which are very different between them) to define the age of the metamorphic climax. On the one hand, Siegesmund et al. (2010) indicated an Ediacaran age of 564 ± 21 Ma (stepwise leaching Pb/Pb-garnet), while on the other hand Famatinian ages of 482 to 470 Ma (U/Pb-monazite) were mentioned by Whitmeyer and Simpson (2004). According to Baldo et al. (2014) all the ages older than 550 Ma determined on zircons of metasedimentary rocks in the neighboring Sierras de Córdoba should be interpreted as the fraction of the protolith, and not as metamorphic ages. Considering this, the Famatinian ages reported by Whitmeyer and Simpson (2004) for the metamorphism of the CMC are more reliable; although it should be noted that these ages cannot be reproduced because the authors did not publish the isotopic analysis data.

The plutonic rocks present in the SSL correspond to two Paleozoic magmatic events: 1) the Ordovician orogenic magmatism associated with the Famatinian arc development, and 2) the Devonian post-orogenic magmatism, which is associated with a stage of erosion and post-collisional exhumation (Morosini et al., 2017 and references therein). The orogenic plutons are more numerous, but cover a minor area than the post-orogenic products (less than ~35%) and, in general, they are differentiated morphologically by their higher aspect ratios and internal structure (Fig. 1a).

The Ordovician orogenic magmatism from SSL is composed of three main groups of plutonic rocks (Morosini and Ortiz Suárez, 2015) separated accordingly to their main petrological, compositional and field relationships: Group I (basic to ultrabasic units), Group II (intermediate units), and Group III (acidic units) (Fig. 1a).

Group I is composed of: a) gabbro bodies containing minor cumulate rocks (hornblendites, pyroxenites, peridotites and dunites), that are located within the PMC along a N–S trending strip called La Jovita-Las Águilas mafic-ultramafic complex (Brogioni, 1994; Mogessie et al., 2000; Sato et al., 2003; Ferracutti et al., 2007); b) Amp-rich gabbros to hornblendites (partially metamorphosed) located in a N–S strip within the NMC (Carugno Durán, 1998; González et al., 2002, 2004; Sato et al., 2003; Morosini, 2011); and c) gabbros associated with ultramafic rocks in the Las Cañas body (Ortiz Suárez et al., 2001, 2012) located in the northeast of CMC.

Group II is represented by plutons with intermediate composition, predominantly tonalites, and to a lesser extent, by cogenetic diorites or quartz-gabbros that are intruded in all the metamorphic units of the SSL (Sato et al., 1996; Brogioni et al., 2005; Morosini, 2011). In general, they are calc-alkaline (I-type) rocks, metaluminous to weakly peraluminous, typical of magmatic arc rocks (Sato et al., 1996; Llambías et al., 1998). There is a spatial, and probably a genetic link between groups I and II, but these relationships are still unknown and subject of new studies.

Group III involves all the acidic units: granitic and granodioritic plutons, aplo-pegmatites and dikes with relict-volcanic texture metamorphosed into a low-grade (metadacites to metariodacites). Geochemically, the group III presents peraluminous (S-type) calc-alkaline tendencies with variations in the source, from pure sedimentary to mixed with both igneous and crustal metasedimentary protholits (e.g. Brogioni et al., 2005; López de Luchi et al., 2007).

The importance of the study of the LCPC is based on that allows distinguishing the three groups mentioned above, and understanding the relationships and processes that occurred between them as will be discussed in the following sections.

Table 1
Temperatures and pressures calculated for the LCPC facies.

facies	Ol-Px hornblendite	Hornblendegabbro	Quartz gabbro	Amp-bearing tonalite		Bt-bearing granodiorite
sample	N1	100501	N2a	60608	20608	LC-176
1) T (°C)	971 ± 39	956 ± 35	932 ± 36	967 ± 40	891 ± 67	–
2) T (°C)	974 ± 56	947 ± 56	914 ± 56	911 ± 22	870 ± 56	–
3) T (°C)	–	963 ± 7	854 ± 5	794 ± 3	738 ± 1	–
4) T (°C)	–	–	–	–	–	690 ± 0.1
2) P (MPa)	–	–	–	457 ± 114	432 ± 108	–

1) Amp thermometer (Putirka, 2016).
2) Amp-TB geothermobarometer (Ridolfi et al., 2010).
3) Hornblende-Plagioclase geothermometer (Holland and Blundy, 1994) based on (Ed-Tr). The temperature and standard deviations were calculated based on the pressure and standard deviation calculated in the metamorphic host rocks (550 ± 120 MPa).
4) Two-feldspar geothermometer (Whitney and Stormer, 1977).

3. Methodology

This paper results from a petrological and structural analysis. Thin sections were petrographically described from which modal compositions were obtained with a manual point counter using 1000 points per thin section (Table A1). Rock classification was based on the IUGS diagram (Le Maitre, 2002), and abbreviations for names of rock-forming minerals follow to Whitney and Evans (2010).

Selected thin sections were analyzed in a JEOL JXA-8230 electron microprobe (WDS mode), in LAMARX (Universidad Nacional de Córdoba, Argentina). Analytical conditions corresponded to 15 kV of acceleration potential, 20 nA of beam current, 1–5 μm beam diameter, and a counting time of 10 s peak/5 s background. The used patterns were a combination of silicates and oxides, and the ZAF correction model (JEOL suite) was applied. A LEO 1450-VP scanning electron microscope was also used with the energy dispersive x-ray spectrometer (EDS) EDAX Genesis 2000, in LABMEM (Universidad Nacional de San Luis). The analytical conditions were 15 kV of acceleration potential, 0.606 nA of beam current, and 200 s of live counting time. The used patterns, in this case, were a combination of silicates and oxides, and the PhiZAF correction model (EDAX software) was applied. The microanalyses are presented as supplementary data in Table A2.

Amphibole formulae (including Fe^{3+}/Fe^{2+}) were calculated with the Excel spreadsheet of Locock (2014). Amphiboles were classified following the IMA recommendations (Hawthorne et al., 2012), with the AMPH 2012 2.0 software (Oberti et al., 2012). Formulae and Fe^{3+}/Fe^{2+} for olivine and clinopyroxene were calculated with the Excel spreadsheet downloaded from http://serc.carleton.edu/research_education/index.html.

Mineral chemistry was used in order to obtain P-T conditions in a metamorphic sample. We used the free TC-Comb© v1.1 platform (Dolivo-Dobrovolsky, 2015), which integrates THERMOCALC® software (Powell and Holland, 1988), with the thermodynamic database of Holland and Powell (1998), AX2 (Holland TJB software) for mineral activity calculations, and TriQuick© MS Windows software (Dolivo-Dobrowolsky, 2012–2013), for the graphical output of the results. Also, thermo-barometers (Putirka, 2016; Ridolfi et al., 2010; Holland and Blundy, 1994; Whitney and Stormer, 1977) were used to determine the crystallization temperatures of some samples of plutonic rocks.

Whole-rock analyses were performed in three laboratories: 1) mayor and trace elements in Activation Laboratories (Actlabs, Canada); rock powders were fused using a mixture of Li meta and tetraborate, dissolved in nitric acid and then analyzed by ICP-OES and ICP-MS; 2) major and trace elements in Departamento de Geología y Minería (Universidad Nacional de Jujuy) through XRF spectrometry; rock powders were fused using Li tetraborate for major elements, while for the trace elements the samples were mixed with methyl methacrylate in a solution with 10% acetone (1 ml per 3 g of sample) and pressed at 20 t/in2; and 3) trace elements (including REE) in the Laboratorio de Espectrometría de Masas (INQUISAL - Universidad Nacional de San Luis, Argentina); rock powders were digested in a microwave oven using a mixture of hydrochloric and hydrofluoric acids in 18:1 vol ratio and then analyzed by ICP-MS. In the three laboratories a sample with known concentrations of major and trace elements was analyzed, which allowed corroborating the good quality of the results.

The absolute age was determined by LA-Q-ICPMS U/Pb zircon method from the Amp-bearing tonalite facies (sample LC-90), located in the north zone of LCPC (S32°32′29.83" - W65°24′46.51″). Zircons concentration and mounting were performed at the technical laboratory of the Departamento de Geología de la Universidad Nacional de San Luis, and they were observed under electron microscopy; backscattered electron images of the zircons were obtained in an LEO 1450VP scanning electron microscope (LABMEM - Universidad Nacional de San Luis).

Analyses of zircons were conducted at the SGIker-Geochronology and Isotope Geochemistry Facility of the University of the Basque Country (Spain). The samples were ablated with a 213 nm Nd: YAG based laser ablation system (NewWave Research) coupled to a Thermo Fisher iCAP Qc quadrupole based ICP-MS instrument with enhanced sensitivity through a dual pumping system. Analytical conditions are spot diameters of 30 μm associated with repetition rates of 10 Hz and laser fluence at the target of ca. 5.5 J/cm^2. The ablated material was carried into helium, then mixed with argon and stabilized with a smoothing device (Tunheng and Hirata, 2004) before injection into the plasma source. The signals of ^{202}Hg, ^{204}(Pb + Hg), ^{206}Pb, ^{207}Pb, ^{208}Pb, ^{232}Th, and ^{238}U masses were acquired. The occurrence of common Pb in the samples was monitored by the evolution of ^{204}(Pb + Hg) signal intensity. Single analyses consisted of 25 s of background integration with the laser off followed by 45 s integration with the laser firing and a 30 s delay to wash out the previous sample (ca. 10 s for 6 orders of magnitude) to prepare the next analysis. Data reduction was carried out with Iolite v. 3.32 (Paton et al., 2011) and VizualAge (Petrus and Kamber, 2012) using GJ-1 zircon standard (Jackson et al., 2004) for calibration and Plešovice zircon (Sláma et al., 2008) as secondary standard (Table A3 and Fig. A1). For each analysis, the time-resolved signal of single isotopes and isotope ratios were monitored and carefully inspected to verify the presence of perturbations related to inclusions, fractures, mixing of different age domains or common Pb. The concentrations of U–Th–Pb were calibrated relative to the certified contents of GJ-1 zircon standard (Jackson et al., 2004). Percentage concordance was calculated as [(^{206}Pb/^{238}U age)/(^{207}Pb/^{206}Pb age)] × 100 (Meinhold et al., 2010). The analysis representations were carried out using Isoplot/Excel (Ludwig, 2003).

Table 2
LA-Q-ICPMS U/Pb-zircon data for Amp-bearing tonalite facies (sample LC-90).

Spot name	Elemental concentration				Isotopes ratios for Tera-Wasserburg plot					Isotopes ratios for Wetherilll plot		
	U (ppm)	Th (ppm)	Pb (ppm)	Th/U	$^{238}U/^{206}Pb$	2s (abs)	$^{207}Pb/^{206}Pb$	2s (abs)	Rho	$^{207}Pb/^{235}U$	2s (abs)	$^{206}Pb/^{238}U$
Data used for crystallization age (emplacement) = concordance A > 95% and concordance B > 84%												
1n	172	120	174	0.70	12.887	0.332	0.059	0.003	0.327	0.641	0.03	0.078
5	179	131	204	0.73	12.937	0.285	0.057	0.003	−0.052	0.615	0.032	0.077
7b	81.1	50.4	74.9	0.62	13.459	0.272	0.057	0.003	0.237	0.593	0.035	0.074
10	118.7	78.1	124.4	0.66	13.263	0.264	0.057	0.003	−0.153	0.574	0.025	0.075
12b	57.8	33.4	54.1	0.58	13.263	0.246	0.058	0.004	0.259	0.585	0.034	0.075
13n	131.5	96.2	175	0.73	12.837	0.231	0.057	0.003	−0.098	0.623	0.035	0.078
13b	240	154	234	0.64	13.661	0.299	0.057	0.003	0.383	0.581	0.032	0.073
15a	164.7	217	303	1.32	13.514	0.201	0.058	0.002	0.290	0.595	0.02	0.074
17a-SP	90.8	69.7	111.2	0.77	13.141	0.466	0.058	0.005	0.049	0.606	0.056	0.076
Ages data of inherited cores (source) = concordance A > 94% and concordance B > 80%												
8	318	110.6	308	0.35	6.925	0.110	0.072	0.002	0.365	1.459	0.047	0.144
8-SP	210	156	307	0.74	9.311	0.616	0.065	0.004	0.461	0.899	0.078	0.107
11	293	125.8	233	0.43	11.641	0.230	0.061	0.002	0.024	0.711	0.028	0.086
14a	422	86	237.5	0.20	6.618	0.136	0.073	0.002	0.347	1.53	0.042	0.151
17a	255	284	688	1.11	6.640	0.172	0.071	0.003	0.314	1.46	0.068	0.151
Younger ages representing loss Pb (interpreted as hydrothermal alteration) = concordance A > 93% and concordance B < 85%												
6b	254.7	146.6	206.1	0.58	14.225	0.283	0.058	0.003	0.090	0.564	0.027	0.070
7c	198.9	122.2	165.2	0.61	14.225	0.304	0.060	0.003	0.432	0.582	0.029	0.070
14b	135.3	68.2	96	0.50	14.124	0.219	0.058	0.002	0.167	0.57	0.023	0.071
Discordant ages not considered in the plots = concordance A < 96% and concordance B < < 69%												
1b	193.5	99.2	204	0.51	12.987	0.826	0.087	0.019	−0.283	1.0	0.25	0.077
2n	388	367	779	0.95	11.933	0.214	0.102	0.004	0.333	1.2	0.048	0.084
2b	280	240	414	0.86	13.089	0.291	0.076	0.003	0.237	0.806	0.029	0.076
3	150.3	92	220	0.61	12.077	0.335	0.106	0.006	−0.034	1.225	0.073	0.083
6n	116.9	76.7	136	0.66	13.514	0.256	0.064	0.003	0.131	0.675	0.035	0.074
7a	379	211.1	336	0.56	14.085	0.337	0.074	0.008	−0.173	0.743	0.086	0.071
12n	231	153	244	0.66	13.245	0.246	0.062	0.003	0.361	0.634	0.028	0.076
14c	103	41.4	87	0.40	13.569	0.571	0.11	0.017	0.153	1.13	0.18	0.074
15b	93	51.54	112.2	0.55	13.908	0.213	0.122	0.008	0.119	1.196	0.072	0.072
17b	133.8	69.9	177.6	0.52	12.920	0.300	0.131	0.008	0.136	1.37	0.081	0.077

Spot name	Isotopes ratios for Wetherilll plot		Apparent ages (Ma)									
	2s (abs)	Rho	$^{206}Pb/^{238}U$	± (Ma)	$^{207}Pb/^{235}U$	± (Ma)	$^{207}Pb/^{206}Pb$	± (Ma)	Best Age (Ma)	± (Ma)	Conc. A (%)	Conc. B (%)
Data used for crystallization age (emplacement) = concordance A > 95% and concordance B > 84%												
1n	0.002	0.190	482	12	500	19	567.1	114	482	12	96	85
5	0.002	0.001	480	10	481	20	499.3	123	480	10	100	96
7b	0.002	0.094	461.8	9	467	22	491.5	132	461.8	9	99	94
10	0.002	0.335	468.3	8.8	455	15	491.5	120	468.3	8.8	103	95
12b	0.001	−0.138	468	8.5	457	22	526.0	140	468	8.5	102	89
13n	0.001	0.418	483.1	8.6	483	21	506.9	115	483.1	8.6	100	95
13b	0.002	0.021	455.3	9.9	462	21	510.8	130	455.3	9.9	99	89
15a	0.001	0.166	460.2	6.9	471	13	533.5	83	460.2	6.9	98	86
17a-SP	0.003	0.281	473	16	475	34	537.3	188	473	16	100	88
Ages data of inherited cores (source) = concordance A > 94% and concordance B > 80%												
8	0.002	0.171	869	13	911	19	994.4	67	869	13	95	87
8-SP	0.007	0.122	657	41	648	42	764.6	117	657	41	101	86

(*continued on next page*)

Table 2 (*continued*)

Spot name	Isotopes ratios for Wetherilll plot		Apparent ages (Ma)									
	2s (abs)	Rho	$^{206}Pb/^{238}U$	± (Ma)	$^{207}Pb/^{235}U$	± (Ma)	$^{207}Pb/^{206}Pb$	± (Ma)	Best Age (Ma)	± (Ma)	Conc. A (%)	Conc. B (%)
11	0.002	0.509	531	10	542	16	653.3	84	531	10	98	81
14a	0.003	0.375	907	17	941	17	1022.3	64	907	17	96	89
17a	0.004	0.292	904	22	912	28	945.9	102	904	22	99	96
Younger ages representing loss Pb (interpreted as hydrothermal alteration) = concordance A > 93% and concordance B < 85%												
6b	0.001	0.353	437.8	8.3	451	17	518.4	103	437.8	8.3	97	84
7c	0.002	0.025	438	9	465	19	614.4	118	438	9	94	71
14b	0.001	0.186	440.9	6.7	454	15	548.5	93	440.9	6.7	97	80
Discordant ages not considered in the plots = concordance A < 96% and concordance B < 69%												
1b	0.005	0.330	477	29	650	110	1360.5	421	477	29	73	35
2n	0.002	0.180	518.4	8.8	800	21	1668.1	79	518.4	8.8	65	31
2b	0.002	0.358	474	10	598	16	1103.0	79	474	10	79	43
3	0.002	0.478	513	13	809	34	1738.6	102	513	13	63	30
6n	0.001	0.263	460	8.5	514	21	744.9	109	460	8.5	89	62
7a	0.002	0.246	442	10	554	48	1036.0	230	442	10	80	43
12n	0.001	0.016	469.4	8.3	496	18	691.3	106	469.4	8.3	95	68
14c	0.003	−0.028	458	19	751	88	1799.4	281	458	19	61	25
15b	0.001	0.154	447.6	6.6	782	34	1985.7	111	447.6	6.6	57	23
17b	0.002	0.211	481	11	869	35	2114.1	106	481	11	55	23

A): Concordance calculated as (206 Pb–238U age/207 Pb–235U age)*100 - B): Concordance calculated as (206 Pb–238U age/207 Pb–206Pb age)*100.

4. Results

4.1. Geology and petrography of the LCPC

The LCPC occurs as parallel discontinuous ovoid bodies partially or entirely controlled by the general N–S structure of the metamorphic host rock (Fig. 1b). The LCPC has a wide compositions range (from ultrabasic to acidic) and three main composite bodies were distinguished. Two of them located to the north (western and eastern Puertas Coloradas) and a third in the southern sector (Las Cañas pluton s.s.). Las Cañas pluton is 800 m wide with an inverted zonation pattern with more acidic units in the borders, whereas the set of plutons near Puertas Coloradas has a random distribution, and their zonation and limits cannot be entirely defined due to the extensive quaternary cover. The three bodies and their metamorphic host rocks are cut by pegmatitic bodies that are part of the Villa Praga-Las Lagunas Pegmatitic Group (Roquet, 2010), within the Conlara Pegmatitic District (Rossi, 1966; Galliski, 1994), and they are not subject of study in this work.

The LCPC is composed of six facies: 1) Ol-Px hornblendite, 2) hornblende gabbro, 3) quartz gabbro, 4) Amp-bearing tonalite, 5) Bt-bearing tonalite, and 6) Bt-bearing granodiorite (Fig. 2). The first two facies are only present in Las Cañas pluton (s.s), and they show cumular textures and magmatic layering, from which crystal fractionation processes are inferred, while the rest of the facies show transitional limits with mingling phenomena, and processes of assimilation with the host rock, evidenced by the presence of enclaves, schlierens and xenoliths.

4.1.1. Ol-Px hornblendite facies

This facies is found in the southwestern sector of the Las Cañas pluton (s.s) (Fig. 1b). The outcropping of decametric size represents less than 5% of the pluton. They are ultramafic rocks (IC > 95), with heterocumulate texture (following the classification of Wager et al., 1960) defined by late growth of amphibole oikocrystals, wrapping olivine and clinopyroxene grains of the cumulus (Figs. 3a and 4a). The contact with the hornblende gabbros facies is defined in a few meters.

Ol-Px hornblendite is composed of olivine, clinopyroxene, amphibole, and opaque minerals (Po, Pn, Cpy, Mag) as primary phases and serpentine, talc, chlorite and opaque minerals (Mag, Spn), as secondary phases.

4.1.2. Hornblende gabbro facies

These rocks (< 5% of LCPC) are present either as a thin layer surrounding the Ol-Px hornblendite facies, in transitional contact with the quartz gabbro or Amp-bearing tonalite facies, or as enclaves within them (Fig. 1b). It is composed of amphibole, plagioclase, quartz, titanite and opaque minerals as primary phases and epidote-group minerals, biotite, and chlorite as secondary minerals (Table A1). It has a melanocratic color index (CI: ~75), a cumulate texture ranging from medium to fine grain, and rhythmic magmatic layering given by intercalation of Amp-rich dark layers and Pl-rich light layers (Figs. 2, 3b and 4b).

4.1.3. Quartz gabbro facies

It corresponds to ~15% of the LCPC and is observed in several zones of the Puertas Colorada plutons and within the Las Cañas Plutón (Fig. 1b). They are mesocratic rocks (CI: ~50), which have a medium to fine equigranular texture (Fig. 3c). Locally, an isolated small elongated body occurs a few meters east of the Las Cañas pluton and is separated through a septum of metamorphic rocks. In this sector, grain size is bigger with minor plagioclase and biotite.

In general, quartz gabbro facies is composed of plagioclase, amphibole, quartz, biotite, titanite, apatite and opaque minerals (Mag, Py, Cpy), as primary phases, and chlorite, sericite, biotite, epidote-group and opaque minerals as secondary phases (Table A1).

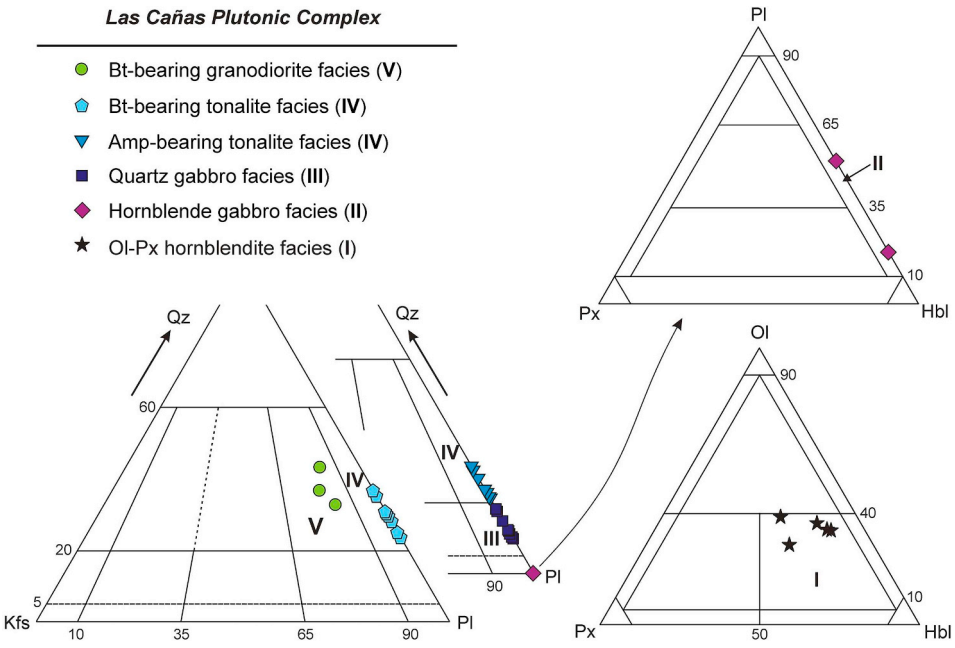

Fig. 2. Modal compositions of LCPC. I = olivine-pyroxene hornblendites. II = hornblende gabbros. III = quartz gabbros. IV = tonalities. V = granodiorites.

4.1.4. Amphibole-bearing tonalite facies

This group covers more extensive areas than the quartz gabbro facies (~30% of the LCPC) and is present in all the plutons (Fig. 1b). It is always spatially linked to the quartz gabbro facies and corresponds to a transition zone between the latter and the biotite-bearing tonalite facies. In some sites, this facies has an injection of pegmatitic dikes and quartz-tourmaline-bearing veins that generate a penetrative hydrothermal alteration in relation to a late or subsequent magmatic episode (Fig. 3d). The contact with the schists of the host rock shows a moderate to high couplement and assimilation degree, due to xenoliths incorporation of various sizes (~0.1–1 m), and development of an intercalation zone that generally is affected by ductile shearing.

The Amp-bearing tonalite facies is a mesocratic rock (CI: ~50) with equigranular to hypidiomorphic unequigranular textures. Locally in some samples, a plagioclase and quartz-rich matrix surrounds larger crystals of amphibole and plagioclase showing a porphyritic texture. The concentrations of amphibole in this facies vary widely, from very low contents (3%) to high modal contents (80%) (Table A1).

The primary minerals are plagioclase, amphibole, quartz, biotite, titanite, apatite, zircon, allanite and opaque minerals (Ttn, Ilm, Mag, Py), and the secondary ones are chlorite, muscovite (sericite), biotite and epidote-group minerals.

4.1.5. Biotite-bearing tonalite facies

It is the most abundant facies (~40%) throughout the LCPC. The limit with the metamorphic host rock occurs in a few meter zone given by the intercalation of both lithologies. Remarkably, along this zone, the contact surface disposes parallel to the internal foliation of the banded schists, where the grain size of the tonalite decreases slightly. Likewise, it is common the incorporation of schistose xenoliths with diffuse edges (schlierens), although there are also xenoliths with straight and angular borders. Small bodies of ~50 m wide, with high long-wide (> 6:1) ratios are located between the Las Cañas pluton and the western pluton of Puertas Coloradas (Fig. 1b). In these cases, they alternate with schists (host rock) and present a magmatic fabric parallel to the penetrative regional (S_2) foliation of the metamorphic basement. Amp-rich schilierens (which modally correspond to Amp-bearing tonalites) are also found within the biotite-bearing tonalite facies, indicating mingling processes between both lithologies (Fig. 3e).

Bt-bearing tonalite is a mesocratic rock (IC: ~45) with a texture ranging from equigranular to hypidiomorphic inequigranular of medium-size. It is composed of plagioclase, quartz, biotite, apatite, titanite, zircon and opaque minerals as primary phases, and sericite, chlorite, and epidote-group minerals as secondary minerals (Table A1).

4.1.6. Biotite-bearing granodiorite facies

Related to the other facies (except pegmatitic bodies) the Bt-bearing granodiorite facies is the most differentiated from the LCPC. It is located through small bodies between Puertas Coloradas and Las Cañas plutons, as well as in the western sector of these. In general, they exhibit a relationship of contemporaneity with the biotite-bearing tonalite facies (gradational or lobed contacts), being, in most cases, difficult to discern between these facies with the naked eye. Also, the bodies show a very marked space link with pegmatites that emerge from the migmatitic unit located immediately to the west (Fig. 3f) and host numerous xenoliths of host rocks.

The group is formed by leucocratic rocks (IC: ~15), of hypidiomorphic medium grain size texture, composed of plagioclase, quartz, alkali feldspar, biotite, muscovite, opaque minerals, titanite, apatite, and zircon as primary minerals, while sericite and epidote-group minerals as secondary phases are common.

4.2. Mineralogy of the LCPC

4.2.1. Olivine

The mineralogy corresponds to forsterite 82% ($Fo_{81.7}$ - Fa_{18} - $Tep_{0.3}$) that is only present in Ol-Px hornblendite facies. It is observed in subhedral crystals with an average size of 1.5 mm, partial to completely replaced by serpentine (pseudomorphic replacement), and wrapped by oikocrystals of amphibole (Fig. 4a). In some cases, a post-magmatic crown with exsolution of magnetite is observed. It is characterized by having an elevated mg-number [(100*Mg/Mg + Fe) atoms = 82 ± 0.4)] which indicates that the source was an Mg-rich primitive magma.

4.2.2. Pyroxene

Pyroxene (Cpx) corresponds to diopside (Wo_{48} - En_{46} - Fs_6). It occurs in subhedral crystals up to 1 mm in size. The crystals are strongly altered by talc and to a lesser extent by serpentine and opaque minerals. Many crystals are partially resorbed at their edges showing irregular faces, and amphiboles as tiny patches indicate an incipient

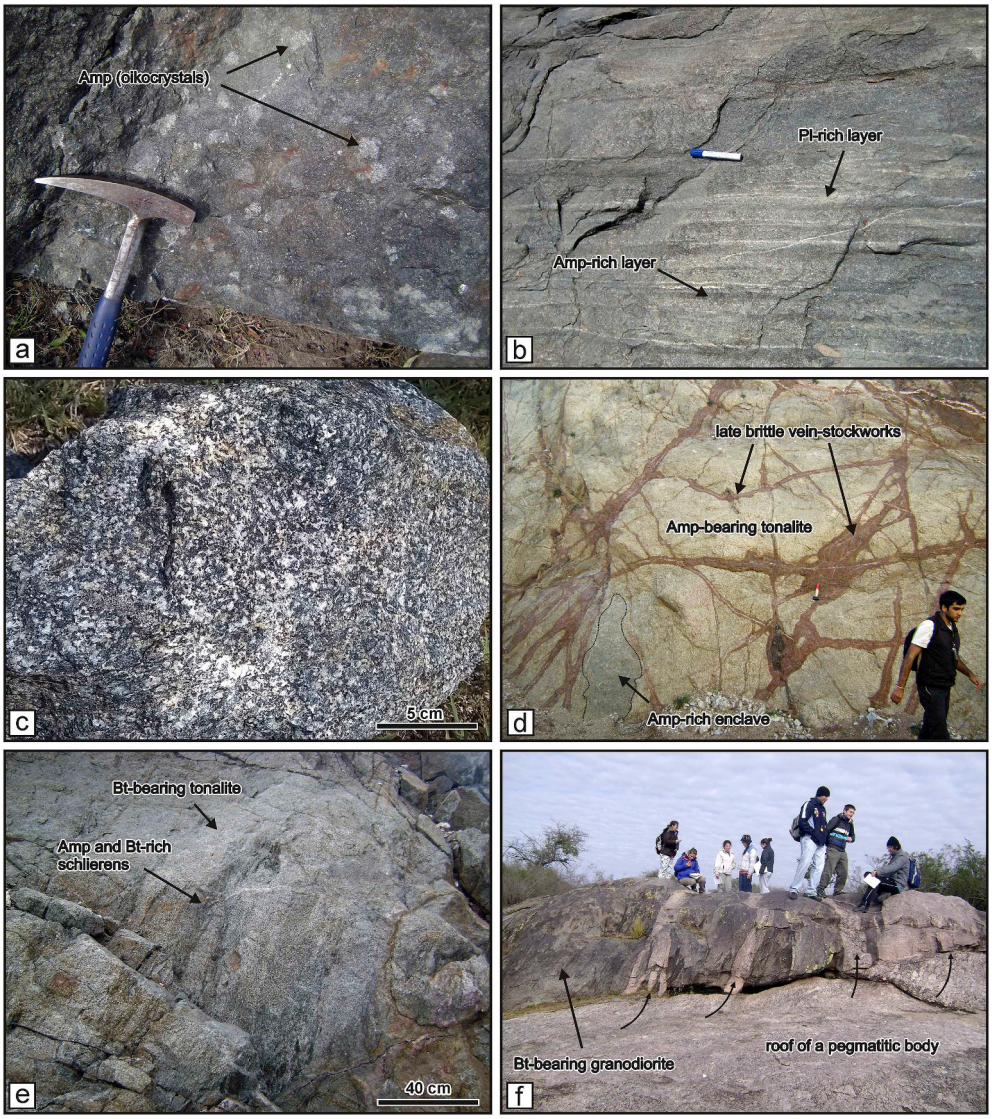

Fig. 3. Photographs of different facies of the LCPC. a) Ol-Px hornblendite facies. b) Hornblende gabbro facies. c) Quartz gabbros facies. d) Amp-bearing tonalite facies. e) Bt-bearing tonalite facies. f) Bt-bearing granodiorite facies intruded by late pegmatitic dikes.

replacement. Together with olivine, they are enveloped by oikocrystals of amphibole (Fig. 4a) and are only present in Ol-Px hornblendite facies.

4.2.3. Amphibole

Amphibole from Ol-Px horblendite facies occurs in large poikilitic subhedral to euhedral crystals (~25 mm) randomly oriented. Its composition varies from pargasite to magnesio-hornblende (mg# = 80) but are partially resorbed in patches by magnesio-ferri-hornblende (mg# = 69) (Figs. 4a and 5a). In some samples, amphibole is strongly replaced by chlorite together with opaque minerals exolution in a postmagmatic stage.

In hornblende gabbro facies, amphibole is magnesio-hornblende (Fig. 5a) with mg# = 64. It is presented in aggregates of subhedral crystals of ~1 mm size, showing simple twinning, and in some cases is replaced by chlorite and biotite at its edges (Fig. 4b).

In quartz gabbro facies the amphibole varies between magnesio-hornblende and magnesio-ferri-hornblende, although cummingtonite is also found (in sample LC-35). It is presented in subhedral prismatic crystals of ~1.2 mm size and shows simple twinning and sometimes zoning (Fig. 4c). Also, it is replaced by chlorite in some cases. The calcic amphibole crystals that have SiO_2 > 45 wt % in quartz gabbro facies, also have higher mg# (~70), while SiO_2 < 45 wt %, the mg# is ~57. On the other hand, cummingtonite presents mg# = 62, being the amphibole with the highest SiO_2 in the complex.

In Amp-bearing tonalite facies, the amphibole occurs in prismatic euhedral to subhedral crystals with ~1.5 mm size (Fig. 4d), exhibiting simple twinning, and is partially replaced by chlorite. In some sites where the percentage of amphiboles is scarce, these are strongly reabsorbed and altered to chlorite. They belong to calcic amphiboles and correspond to ferri-tschermakite, magnesio-ferri-hornblende and magnesio-hornblende (Fig. 5a), following the IMA consideration (Hawthorne et al., 2012). It shows an increase in mg# as the concentration of SiO_2 increases, with values of mg# ranging from 57 to 77 over a range of SiO_2 from 43 to 51 wt%.

4.2.4. Plagioclase

In hornblende gabbro facies, plagioclase appears as subhedral crystals of ~2 mm size and shows compositional zonation. The cores correspond to bytownite-anorthite (An_{89-91}) that have been partially reabsorbed by the mantle (Figs. 4b and 5b). In most crystals, the cores are strongly dissolved by labradorite (An_{49-61}). The mantles present a median composition of An_{52} (labradorite) where its external borders are sutured, possibly indicating the last stage of crystallization (Fig. 6a). On

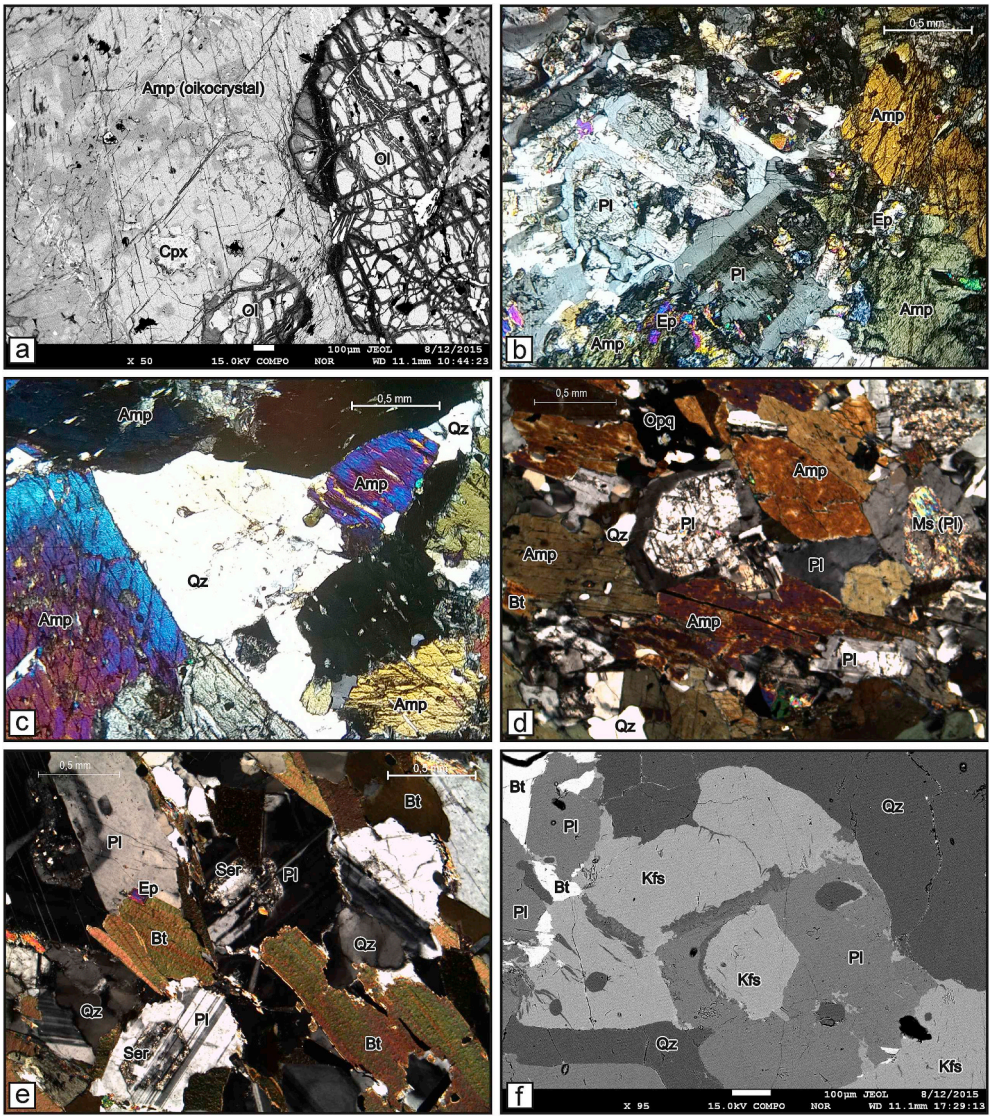

Fig. 4. a) BSE image of Ol-Px hornblendite facies. Compositional zonation observed in an amphibole oikocrystal. b) Crossed nicols microphotograph of the hornblende gabbro facies. c) Crossed nicols microphotographs of quartz gabbro facies. d) Crossed nicols microphotograph of the Amp-bearing tonalite facies. e) Crossed nicols microphotographs of the Bt-bearing tonalite facies. f) BSE image of the Bt-bearing granodiorite facies.

the other hand, plagioclase is very altered by epidote-group minerals in the subsolidus stage, mainly in their cores.

In quartz gabbro facies, plagioclase occurs as euhedral to subhedral crystals with 1.5 mm average sizes. It presents a compositional zonation with cores, mantles, and rims (Fig. 5b). The cores correspond to bytownite (An_{72-87}) and are dissolved by labradorite ($Añ_{60}$) with texture in box or cells (spongy-cellular type) (Fig. 6b and c). The mantles are composed of andesine-labradorite (An_{34-65}). Their rims are very thin (~10 μm), corresponding to oligoclase (An_{17-26}) that are not found in all crystals. The cores show alteration to muscovite (sericite) and epidote-group minerals, while the mantles remain unchanged.

In Amp-bearing tonalite facies plagioclase is zoned, with cores of labradorite-bytownite (An_{67-72}), which presents spongy-cellular texture (Figs. 5b and 6d). In general, the cores are replaced by epidote-group minerals and sericite (Fig. 4d). The mantles are formed by andesine-labradorite (An_{45-58}) presenting sutured edges. The rims are very thin (< 0.1 mm), not found in all crystals and their composition is oligoclase (An_{18}) (Fig. 6e).

Within Bt-bearing tonalite facies, plagioclase occurs in euhedral to subhedral crystals (Fig. 4e) and has two types of composition and zoning. Some crystals present core-mantle-rim structures with a progressive decrease of An content, cores of bytownite (An_{74-82}), mantles of labradorite (An_{54-59}) and rims of andesine (An_{43-48}) (Fig. 6f). Other crystals have cores of labradorite (An_{53-57}), thinner mantles with bytownite composition (An_{70-75}), and rims compositionally very similar to the cores (An_{52-53}) (Fig. 6g).

Plagioclase occurs in euhedral to subhedral crystals within Bt-bearing granodiorite facies. There are two types according to their composition and zoning. Some crystals have cores of An_{70} strongly dissolved (spongy-cellular), then, a plagioclase of andesine composition (An_{40-45}) grows like a mantle that wraps up to the dissolved calcic cores. The rims of these crystals are from An_{37} (Fig. 6h). The cores are usually very altered by epidote-group minerals and sericite. Another type of crystals has a very slight gradual compositional variation (uniform zoning) from a center of composition An_{42} to an edge of An_{30} (andesine). Generally, these crystals are replaced by muscovite tablets (Fig. 6i).

4.2.5. K-feldspar

Alkali feldspar only occurs in Bt-bearing granodiorite facies. It appears as irregular grains with scattered lobed edges and interspersed with plagioclase and quartz (Fig. 4f). Its composition is very

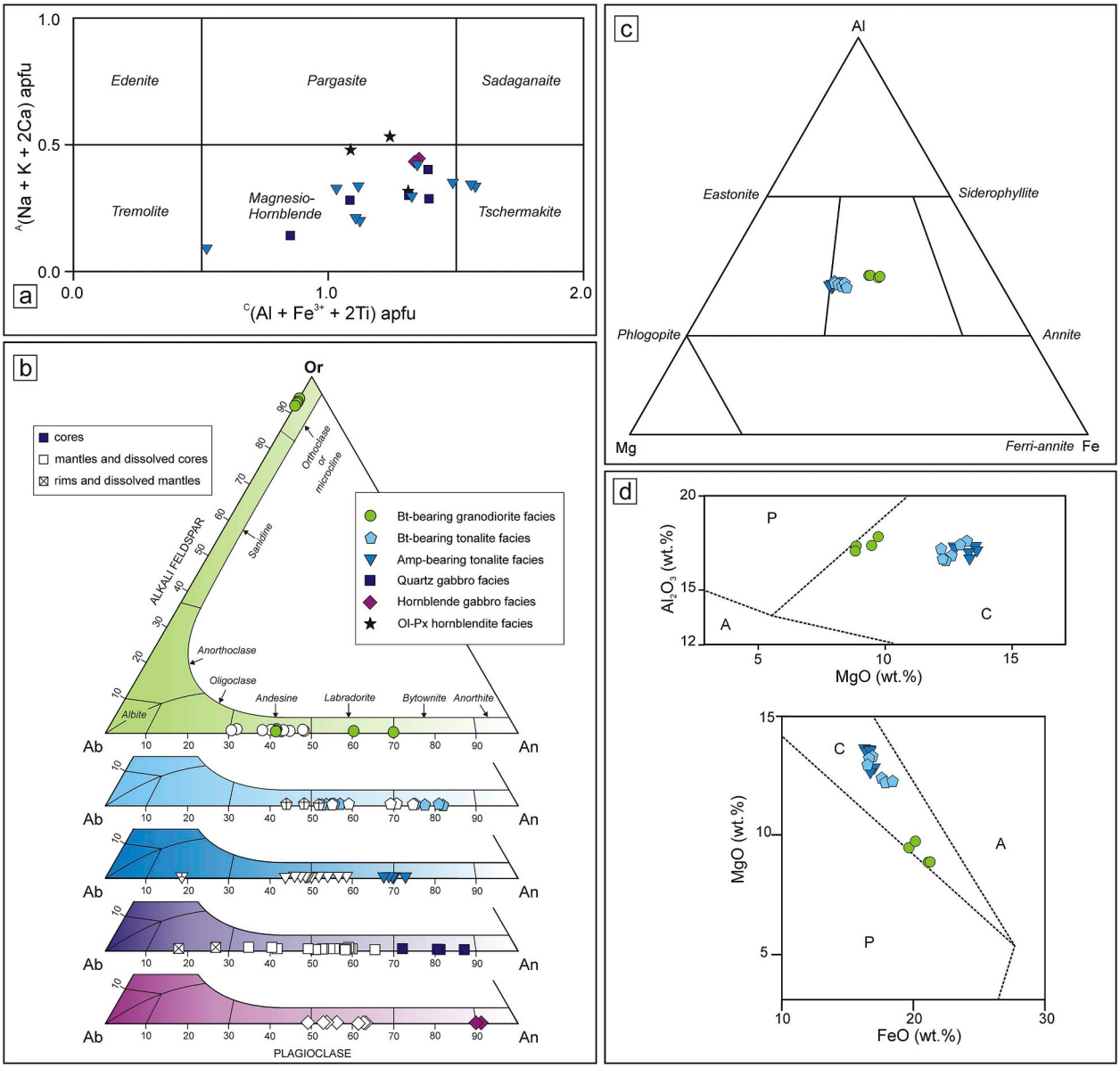

Fig. 5. a) Calcic amphibole classification diagram following new IMA recommendations (Hawthorne et al., 2012). Amphiboles were classified using the AMPH 2012 2.0 software (Oberti et al., 2012). b) Feldspars compositions for the different facies of the LCPC. c) Composition of the micas from the LCPC in the Al-FeT-Mg (a.p.f.u) triangular diagram after Barbosa et al. (2012). d) MgO, FeO * and Al_2O_3 diagrams after Abdel-Rahman (1994). A = biotites of alkaline granites (type A). C = "biotites" of calc-alkaline granites, mainly related to subduction orogens (I-type). P = "biotites" of peraluminous rocks, including collisional granites (S-type).

homogeneous and corresponds to orthoclase/microcline ($Ab_{5.9\text{-}7.8}$ - $An_{0\text{-}0.1}$ $Or_{90.5\text{-}93.4}$) (Fig. 5b). Based on its anhedral (interstitial) texture, filling along with quartz, spaces between grains of plagioclase, it is considered late in the crystallization sequence.

4.2.6. Biotite

Dark mica "biotite" is very sparse in hornblende gabbro facies, forming patches of ~0.1 mm replacing to amphibole.

Inside the quartz gabbro and Amp-bearing tonalite facies, biotite is not always present (Table A1), but when it is present, appears as laminar crystals with an average of 0.5 mm in size. In some sectors, it is partially replaced by chlorite in late magmatic or hydrothermal state. It has an average Fe/(Fe + Mg) ratio of 0.41 which corresponds to biotite (s.s.), although very close to the limit of the phlogopite field (Fig. 5c).

In Bt-bearing tonalite facies, dark mica is very common as laminar crystals or oriented crystalline aggregates drawing the magmatic foliation (Fig. 4e). By sectors, it is replaced by chlorite and epidote-group minerals. As in the previous facies, it corresponds to biotite (s.s.) close to the phlogopite limit, although its average Fe/(Fe + Mg) ratio is a bit higher (0.43) than in Amp-bearing tonalite facies (0.41).

Dark mica from Bt-bearing granodiorite facies forms laminar subhedral crystals. Their composition moves away from the boundary of the phlogopite field and shows a higher proportion of the annite molecule [Fe/(Fe + Mg) = 0.55] related to other dark micas.

In general, dark mica from LCPC is typical of calc-alkaline granites, based on their MgO, FeO* and Al_2O_3 wt.% contents (Abdel-Rahman, 1994) (Table A2), although clearly those corresponding to Bt-bearing granodiorite facies deviate from the tonalite group, approaching the biotite field of peraluminous granites (Fig. 5c).

4.2.7. Quartz

The modal proportions of this mineral vary widely between facies (Table A1). In general, quartz occurs as anhedral interstitial grains of 0.2–0.5 mm in size, late in the crystallization sequence of this rock

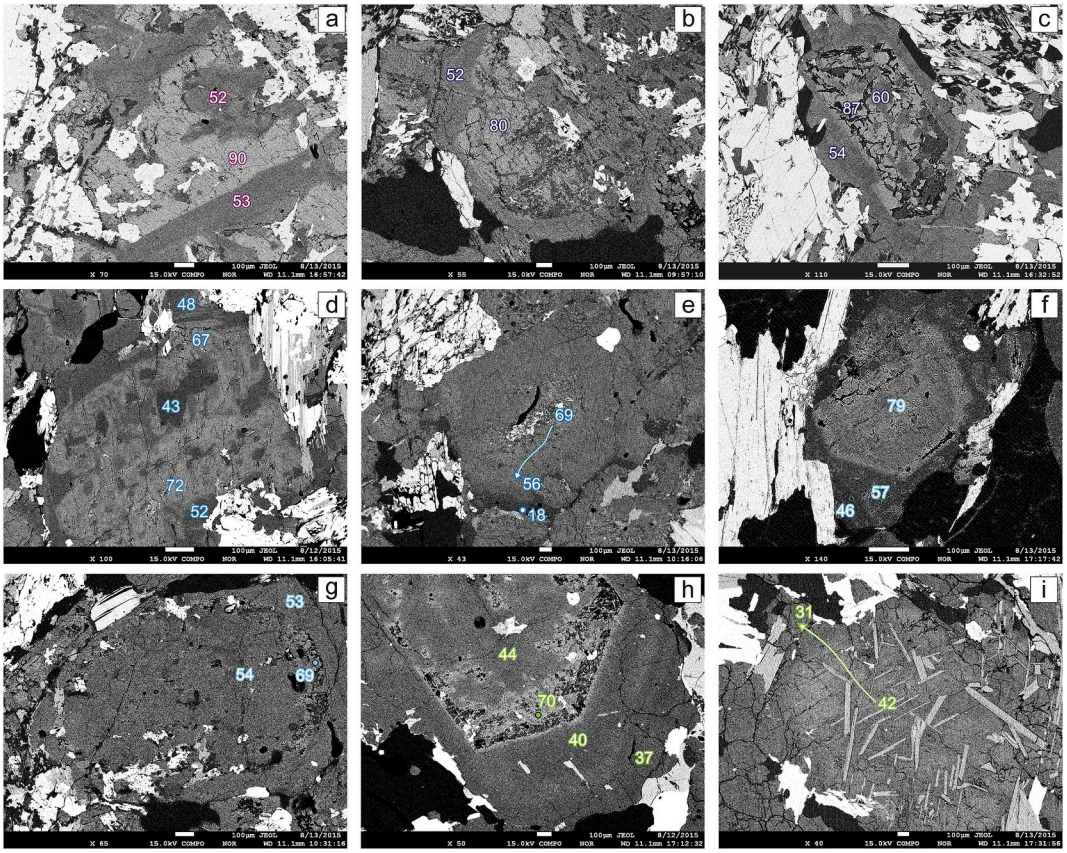

Fig. 6. Back-scattered-electron (BSE) images (Z contrast) of plagioclase from: a) Amp-bearing gabbros facies. b-c) Quartz gabbro facies. d-e) Amp-bearing tonalite facies. f-g) Bt-bearing tonalite facies. h-i) Bt-bearing granodiorite facies. The numbers represent An%.

(Fig. 4c, d, e, f). Locally it has irregular and sutured edges, usually exhibiting undulating extinction.

4.2.8. Other minority phases

Apatite, titanite, allanite, and zircon are observed in small euhedral prisms (< 0.5 mm).

Apatite is common in Bt-bearing tonalite and granodiorite facies, and less common in mafic facies. Titanite sometime appears surrounded by opaque minerals, especially in gabbro facies.

Primary allanite is present as traces in Amp-bearing tonalites facies, and almost always presents crowns of other epidote-group minerals. Zircon crystals are common as inclusions in amphibole and biotite, distinguished by the development of pleochroic halos.

4.2.9. Sulfides and oxides

The opaque minerals present in the LCPC form small grains (2–4 mm) dispersed among the silicated matrix of the rocks. In cumulates (Ol-Px hornblendite and hornblende gabbro facies), they are mainly composed of magnetite ± pyrrhotite ± pentlandite ± chalcopyrite. These minerals are linked together and show exsolution textures.

In quartz gabbro facies, pyrite and chalcopyrite are the present sulfides, while in Amp-bearing tonalite, pyrite is the only sulfide observed. Magnetite is the oxide that is always accompanying the set of sulfides in the basic rocks. Ferrum-hydroxides (Gth) are usually found as secondary minerals. Also, magnetite is common as a replacement product of olivine along with serpentine within of cumulates, while small inclusions (< 10 μm) of Al–Cr spinel are recognized in clinopyroxene crystals.

In quartz gabbros and tonalite facies, titanite-ilmenite-magnetite association is common in dispersed small grains up to 0.4 mm in size, whose magnetite-ilmenite compounds are interpreted as an oxy-exsolution product during subsolid conditions.

4.3. Crystallization conditions

Crystallization temperatures and pressures in some facies were obtained through mineral compositions, with the assumption that they were not modified after their crystallization, and only considering samples in which the textural relationships between minerals and their chemical compositions indicate that the system was in equilibrium.

For the calculations, four geothermometers were used: 1) Amp-thermometer (Putirka, 2016); 2) Amp-TB geothermobarometry (Ridolfi et al., 2010); both were implemented in Ol-Px hornblendite, gabbros and Amp-bearing tonalite facies (in tonalites, the pressure was also determined); 3) Hbl-Pl (Holland and Blundy, 1994) for gabbros and Amp-bearing tonalite facies; and 4) two-feldspar (Whitney and Stormer, 1977) for Bt-bearing granodiorite facies.

The results indicate that the crystallization temperatures in the different samples of the LCPC decrease with the differentiation grade of the rocks (Table 1), being higher in the Ol-Px hornblendite facies (974 °C) and minimum in the Bt-bearing granodiorites (690 °C).

Calculation was made through both Amp-thermometers indicating a decrease in temperature with the increase in the degree of differentiation, in the same way as the calculations made with the Hbl-Pl thermometer; although unlike the latter, the first two show significantly higher values in a quartz gabbro and two Amp-bearing tonalite samples, in comparison to the values calculated in the same samples by the Hbl-Pl thermometer (Table 1). These differences could be juxtified since the calculations in the Hbl-Pl thermometer in rocks with amphibole were taken only with albite concentrations in plagioclase cores [x (Ab)Pl], with the assumption that they were in equilibrium with the magma at

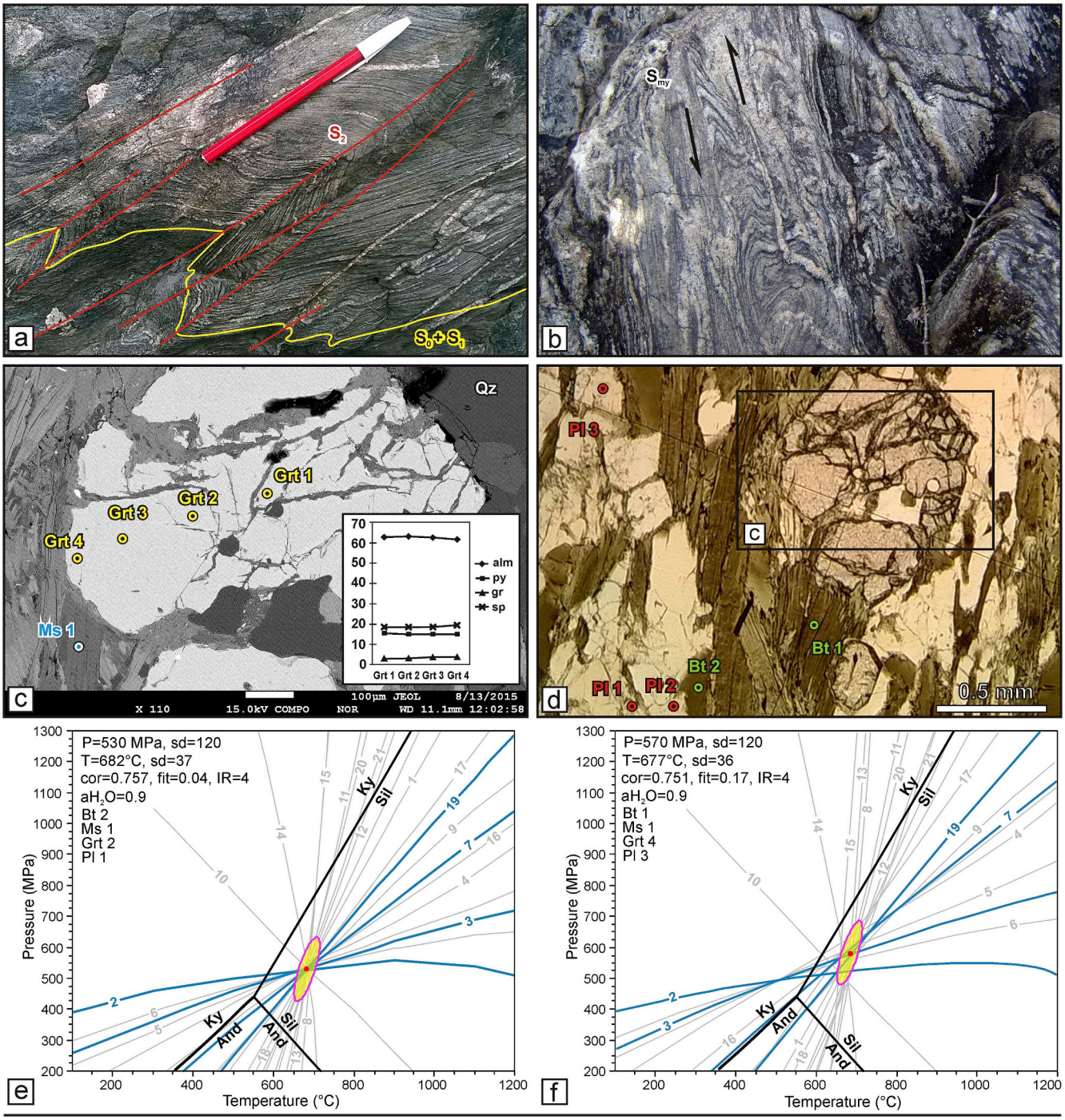

Fig. 7. Photographs of metasedimentary host rock of LCPC. a) Asymmetrical isopach folds in banded schists (quartz-biotite schist unit). b) Stromatitic metatexites with high-temperature ductile shear. c) BSE image showing a garnet porphyroblast with the analyzed points and a muscovite crystal that is in contact. There is also a compositional profile of the Grt (from core to edge), showing little chemical variations. d) Photomicrograph showing the metamorphic fabric, the location of the porphyroblast represented in (c), and the location of other analysis (Bt and Pl). e-f) P-T diagrams showing the set of independent reactions and metamorphic conditions for schist (with its standard deviation represented by the ellipse), calculated by 4 independent reactions (blue lines), for two analysis combinations: Bt 2 Ms 1 Grt 2 Pl 1 [internal sector of garnet (e)] and Bt 1 Ms 1 Grt 4 Pl 3 [external sector of garnet (f)]. (For interpretation of the references to color in this figure legend, the reader is referred to the Web version of this article.)

the same time that amphibole was crystallized, unlike mantles and rims, which probably represent a late-stage of crystallization, or magma mixing processes at some point in the history of cooling of the bodies, evidencing an imbalance in the system.

The pressure was only calculated for Amp-bearing tonalites for ferritschermakite composition since the rest of the amphiboles present Al# > 0.21 which invalidates the calculations according to the geobarometer of Ridolfi et al. (2010). The calculated pressures for the Amp-bearing tonalite facies gave pression of 457 ± 114 and 432 ± 108 MPa (Table 1), equivalent to an average depth of 17.1 ± 4.3 km (considering a pressure gradient of 0.26 MPa/km).

4.4. Features of metasedimentary host rock

Two units compose the host rock of LCPC: 1) quartz-biotite schists, located in the eastern sector and 2) migmatites located in the western part (Fig. 1b). These two units are strongly tectonized and associated with the development of a wide ductile shear zone named El Salado-La Cocha Shear Zone, which is developed in several arms along the transition between them.

Schists have a millimeter-scale compositional banded (Fig. 7a) and simple mineralogy consisting of Qz + Pl (light bands) and Bt ± Ms (dark bands), although some varieties also contain Kfs ± Sil ± Tur ± Grt as accessory phases.

The migmatites are located in the western sector, and their contact with the schists is transitional which develops in a few meters through a zone characterized by the presence of metatexitic migmatites in the eastern edge (highly deformed), and an increase in the leucosome part towards the west that culminates with a predominance of diatexitic migmatites (Fig. 1b).

In metatexites, the principal structure is a stromatitic foliation locally folded (Fig. 7b); while in diatexites the schollen, schlieren, and veins are common structures with evidence of important mobility and percolation of a molten fraction.

Metatexites are heterogeneous at the outcrop scale with coherent, pre-partial melting structures preserved in the paleosome. In these rocks, the neosome is segregated into leucosome and melanosome. The leucosome has tonalitic-granodiorite composition (Qz + Pl + Bt ± Kfs ± Sil), with grain sizes varying in millimeter order, whereas the melanosome is composed mainly of Bt ± Sil. The paleosome is made up of banded schists. Diatexites have more than 85% melt, with less than 15% of the paleosome remaining in the form of discontinuous and isolated blocks (schollen), and diffuse schlierens parallel to the flow fabric. They are modally of Bt-bearing granodioritic composition.

Three deformational events generated the internal structure of the metasedimentary host rock. The first (D_1) deformational event is characterized by the development of a schistosity (S_1) surface, which determines planes with variable strike sub-parallel to a relict (S_0) sedimentary surface (Fig. 7a). The second (D_2) deformational event is considered the most important within the group. This event folds to $S_1 + S_0$ surfaces and is characterized by the development of a penetrative axial plane (S_2) surface with NNE trending (average 10°), and variable dips (between 30° and 80°), always towards the SE (with rare exceptions to the NW). The (F_2) folds are overturned and asymmetrical; their interlimb angles vary from closed to open and in sectors they are harmonic whereas in other are disharmonic. The (B_2) axes plunge toward NNE or SSO between 14° and 60°. The third (D_3) deformational event is associated with ductile shear surfaces (S_{my}) that form parallel to subparallel to the S_2 surfaces. These planes are present in different scales, from decimeters (Fig. 7b) to major shear zones that acquire regional importance towards the transition between migmatites and schists (El Salado-La Cocha). The shear zones present strikes of ~11° on average, and dips between 60° and 80° SE. Mineral stretching lineations (L_{my}) with plunge direction of ~63° are common and are characterized by normal kinematics with a sinistral strike-slip component. The (F_3) asymmetrical folds associated with the shear zone and σ-type indicators evidence the movement sense in the field.

A low-temperature (D_4) local deformation (brittle shear) can be recognized along the central part of the area that is superimposed on the high-temperature ductile deformation. The planes are subparallel to a previous ductile shear and dip to the east, but the stretch mark directions (45° SE) together with other indicators (e.g. Riedel fractures and tension gashes) attest an oblique inverse movement with a minor sinistral strike-slip component, where the hanging wall is the eastern block.

4.4.1. P-T conditions of the LCPC host rocks

A microchemical analysis was obtained on biotite, muscovite, garnet and plagioclase in a sample belonging to the schists unit (Fig. 7c and d), located ~200 m west of the Las Cañas pluton (Fig. 1b).

The paragenesis determined in this sample is Qz + Bt + Pl + Grt + Ms + Tur + Fi. This association corresponds to amphibolite facies and represents a climax stage, while a retrograde event is evidenced by replaces of Grt and Bt by Ser + Chl, following the reaction Grt + Bt = Ms + Chl in greenschist or low amphibolites facies. The data obtained in the microanalysis and the subsequent calculations of structural mineral formulas are presented in Table A4. The average P-T conditions for the metamorphic climax in schists is ~550 ± 120 MPa and 680 ± 37 °C, representing a temperature gradient ($\Delta T_{(h)} = T.\rho_c.g/P$) of ~32.3 °C/km that corresponds to a low-pressure series in middle-amphibolite facies. However, the best result (fit of 0.04) was obtained with the Grt core analysis, yielding values of 530 ± 120 MPa and 682 ± 37 °C, while values of 570 ± 120 MPa and 677 ± 36 °C were calculated with the Grt rim analysis (Table A.5 and Fig. 7e and f).

4.5. Whole-rock geochemistry of the LCPC

4.5.1. Major elements

The LCPC rock samples vary over a wide range of SiO_2, displaying an almost continuous trend from cumular Ol-Px hornblendite facies with around 43 wt% to Bt-bearing granodiorite facies with 65 wt% (Table 3). Hornblende gabbro facies mostly have SiO_2 contents below 50 wt %, whereas quartz gabbro 47–53 wt % of SiO_2.

The rocks of LCPC correspond to a subalkaline suite with magnesian composition, where Mg-number [Mg# = 100*MgO/(MgO + FeO) on a molar basis] ranges from 83 in Ol-Px hornblendites to 40 in Bt-bearing granodiorites. They are calc-alkaline to calcic and metaluminous, consistent with the ferro-magnesian minerals (Amp + Bt) which reflect the Al_2O_3 deficit (Table 3 and Fig. 8).

In terms of major elements, there is considerable overlap in FeOt, CaO, Na_2O, and K_2O, among hornblende gabbro and quartz gabbro facies, while there is a contrast in values of Ti_2O, Al_2O_3 and Mg-number (Fig. 9).

The chemical variation from gabbros to granodiorites shows a broad but well-defined trend of decreasing FeOt, MgO and CaO with increasing SiO_2 (Fig. 9).

The low contents of Al_2O_3 and CaO, such as the high MgO in the Ol-Px hornblendite facies and some samples of hornblende gabbros, reflect the absence of plagioclase in the cumulates of the Las Cañas pluton.

In the quartz gabbros facies there are two groups of samples. One group has higher concentrations of SiO_2, Fe_2O_3, MgO and Mg# (high silica quartz gabbro), while the other group has low SiO_2 but higher CaO, Al_2O_3, Na_2O (low silica quartz gabbro) (Table 3).

The tonalitic rocks present a range that goes from 52 wt % of SiO_2, in Amp-bearing tonalite, to 60 wt % in Bt-bearing tonalite facies. The concentration of SiO_2 in Bt-bearing granodiorite samples (64–66 wt %) deviates from the most differentiated tonalites (Table 3 and Fig. 9).

The Bt-bearing granodiorite facies have lower CaO and FeOt and higher Na_2O and K_2O than the Bt-bearing tonalite facies, and they are of high-K, unlike the rest of the facies, which are projected in the low to medium-K fields (Fig. 9).

In the Mg# versus SiO_2 diagram, plutonic rocks show a trend that crosses the limit between tholeiitic and calc-alkaline field at about 58 wt % of SiO_2 (Fig. 9). The Mg-number shows a remarkable difference between the more basic rocks (Ol-Px hornblendite and hornblende gabbros facies) with Mg# = 61–82, and the rest of the facies, in which there is an overlap in the range of Mg# values (40–59) for a wide range of SiO_2 concentrations (Fig. 9). An important consideration is that if the compositional average of continental and oceanic arc basalts published by Kelemen et al. (2003) is plotted, the samples that most resembles, and therefore could be considered as compositional equivalent to the parental magma of the studied rocks, belong to the quartz gabbros or hornblende gabbro facies.

Table 3
Whole-rock chemical analyses of Las Cañas plutonic complex.

Facies	Ol-Px hornblendite	Hornblende gabbro			Quartz gabbro				
Sample	E1	E5-e	E4	20608-e	LC-35	BLC-1A	LC-9	E2-e	W1
Major elements (wt.%)									
SiO_2	43.06	49.56	46.94	46.63	52.37	49.25	51.08	47.5	47.75
Al_2O_3	5.7	7.79	19.13	12.16	13.39	15.05	13.24	20.53	19.32
Fe_2O_3t	11.4	10.89	8.84	11.13	13.07	12.76	12.53	10.19	12.43
MnO	0.158	0.187	0.134	0.204	0.21	0.16	0.21	0.14	0.131
MgO	25.02	17.43	8.37	12.2	8.25	7.29	8.76	3.78	5.15
CaO	7.96	8.7	9.73	10.9	6.12	9.58	7.93	9.09	9.77
Na_2O	0.51	1.26	1.78	1.29	1.51	1.96	1.52	2.45	2.25
K_2O	0.14	0.06	0.95	0.42	0.69	0.59	0.87	1.11	0.62
TiO_2	0.299	0.601	0.913	0.7	1.29	1.52	1.38	1.161	1.667
P_2O_5	0.03	0.1	0.05	0.15	0.38	0.15	0.35	0.71	0.09
LOI	6.55	3.34	2.97	3.58	3.63	1.83	2.57	2.8	1.65
Total	100.8	99.9	99.83	99.37	100.91	100.13	100.45	99.45	100.8
Mg#	83.16	78.27	68.06	71.15	58.69	56.25	61.14	45.49	48.25
Trace elements (ppm)									
Sc	37	28	38	58	22.84	32.47	31.57	17	38
Be	< 1	1	1	< 1	1.64	1.75	1.33	1	2
V	170	178	291	296	296	383	325	140	374
Cr	2100	1080	170	720	183	108	261	20	< 20
Co	87	62	36	44	115	59	74	20	36
Ni	640	590	100	170	94	71	114	< 20	< 20
Cu	80	< 10	60	30	56.06	73.57	57.44	20	70
Zn	60	110	60	120	157.40	143.40	164.99	220	100
Ga	6	10	15	13	9.28	12.38	11.39	22	22
Ge	1	3	1	2	–	–	0.42	1	2
As	< 5	< 5	< 5	< 5	–	–	–	< 5	< 5
Rb	3	< 2	37	11	30	19	34	49	18
Sr	47	35	203	79	140	211	138	348	308
Y	6	10	15	17	19	32	36	29	39
Zr	20	57	40	67	125	79	186	672	60
Nb	< 1	2	2	3	7	7	8	6	6
Mo	< 2	< 2	< 2	< 2	0.27	1.40	0.60	< 2	< 2
Ag	< 0.5	< 0.5	< 0.5	< 0.5	0.85	4.29	1.36	5.6	< 0.5
In	< 0.2	< 0.2	< 0.2	< 0.2	0.33	0.64	0.58	< 0.2	< 0.2
Sn	2	1	2	< 1	1.16	8.42	2.69	16	3
Sb	< 0.5	< 0.5	< 0.5	< 0.5	0.62	0.94	1.03	< 0.5	< 0.5
Cs	< 0.5	1.7	5.9	2.5	7.19	9.24	10.18	9.5	8.4
Ba	37	12	135	66	115	299	198	258	108
La	2.1	5.3	10.2	12.3	53.11	21.96	32.90	24.8	16.1
Ce	4.9	14.8	25.1	27.1	112.23	62.05	82.55	55.7	41.6
Pr	0.65	2.2	3.19	3.35	11.40	7.79	10.76	7.13	6.25
Nd	3.3	10.8	13.6	14	45.02	34.71	51.42	32.8	31.1
Sm	0.9	2.6	3	3.1	5.55	6.27	9.17	6.7	8.4
Eu	0.25	0.93	0.85	0.85	1.67	1.93	2.57	1.76	1.73
Gd	1	2.3	3	3.2	6.42	7.83	12.19	6.4	8
Tb	0.2	0.4	0.5	0.5	0.79	1.17	1.70	1	1.3
Dy	1.1	2.1	2.6	3.1	4.30	6.77	10.37	5.3	7.1
Ho	0.2	0.4	0.5	0.6	0.85	1.37	2.00	1	1.4
Er	0.6	1.1	1.5	1.8	2.58	3.96	5.61	3.1	3.9
Tm	0.09	0.16	0.22	0.27	0.34	0.58	0.78	0.45	0.55
Yb	0.6	1	1.3	1.7	2.17	3.32	4.42	3	3.4
Lu	0.1	0.17	0.21	0.28	0.38	0.60	0.74	0.53	0.49

(*continued on next page*)

Table 3 (*continued*)

Facies	Ol-Px hornblendite	Hornblende gabbro			Quartz gabbro				
Sample	E1	E5-e	E4	20608-e	LC-35	BLC-1A	LC-9	E2-e	W1
Hf	0.6	1.7	1	2	3	2	4	15	2
Ta	< 0.1	0.2	0.2	0.2	–	4.02	–	0.4	0.6
W	< 1	10	2	3	0.34	1.63	0.26	< 1	< 1
Tl	< 0.1	< 0.1	0.2	< 0.1	–	–	–	0.3	0.1
Pb	10	< 5	10	< 5	4.95	7.19	6.22	32	13
Bi	< 0.4	0.4	< 0.4	0.6	0.56	1.80	0.75	< 0.4	< 0.4
Th	0.5	2.2	4	8	9	5	4	5	3
U	0.3	0.5	0	1	1	2	2	2	1

Facies	Amp-bearing tonalite	Bt-bearing tonalite			Bt-bearing granodiorite				Granodioritic diatexite
Sample	LC-90	BLC-2	LC-178	LC-177	LC-176	LC-84	BLC-3	BLC-4	BLC-10
Major elements (wt.%)									
SiO_2	52.23	59.53	57.57	–	65.29	64.21	–	–	64.90
Al_2O_3	15.43	12.52	15.46	–	13.84	14.74	–	–	14.93
Fe_2O_3t	9.38	9.76	9.23	–	6.78	5.73	–	–	6.20
MnO	0.14	0.17	0.13	–	0.13	0.11	–	–	0.13
MgO	4.55	5.27	3.07	–	2.01	2.41	–	–	2.33
CaO	8.15	7.23	7.27	–	3.74	4.62	–	–	3.08
Na_2O	2.12	2.02	2.42	–	2.62	3.57	–	–	3.25
K_2O	1.60	0.97	1.77	–	3.70	2.41	–	–	3.33
TiO_2	1.16	0.94	1.34	–	0.90	0.84	–	–	0.86
P_2O_5	0.50	0.35	0.96	–	0.40	0.61	–	–	0.06
LOI	4.37	1.61	1.42	–	0.86	1.04	–	–	1.69
Total	99.63	100.37	100.65	–	100.25	100.29	–	–	100.76
Mg#	52.20	54.85	42.80	–	39.95	48.61	–	–	45.79
Trace elements (ppm)									
Sc	27.54	25.47	20.87	30	19.78	18.58	14	17	14.34
Be	4.30	2.29	2.19	4	2.66	5.38	4	4	3.34
V	234	238	109	190	95	167	113	130	95
Cr	97	135	39	74	16	3	59	74	23
Co	37	44	30	14	30	23	3	7	28
Ni	55	60	17	8	6	11	4	14	16
Cu	27.31	34.13	27.13	25.72	72.31	47.95	18.16	24.64	32.60
Zn	167.87	139.32	102.81	199.54	103.15	80.89	72.89	123.68	94.89
Ga	25.92	10.29	11.03	13.60	13.94	12.26	11.29	16.44	14.58
Ge	–	–	–	–	0.06	0.08	–	–	0.29
As	–	–	–	–	–	–	–	–	–
Rb	72	36	107	–	114	120	–	–	119
Sr	301	188	194	–	120	188	–	–	168
Y	34	39	23	–	32	39	–	–	48
Zr	536	277	156	–	300	404	–	–	354
Nb	9	7	9	–	10	17	–	–	13
Mo	0.82	0.45	0.84	0.82	0.50	0.15	0.49	0.44	0.90
Ag	1.32	2.56	1.06	1.45	1.68	2.01	2.30	2.09	2.53
In	0.77	0.53	0.31	0.46	0.57	0.65	0.49	0.68	1.30
Sn	2.49	3.58	1.49	1.85	2.06	1.94	2.47	3.07	2.52
Sb	1.00	0.84	0.79	0.89	0.74	0.60	0.71	0.91	1.45
Cs	19.15	3.83	37.58	219.21	8.18	12.27	8.14	9.10	12.48
Ba	716	246	260	–	423	235	–	–	696
La	61.74	23.21	31.94	16.10	69.51	155.81	91.34	105.72	123.23
Ce	149.94	61.10	72.29	46.81	174.23	311.36	189.99	211.60	240.95

(*continued on next page*)

Table 3 (*continued*)

Facies	Amp-bearing tonalite	Bt-bearing tonalite			Bt-bearing granodiorite				Granodioritic diatexite
Sample	LC-90	BLC-2	LC-178	LC-177	LC-176	LC-84	BLC-3	BLC-4	BLC-10
Pr	17.99	8.31	8.49	6.76	18.09	31.95	20.59	23.37	26.92
Nd	74.22	37.80	37.04	33.88	73.71	125.00	82.20	94.50	104.62
Sm	10.72	6.10	5.89	7.47	11.32	16.83	10.96	13.92	14.74
Eu	3.46	1.75	2.09	2.03	2.75	3.63	2.70	3.15	3.96
Gd	11.32	7.41	7.69	11.18	13.48	18.43	12.36	15.52	16.17
Tb	1.51	1.10	1.01	1.75	1.82	2.19	1.51	1.98	2.58
Dy	8.24	6.39	5.60	11.33	9.64	11.31	7.72	9.95	9.94
Ho	1.60	1.28	1.03	2.25	1.81	1.97	1.37	1.73	2.33
Er	4.48	3.71	2.99	6.40	5.22	5.38	3.84	4.58	4.82
Tm	0.61	0.52	0.36	0.89	0.72	0.73	0.51	0.57	1.27
Yb	3.41	2.93	2.12	4.75	4.28	4.34	3.08	3.24	3.59
Lu	0.59	0.50	0.35	0.81	0.81	0.83	0.57	0.58	1.32
Hf	11	7	4	–	8	10	3	3	9
Ta	–	0.51	–	–	–	0.28	0.33	0.83	1.17
W	0.67	0.57	0.43	0.67	0.23	0.35	0.92	0.66	1.25
Tl	–	–	–	–	–	–	–	–	–
Pb	12.00	4.97	7.84	10.58	13.24	9.03	15.02	15.87	13.20
Bi	0.66	0.61	0.81	1.41	0.35	0.41	0.39	0.33	1.08
Th	11	3	10	–	19	36	–	–	18
U	2	1	2	–	3	4	–	–	3

4.5.2. Trace elements

As expected, the mafic and ultramafic rocks have higher abundances in compatible elements (Ni, Cr, Sc, V), but lower concentrations of incompatible elements than the tonalitic and granodioritic facies.

In the mafic rocks, the concentration of compatible elements Ni and Cr is scattered, and they show two types of values for low SiO_2 contents (Fig. 10a). This reflects that, excluding the cumulate rocks and some samples of hornblende gabbros, the abundance of Cr and Ni in some mafic rocks is lower than in the primitive arc magmas, and therefore that these elements were incorporated into early crystallizing minerals such as Ol, Cpx, Pn and Spl, which are present in the cumulates with high Ni, Cr and Mg#.

The total concentrations of incompatible trace elements (including REE) are minor in the ultramafic cumulate (Ol-Px hornblendite facies) and maximum in the Bt-bearing granodiorite facies. This means that the total concentration increases proportionally with the SiO_2 content (Fig. 10b and c).

In general terms, extended trace element diagrams (Fig. 10b) clearly show the enrichment in some incompatible elements (Rb, Th, U, K) and negative anomalies in Nb respect to Th and Ce, features that are generally interpreted as typical of subduction-related volcanic arc rocks (Pearce, 1982, 1996; Baier et al., 2008). Besides, the rocks of LCPC are notably poor in Sr and even more in Y, resulting in low Sr/Y ratios (between 3.5 and 13.5), and are strongly enriched in Pb compared to Ce (Fig. 10b).

The Ol-Px hornblendite facies has significantly lower Ba, Rb, Th, and Sr than the gabbros, tonalites and granodiorites (Fig. 10b) according to the absence of plagioclase.

The Th, U, K and La elements are much more abundant in granodiorites than in tonalites and gabbros. In these last ones, the concentrations of the mentioned elements do not differ substantially. The appearance of K-feldspar in Bt-bearing granodiorites is considered the main cause of these discrepancies.

The distinction among facies is clearly observed from contrasting rare earth elements abundances shown in chondrite-normalized (REE_{C-N}) patterns. The facies display different bands of REE_{C-N} profiles that change as the total amount of rare earth elements (ΣREE) increases (Fig. 10c). Hence, with increasing ΣREE contents, the pattern varies from little-fractionated [$(La/Yb)_{C-N} = 2.4$] in Ol-Px hornblendite facies to quite-fractionated with $(La/Yb)_{C-N} = 19.3 \pm 5.8$ in Bt-bearing granodiorite facies, and from patterns showing the absence of Eu-anomaly ($Eu/Eu^* = 0.85$) to patterns having a small negative Eu-anomaly ($Eu/Eu^* = 0.7$), that would indicate that plagioclase was partially fractionated (Fig. 10c).

In hornblende gabbro facies, the REE_{C-N} patterns are separated from the Ol-Px honblendite facies pattern, and therefore the ΣREE are increased from 16 ppm (in Ol-Px hornblendites) to 61 ± 15 ppm (in hornblende gabbros) (Fig. 10c).

4.6. Zircon U–Pb dating

Isotope data and dates for the Amp-bearing tonalite facies of the LCPC (western Puertas Coloradas pluton) are presented in Table 2. The analyzed zircon crystals of this facies (sample LC-90) are generally euhedral to subhedral, with Th/U ratio between 0.4 and 1.3. Their sizes range from 200 to 500 μm in length, showing oscillatory internal zoning. Some crystals exhibit cores with discordant contours with respect to the zoning of crystal magmatic growth, indicating that these are inherited cores (Fig. 11a). It is important to point out that the host rock of these zircons has suffered hydrothermal alteration, showing significant loss of Pb in some analyzed zircons, reason why these analyses are not included in the calculation of crystallization final age.

Several ages can be observed in the $^{206}Pb/^{238}U$ versus $^{207}Pb/^{235}U$ conventional concordia diagram (Fig. 11b), which corroborate the inheritance. Final age of crystallization determined for the Amp-bearing tonalite facies is 470.4 ± 8.1 Ma (typically Famatinian), calculated

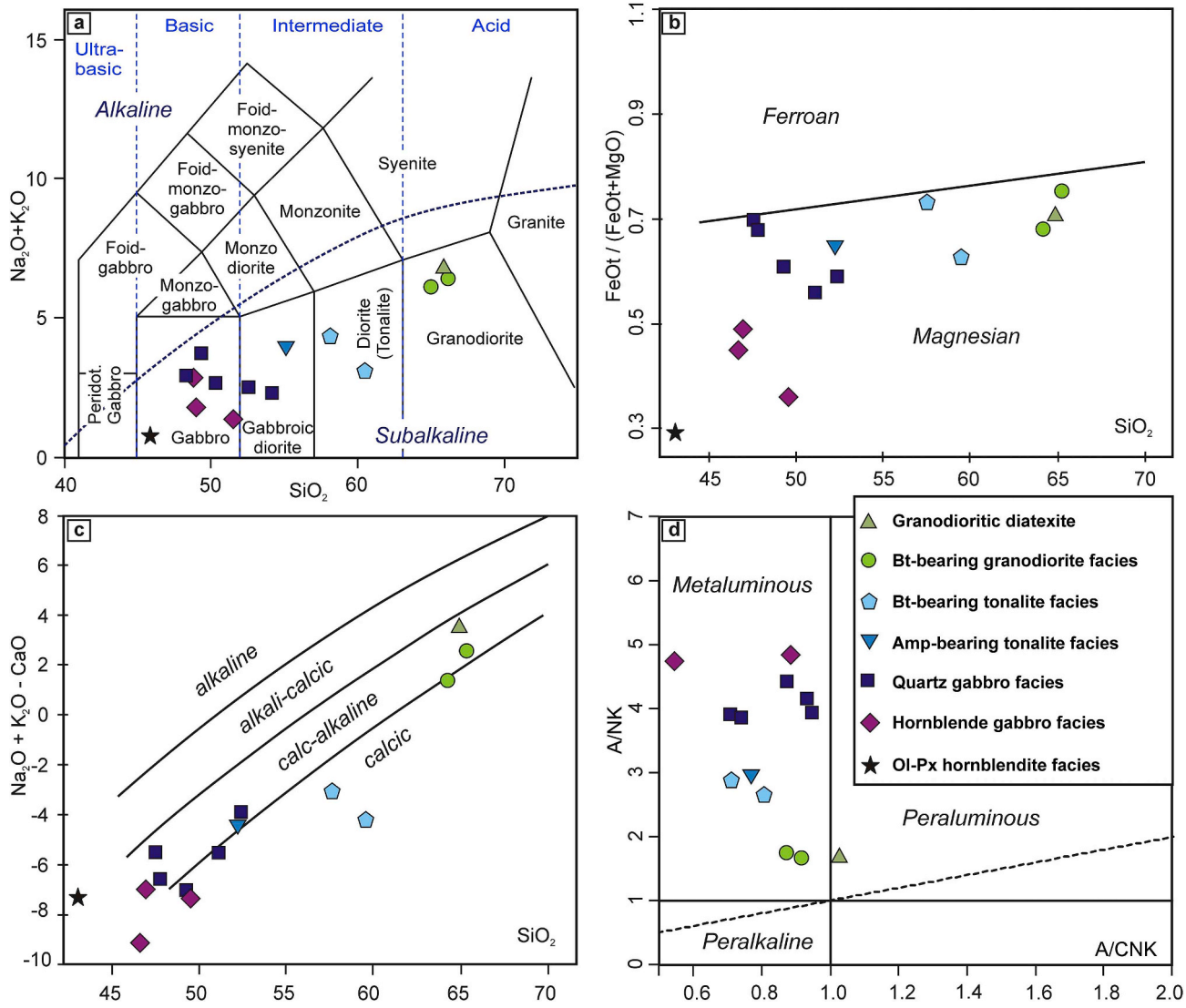

Fig. 8. a) TAS diagram for plutonic rocks (LeMaitre, 2002) with the divisions of alkaline and subalkaline series proposed by Irvine and Baragar (1971). b) Fe index and c) MALI index (after Frost et al., 2001). d) Alumina saturation index (after Shand, 1943).

through error-weighted average of a group of nine best concordant analyses (Fig. 11c). Inherited zircon cores give $^{206}Pb/^{238}U$ ages of 531 ± 10 Ma, 657 ± 41 Ma, 869 ± 13 Ma, 904 ± 22 Ma and 907 ± 17 Ma, which we interpret reflecting detrital zircons from the assimiladed metasedimentary source in the magma (Fig. 11a and b).

Ages less than 455 Ma (with a peak at 440 Ma) are discordant in the $^{206}Pb/^{238}U$ versus $^{207}Pb/^{206}Pb$, and interpreted as an isotopic system partially reset by loss of Pb due to post-magmatic hydrothermal processes.

5. Discussion and interpretations

5.1. Geochemical comparison with the famatinian typical arc section

The studied plutonic rocks show a calc-alkaline signature and major and trace elements contents, comparable with rocks from the axis of the Famatinian magmatic arc in the Sierra de Valle Fértil-La Huerta (Otamendi et al., 2009), located 260 km to the NW. Besides, these rocks are the less differentiated rocks in the western Sierra de San Luis (Sato et al., 1996; Llambías et al., 1998; Brogioni et al., 2005; López de Luchi et al., 2007; Morosini, 2011) and resemble the sequence (I-type) described in the Sierras de Chepes and Los Llanos, in La Rioja (Pankhurst et al., 1998; Dahlquist et al., 2005). Besides, the LCPC evolutionary trends overlap considerably with those of the rocks (mafic, intermediate and silicic) exposed arc in the Sierra de Valle Fértil (Fig. 9).

The incompatible and REE elements patterns (Fig. 12a, d) show that cumulate facies of the LCPC (Ol-Px hornblendites), fit in almost completely with the cumulate rocks of the deep Famatinian arc exposed in the sierra of Valle Fértil (Otamendi et al., 2009). In hornblende gabbro facies, the patterns fit well with the mafic rocks (< 50 wt% SiO2) from Valle Fértil-La Huerta, although a small difference is observed in the HREEs [$(La/Yb)_{C-N}$ = 3.0 ± 1.4 in Valle Fértil versus 4.6 ± 0.9 in LCPC)]. Besides, hornblende gabbros have less Ba, Sr, Ti (Fig. 12a, d). These similarities correspond to the averages oceanic and continental primitive arc basalts (Kelemen et al., 2003), reflecting that the hornblende gabbros facies of the LCPC has an arc origin (Fig. 12d).

The LCPC and Valle Fértil intermediate rocks have a very similar trace element pattern (Fig. 12b), but with differences in total REEs (ΣREE = 195 ± 70 ppm in LCPC versus 87 ± 36 ppm in Valle Fértil). Besides, REE_{C-N} contents of the LCPC are comparatively similar with diorites and tonalites from the Cordón del Realito (Brogioni et al., 2005) located in the west of the Sierra de San Luis (Fig. 12e). In both, granodioritic (siliceous) rocks of Valle Fértil and granodiorites (acidic) of the LCPC, moderate negative Eu/Eu* anomalies are observed

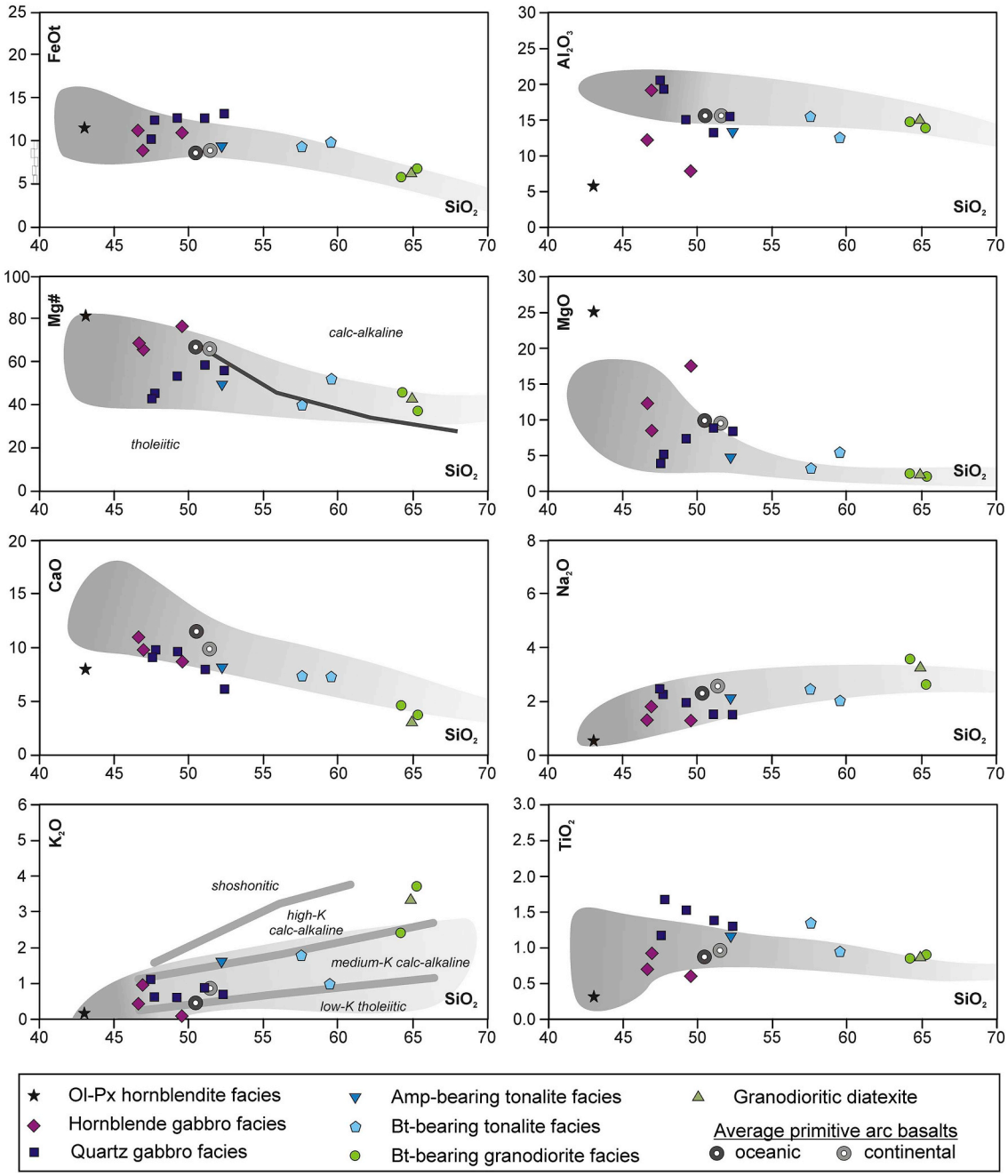

Fig. 9. Major element composition of each facies projected versus SiO_2 content. The gray fields reflect the compositional trends for the set of mafic, intermediate and silicic units of the famatinian arc exposed in Sierra de Valle Fértil-La Huerta (according to Otamendi et al., 2009). In the Mg-number versus SiO_2 diagram, the line dividing tholeiitic and calc-alkaline fields is from Miyashiro (1974) but after converting FeO*/MgO ratio to Mg-number. The K_2O diagram shows the boundaries among low-K, medium-K, high-K and shoshonitic series after Peccerillo and Taylor (1976). Composition of average primitive continental and oceanic arc basalts are taken after Kelemen et al. (2003).

(0.74 ± 0.16 in Valle Fértil, and 0.7 ± 0.03 in the LCPC), which would indicate plagioclase fractionation. On the other hand, the higher slope in Bt-bearing granodiorites [$(La/Yb)_{C-N}$ = 19.3 ± 5.8)] compared to the silicic unit of Valle Fértil [$(La/Yb)_{C-N}$ = 6.1 ± 1.9)], would suggest some differences in the melting conditions of the source (Fig. 12f), most likely a less volumetric participation of the I-type magmas in the metasedimentary environment.

5.2. Geochemical discrimination

All LCPC rocks can be grouped as magnesian granitoids (cordilleran), which rules out the possibility of an A-type anorogenic origin (Frost et al., 2001). These characteristics were also observed in an important group of outcropping magmatic rocks in the Serrania de La Aguada, Sierra de Comechingones, in the Conlara Metamorphic Complex (Cristofolini et al., 2017).

Using the geochemical discrimination proposed by Batchelor and Bowden (1985), the Bt-bearing tonalites facies derived from mantle fractionate magmas or pre-collisional-plate (Fig. 13a). In the same way, the ternary Ba–Rb–Sr diagram (El Bouseily and El Sokkary, 1975) clearly shows that the LCPC rocks are poorly differentiated from their source because of their reduced concentrations in Rb with respect to Sr and Ba (Fig. 13b). However, the intermediate and acidic units of the LCPC are little more evolved than those of the exposed arc in Valle

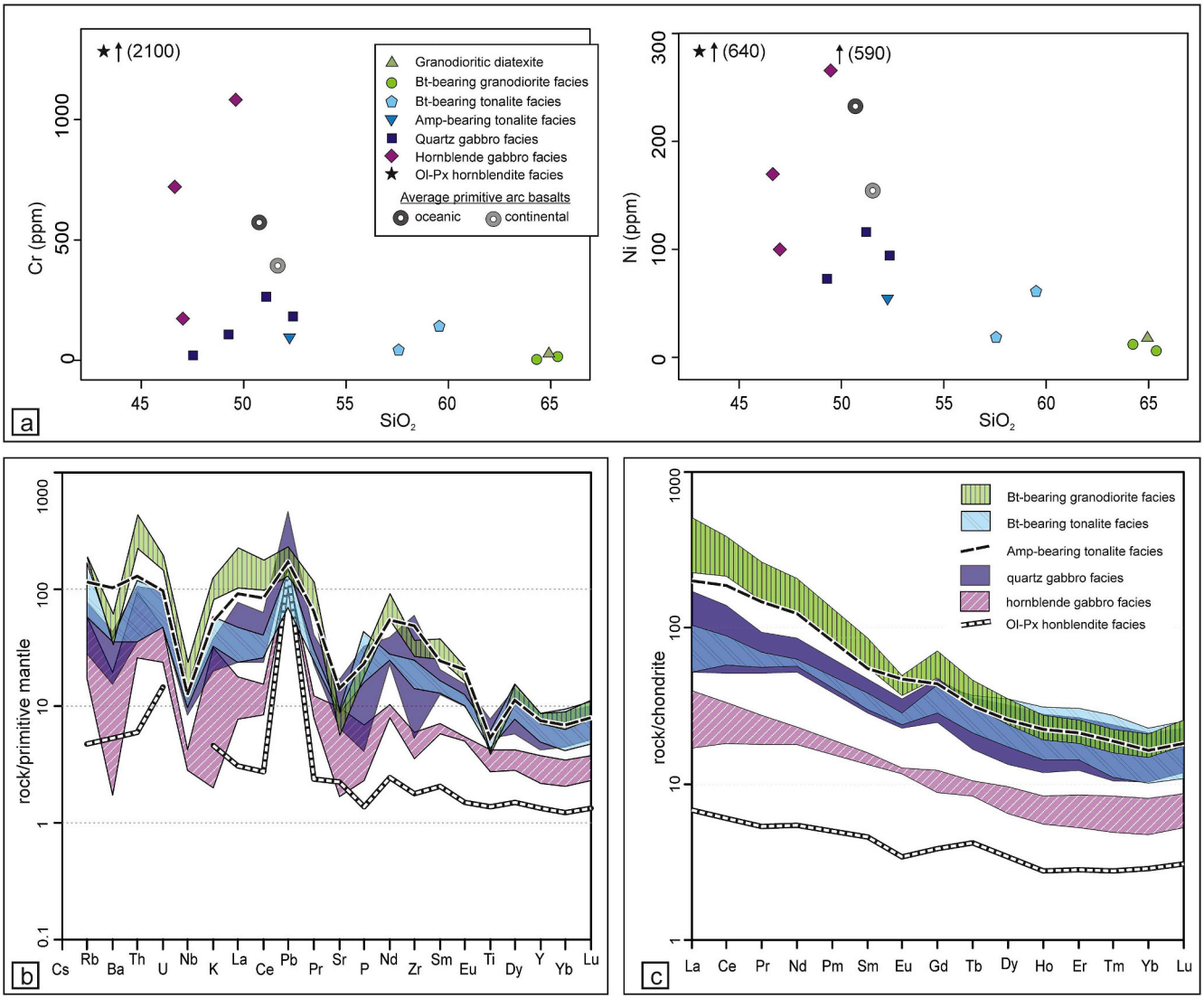

Fig. 10. a) Cr and Ni vs. SiO_2 binary diagrams. Averages of primitive arc basalts are taken after Kelemen et al. (2003). b) Spider diagrams normalized to the primitive mantle of Sun and McDonough (1989) for LCPC. c) REE diagrams normalized to chondrite of Boynton (1984).

Fértil, and this is also reflected in the highest total concentrations of REEs.

The tectonic discrimination diagram of Pearce et al. (1984) indicates that all the rocks of the LCPC are linked to a volcanic arc (Fig. 13c). The Pb enrichment compared to Ce in the basic and intermediate rocks of LCPC suggests a possible Pb input from subduction-derived fluids (e.g., Elliott et al., 1997; Hermann et al., 2006). In turn, Th and U elements are enriched in all the rocks of the LCPC with respect to the Valle Fértil rocks, which may be a symptom of higher crustal contamination (Fig. 12a, b, c).

The low Sr/Y values in all the rocks of the LCPC indicate that plagioclase was a stable phase that fractionated Sr at the source, probably in the lower crust, where the processes of differentiation and assimilation begin to be effective (Chiaradia, 2015). This behavior is consistent with those observed in all the exposed rocks in Valle Fertil (Otamendi et al., 2009), as well as the rest of the Ordovician plutonic rocks exposed in other sites of the Sierra de San Luis (López de Luchi et al., 2007; Morosini, 2011; Morosini et al., 2017).

Sr/Y is a common qualitative indicator of the average crustal pressure or depth, at which magmatic differentiation occurred, where a larger Sr/Y ratio signifies a higher pressure or depth (Chapman et al., 2015). Low Sr/Y values (< 13), for magmas with concentrations less than 10 wt% MgO, are statistically more common of arcs < 20 km thick, where the magmatic differentiation occurs in the stability field of plagioclase. In contrast, high Sr/Y values (15–40), for magmas with the same concentration of MgO (< 10 wt%), are statistically common of arcs > 30 km thick, where magmatic differentiation occurs outside the stability field of plagioclase and within the amphibole ± garnet (Chiaradia, 2015). Therefore, we can infer that rocks of LCPC (Sr/Y = 7 ± 3) would have started to fractionate at depths no higher than 25 km (< 0.7 GPa), because plagioclase starts to be very unstable from those depths onwards (e.g., Patiño Douce and Beard, 1995). In contrast, the Devonian post-orogenic granites in Sierra de San Luis show average of Sr/Y = 22 ± 12, according to Lopez de Luchi et al. (2007) and Morosini et al. (2017) data set. They would have been separated from their metasedimentary source (in granulite facies) at depths higher than 30 km (> 0.8 GPa), in the garnet stability field (Fig. 13d). This interpretation is in favor of a model of melting and emplacement after a tectonic exhumation with crustal thickening due to a collision stage (Morosini et al., 2017). This allows us to deduce that there was a thin crust at the time when the LCPC was fractionated, indicating that this process took place in a pre-collisional arc stage, probably linked to an extensional and hot retro-arc setting (e.g. Brogioni, 1994; Hauzenberger et al., 2001). The low-pressure and high-temperature

conditions determined in the studied zone are similar to those of the Famatinian retro-arc zones (Larrovere et al., 2011).

5.3. Differentiation processes

5.3.1. Mass balance constraints on petrologic processes

In order to understand the petrological processes that produce the different igneous lithological units, a mass balance was used through least squares multiple-regressions to try reproducing the differentiation of LCPC. Then models are further tested through trace element approximations. Mass balance models combined whole-rock major and trace elements chemistry with measured mineral compositions.

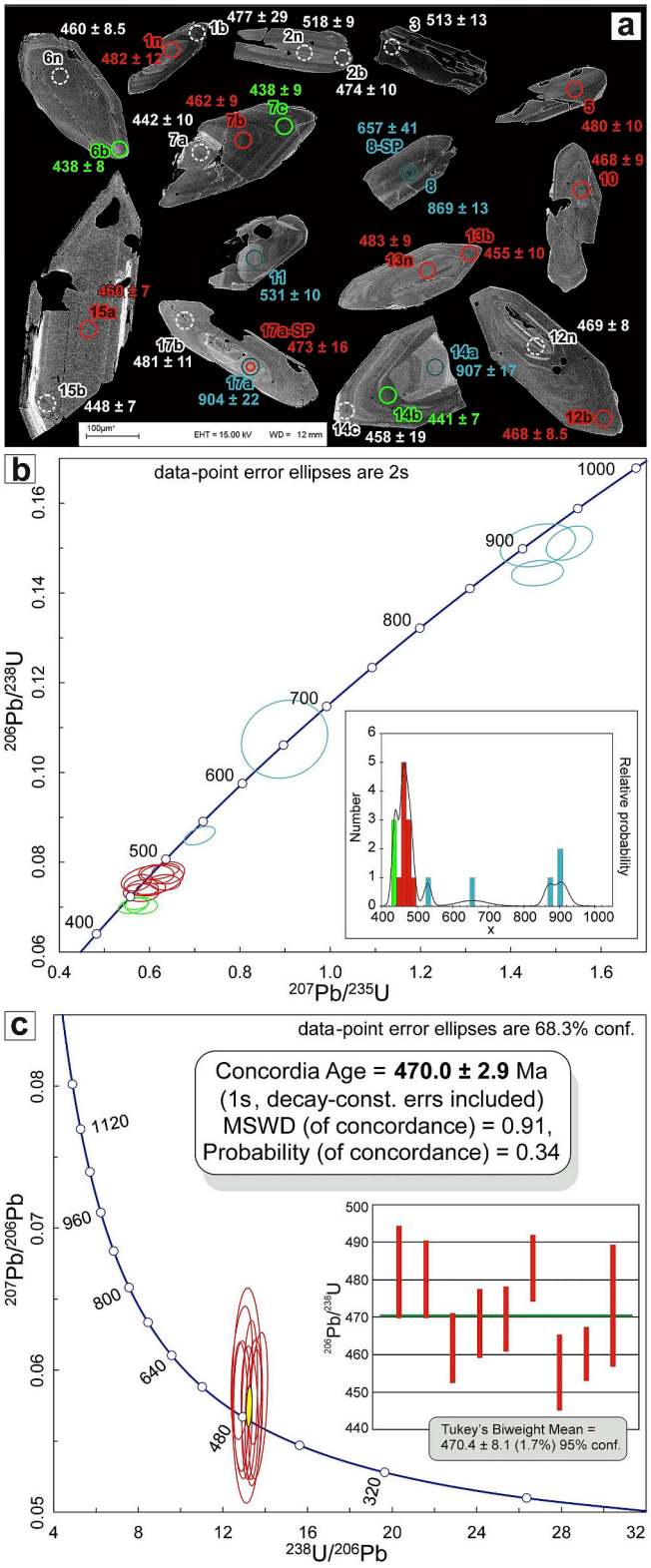

Fig. 11. a) BSE image of the analyzed zircons in the sample LC-90 (Amp-bearing tonalite facies). The dashed white-spots correspond to discordant ages (not used in the calculations). The red-spots represent the ages of crystallization used in the calculation of the final age represented in (c). The green-spots represent young discordant ages interpreted as hydrothermal alteration. While the blue-spots are ages of inherited cores (assimilated rock?). b) Conventional concordia diagram. Errors are shown as ellipses at the 2s level. Three groups of ellipses are shown, that corresponding to Ordovician crystallization (red-ellipses), another group belongs to ages from inherited cores (blue-ellipses), and one representing discordant ages for Pb loss (green ellipses) that have not been weighed when the final age was determined. c) Tera-Wasserburg diagram (errors are shown as ellipses at the 1s level). The crystallization $^{206}Pb/^{238}U$ mean age is also shown. The results were plotted with Isoplot/Excel (Ludwig, 2003). (For interpretation of the references to color in this figure legend, the reader is referred to the Web version of this article.)

Based on field evidence that shows cumulate textures and structures in Ol-Px hornblendite and hornblende gabbro facies, mineral chemistry in olivine from Ol-Px hornblendite suggests that rocks are in equilibrium with quartz gabbro facies and the major elements of these rocks agree with arc basalts. This facies could be the more primitive preserved magma in LCPC; therefore mass balance models will try to reproduce a scheme of differentiation processes by step from quartz gabbro to Bt-bearing granodiorite that includes all the rocks in the plutonic complex.

The first approach involves a crystal fractionation (CF) model using major elements in a closed system by this equation:

$$C_0 = FC_l + (1 - F)C_s \quad (1)$$

Where C_0 is the concentration from parental magma, F is the mass of liquid fraction, C_s is the concentration of cumulates mineral and C_l is liquid concentration.

Results from inverted crystal fractionated models using the low silica quartz gabbro (sample W1) fail to reproduce an Amp-bearing tonalite, fractionating Hbl, Pl (An_{56} or An_{80}), Mag and Ilm ($\Sigma R^2 = 1.16$), because Na_2O, Ca_2O and K_2O contents are away from the model (Table 4, model 1). In contrast, it was possible to reproduce ($\Sigma R^2 = 0.06$) an Amp-bearing tonalite from a high silica quartz gabbro (sample BLC-1a), removing 44 wt % Hbl, 6 wt % Pl (An_{50}) and 2 wt % Ilm (Table 4, model 2). Also, it was a success ($\Sigma R^2 = 0.74$) to derive an Amp-bearing tonalite from a high silica Quartz gabbro (sample LC-35), subtracting 35 wt% Cum, 14 wt% Pl (An_{50}) and 2 wt% Ilm (Table 4, model 3). The cumulates calculated with models 2 and 3 (Table 4) have similar major elements contents between them and also show very similar concentrations with the hornblende gabbro facies (sample 20608-e; Table 3). The crystal fractionation model (Table 4, model 4) to derive a Bt-bearing tonalite (sample LC-178) from an Amp-bearing tonalite (sample LC-90) by suppressing 21 wt % Hbl and 7 wt % Pl (An_{70}) was possible to reproduce ($\Sigma R^2 = 0.18$). Instead, it not was possible to reproduce a Bt-bearing granodiorite derived from a Bt-bearing tonalite through crystal fractionation of Bt, Pl and Mag, because the concentration in alcalis elements, CaO and MgO, is away from models ($\Sigma R^2 = 6.2$).

In order to test the results obtained by mass balance through least squares multiple-regressions, equation (2) was used, to model behaviors of trace elements by batch crystallization (BC):

$$C_i^l / C_i^0 = \frac{1}{(D_i^{s/l} + F(1 - D_i^{s/l})} \quad (2)$$

Where C_i^l is the liquid derived concentration of element i, C_i^0 is the initial concentration of element i, and D is the bulk distribution

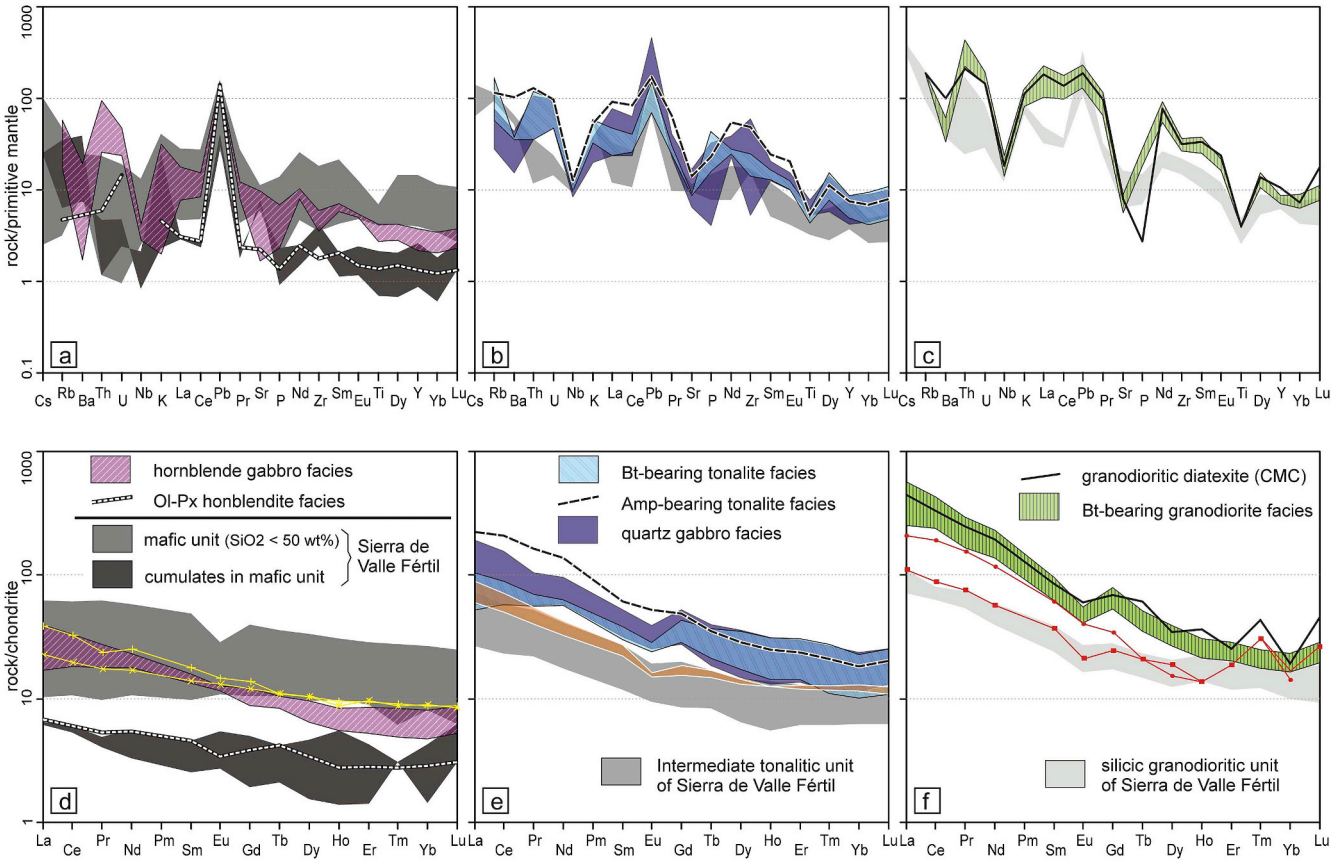

Fig. 12. Comparison of trace elements between the rocks of the LCPC and those of Valle Fértil-La Huerta (Otamendi et al., 2009). a-b-c) spider diagrams normalized to the primitive mantle of Sun and McDonough (1989). d-e-f) REE diagrams normalized to chondrite of Boynton (1984). Mafic, intermediate and silicic units of sierra de Valle Fértil-La Huerta (Otamendi et al., 2009) in grayscale are plotted. The yellow lines in (d) correspond to the oceanic (x) and continental (+) primitive arc basalts taken after Kelemen et al. (2003). The orange field in (e) corresponds to intermediate rocks (SiO2 < 63 wt%) from the west of the Sierra de San Luis (Brogioni et al., 2005). The red lines in (f) correspond to the average of seven metawackes (boxes) and one metapelite (circles) taken after López de Luchi et al. (2003). (For interpretation of the references to color in this figure legend, the reader is referred to the Web version of this article.)

coefficient (Kd) solid/liquid in i element. Kd was obtained from Claeson and Meurer (2004) compilation for gabbros and GERM Kd database (http://earthref.org/database team – Roger Nielsen) for tonalites.

According to the result obtained by major element models, bulk partition coefficients were calculated for the different models. Then equation (2) was used to test the model 2, that derives an Amp-bearing tonalite from a high silica quartz gabbro by fractioning a 51% of solid composed by an 86 wt% Hbl, 12 wt% Pl and 2 wt% Ilm. This model fails to reproduce contents in Ba, Rb, La, Th, U, Pb, MREE, HREE and Zr, because, in general, they are below content in comparison with Amp-bearing tonalite, but has a good correlation with Cs, Nb, Sr, and Pb (Fig. 14a). The model 3 fails to reproduce Ba, La, Pb, Sr, MREE and HREE content. Instead, it has similar concentrations in Cs, Rb, Th, U, Nb, Ce, and Pr. The crystal fraction model 4 (Fig. 14b) has a good correlation in contents of Cs, Rb, U, Nb, Sr and HREE; although it fails to reproduce Ba, Th, Pb, Zr, LREE, MREE. Attending to high contents in REE and allanite presence in Amp-bearing tonalite, a fraction of this mineral in a minor part (0.5 wt %) was tested. Adding this mineral to the crystal fraction model had an improvement in Th and REE correlation (Fig. 14b), mainly in LREE.

The models were also tested by fractional crystallization (FC) using Rayleigth equation (3):

$$\frac{C_l^i}{C_0^i} = F^{(D-1)} \tag{3}$$

Concentration differences in HREE and MREE, using FC equation in model 2, are larger than in BC model, with respect to sample (LC-90), where they are more depleted. In contrast Ba, La, Rb, Th and LREE have better correlation than BC, but contents do not reproduce the sample. On the other hand, like using BC, Cs, Pb, Nb and Sr have good correlation. So, in general, using FC and BC equation in model 4, similar results don't have a good correlation with the sample, unless allanite is added.

Given differences in the results between models (FC and BC) and sample, attending to field observations, that show a more complex process than crystal fraction, assimilation was tested together with crystal fraction (AFC), using equation (4) from De Paolo (1981):

$$\frac{C_m}{C_m^0} = f' + \frac{r}{(r + D - 1)}\frac{C_a}{C_m^o}(1 - f') \tag{4}$$

where $f' = F^{-z}$

and $Z = \frac{r+D-1}{r-1}C_m^0$ is initial concentration in parental magma, C_m is concentration in derived liquid magma, C_a is concentration in assimilated rock and r is assimilation/fractional crystallization ratios.

AFC models were trialed with two different contaminants (diatexite and metapsammite rock), attending to host rock, and no major difference was found. A direct model was built to reproduce different assimilation/crystal fraction ratios (r). Initially, AFC was modeled from quartz gabbro (sample BLC-1a) to derive Amp-bearing tonalite. It is possible to note that a low r ratio (0.1) AFC produces an HREE depletion and high La/Yb relation. In contrast, high r ratio (0.5) produces minor depletion in LREE and minor La/Yb relation than low r ratio. Correlation between Amp-bearing tonalite sample and models at low fraction part (F = 0.9 to 0.7) in high r ratio model was an improvement with respect to CF and BC, especially in Ba, La, Rb, Pb, MREE and LREE,

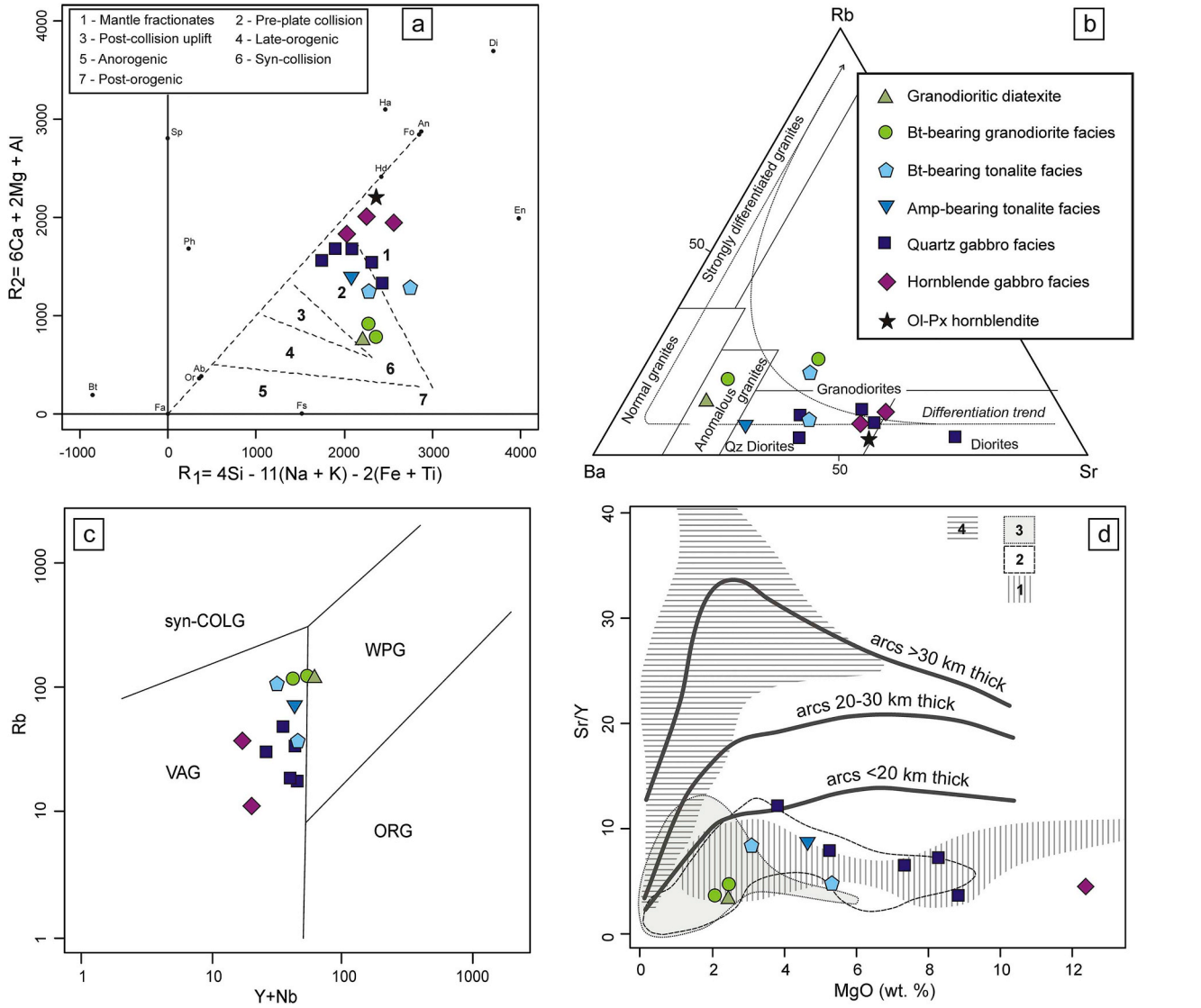

Fig. 13. a) R1 versus R2 diagram of Batchelor and Bowden (1985). b) Ternary Ba–Rb–Sr diagram (El Bouseily and El Sokkary, 1975). c) Tectonic discrimination diagram of Pearce et al. (1984). d) Sr/Y versus MgO (w.t.%) diagram after Chiaradia (2015). The black lines represent averages of median MgO and Sr/Y values for arcs < 20 km, > 30 km, and 20–30 km thick respectively. The fields represent: 1) Ordovician magmatism of Valle Fértil-La Huerta (Otamendi et al., 2009); 2) Ordovician Valle de Pancanta plutonic complex, southwest of Sierra de San Luis (Morosini, 2011; Morosini et al., 2017); 3) Ordovician plutons from Sierra de San Luis (López de Luchi et al., 2007); and 4) Devonian postorogenic plutons from Sierra de San Luis (López de Luchi et al., 2007; Morosini et al., 2017).

but contents in MREE and LREE were not possible to reproduce (Fig. 14a). Therefore, high contamination (r ~ 0.5) and a low fraction of crystal in an AFC model reproduces better an Amp-bearing tonalite from a quartz gabbro than CF or BC models. Therefore, we assume that this was the predominant process.

Secondly, AFC was tested to derive a Bt-bearing tonalite from an Amp-bearing tonalite. Different r ratios were used, to evaluate contamination rate behavior, and the principal differences in these models are: 1) La/Yb relation, where high r ratio is smaller at high part fraction and 2) Hf depression was steeper at low r ratio. AFC model fails to reproduce contents in Ba, La, Ce, Pb, Pr, Nd, Zr and HREE. So, AFC models are inadequate to derive a Bt-bearing tonalite and seem most probably a CF or BC with allanite to reproduce them (Fig. 14b).

Finally, alternative methods were tested through least squares multiple-regressions to reproduce a Bt-bearing granodiorite that do not involve CF from a Bt-bearing tonalite. Firstly, it was trialed to derive a Bt-bearing granodiorite from a Bt-bearing tonalite or an Amp-bearing tonalite by assimilation of metapsammite from CMC. Both models fail to reproduce it, because concentrations in alumina, Na_2O, Fe_2O_3 and MgO are away from these models. Secondly, CF was tested from an Amp-bearing tonalite and it was successful in reproducing a Bt-bearing granodiorite by fractioning 35 %wt. Hbl, 18 %wt. Pl and 1 %wt. Ilm, but the quadratic sum of residuum is nearly 1. In order to prove this, last model trace element approximation was tested by CF equation (3) and it has many differences with sample (LC-176), essentially in Cs, Ba, Ce, Sr, Zr, Sc, Cr, Ni and LREE concentrations, although reasonably good correlation with Rb, Th, U, La, Pb, Sm, Nd and Eu. Concerning the discrepancy between sample and CF model, an AFC approach was tested with metapsammite like a contaminant. Results from AFC models show that similarly to previous models, a higher r (0.5) value and a minor solid fraction (F = 0.9–0.8) are needed than in CF to reproduce a Bt-bearing granodiorite, however, AFC also has a major discrepancy like CF, especially in Cs, Ba, Zr and LREE in element correlation. However, this model has a good correlation in the same elements as CF with Sr.

5.3.2. *Evidences of multiple processes in the LCPC differentiation*

The relatively flat chondrite-normalized REE patterns (Fig. 10c) and

Table 4
Mass balance model calculations.

wt.%	facies		minerals				Model 1		
	Low silica Qz-gabbro	Amp-bearing tonalite	Amp	Pl (An_{56})	Mag	Ilm	Low silica Qz-gabbro	R^2	Cumulate
SiO_2	48.76	55.37	51.34	53.38	0	0	48.84	0.01	47.84
TiO_2	1.7	1.23	0.2	0	0	50	1.7	0	1.78
Al_2O_3	19.73	16.36	7.54	29.37	0	0	19.61	0.01	20.10
FeO	11.42	8.95	14	0.12	100	50	11.42	0	11.80
MnO	0.13	0.15	0.63	0	0	0	0.18	0	0.19
MgO	5.26	4.82	17.56	0	0	0	5.21	0	5.27
CaO	9.98	8.64	7.72	12.07	0	0	9.52	0.21	9.65
Na_2O	2.3	2.25	0.94	5.02	0	0	3.19	0.79	3.33
K_2O	0.63	1.7	0.07	0.04	0	0	0.27	0.14	0.046
P_2O_5	0.09	0.53	0	0	0	0	0.07	0	0
Coeff.		0.13	0.26	0.53	0.05	0.03	Sum R^2	1.16	100
	facies		**minerals**				**Model 2**		
wt.%	High silica. Qz-gabbro	Amp-bearing tonalite	Hbl	Pl (An_{50})	Ilm		High silica Qz-gabbro	R^2	Cumulate
SiO_2	50.76	55.37	45.42	54.75	0		50.73	0	45.13
TiO_2	1.57	1.23	0.63	0	50		1.52	0	2.05
Al_2O_3	15.51	16.36	13.25	28.96	0		15.58	0.01	14.68
FeO	11.84	8.95	15.35	0.06	50		11.88	0	14.61
MnO	0.16	0.15	0.43	0	0		0.11	0	0.36
MgO	7.51	4.82	11.86	0	0		7.5	0	10.12
CaO	9.87	8.64	11.44	10.8	0		9.86	0	11.02
Na_2O	2.02	2.25	1.39	5.38	0		1.91	0.01	1.81
K_2O	0.61	1.7	0.23	0.05	0		0.8	0.04	0.21
P_2O_5	0.15	0.53	0	0	0		0.11	0	0
Coeff.		0.5	0.44	0.06	0.02		Sum R^2	0.06	100
	facies		**minerals**				**Model 3**		
wt.%	High silica Qz-gabbro	Amp-bearing tonalite	Cum	Pl (An_{50})	Ilm		High silica Qz-gabbro	R^2	Cumulate
SiO_2	54.57	55.37	52.78	54.75	0		54.54	0	51.46
TiO_2	1.34	1.23	0.16	0	50		1.33	0	1.87
Al_2O_3	13.95	16.36	4.43	28.96	0		13.81	0.02	10.96
FeO	12.26	8.95	19.98	0.06	50		12.27	0	15.60
MnO	0.22	0.15	0.73	0	0		0.08	0.02	0.51
MgO	8.6	4.82	18.32	0	0		8.64	0	12.68
CaO	6.38	8.64	2.98	10.8	0		6.78	0.16	5.01
Na_2O	1.57	2.25	0.59	5.38	0		1.87	0.09	1.87
K_2O	0.72	1.7	0.03	0.05	0		0.66	0	0.04
P_2O_5	0.4	0.53	0	0	0		0.03	0.14	0
Coeff.		0.52	0.35	0.14	0.02		Sum R^2	0.43	100
	facies		**minerals**				**Model 4**		
wt.%	Amp-bearing tonalite	Bt-bearing tonalite	Amp	Pl	Ilm		Amp-bearing tonalite	R^2	Cumulate
SiO_2	55.37	58.57	44.29	50.55	0		55.38	0	45.56
TiO_2	1.23	1.36	0.87	0	50		1.23	0	0.90
Al_2O_3	16.36	15.73	13.35	31.66	0		16.36	0	17.62
FeO	8.95	8.45	15.95	0.12	50		8.95	0	12.36
MnO	0.15	0.13	0.77	0	0		0.25	0.01	0.59
MgO	4.82	3.12	12.13	0	0		4.83	0	9.21
CaO	8.64	7.4	10.62	14.18	0		8.56	0.01	11.41
Na_2O	2.25	2.46	1.8	3.44	0		2.39	0.02	2.18
K_2O	1.7	1.8	0.22	0.06	0		1.35	0.12	0.18
P_2O_5	0.53	0.98	0	0	0		0.7	0.03	0
Coeff.		0.73	0.21	0.07	0		Sum R^2	0.18	100

the low Sr/Y and $(Gd/Yb)_{C-N}$ in mafic rocks indicate a relatively shallow source without garnet in the residue. The behavior of the major elements in intermediate and felsic rocks could be explained by the presence of Fe–Ti oxides, amphibole, and plagioclase as the major fractionating phases, which has been proven through mass balance models in the preceding section.

The rise of a primitive (arc) parental magma through pulses of low volume in an environment highly impregnated with granodiorite anatectic melts, allowed the interaction of two types of sources that produced the set of zoned plutons in the Las Cañas-Puertas Coloradas area. In this context, AFC (fractional crystal with high rates of diatexites assimilation) reigned during the differentiation processes that gave rise to Amp-bearing tonalites from quartz gabbros, also allowing the development of hornblende gabbro residues. The ultramafic cumulus (Ol-Px hornblendites) must have been fractionated from a previous liquid, which when differentiated, gave rise to a magma compositionally equivalent to the quartz gabbro facies. The calculated Mg# of the liquids (using Fe–Mg Kd values for olivine/melt = 0.33; Roeder and Emslie, 1970) show that the forsterite crystals from the Ol-Px hornblendite facies crystallized in equilibrium with a melt having Mg# from 57 to 60. Such compositions are very similar to those of the high silica quartz gabbro facies, with whole-rock Mg# between 56 and 61 (calculated using samples LC-35, BLC-1A and LC-9).

Batch crystallization (BC) can be assumed as the process by which the Bt-bearing tonalites were differentiated from the previously fractionated Amp-bearing tonalites (Fig. 15a).

Our calculations indicate that a Bt-bearing granodiorite cannot be formed from a Bt-bearing tonalite under any differentiation process, not even AFC. However, the composition of a granodiorite can be reproduced from Amp-bearing tonalites fractionating high percentages of

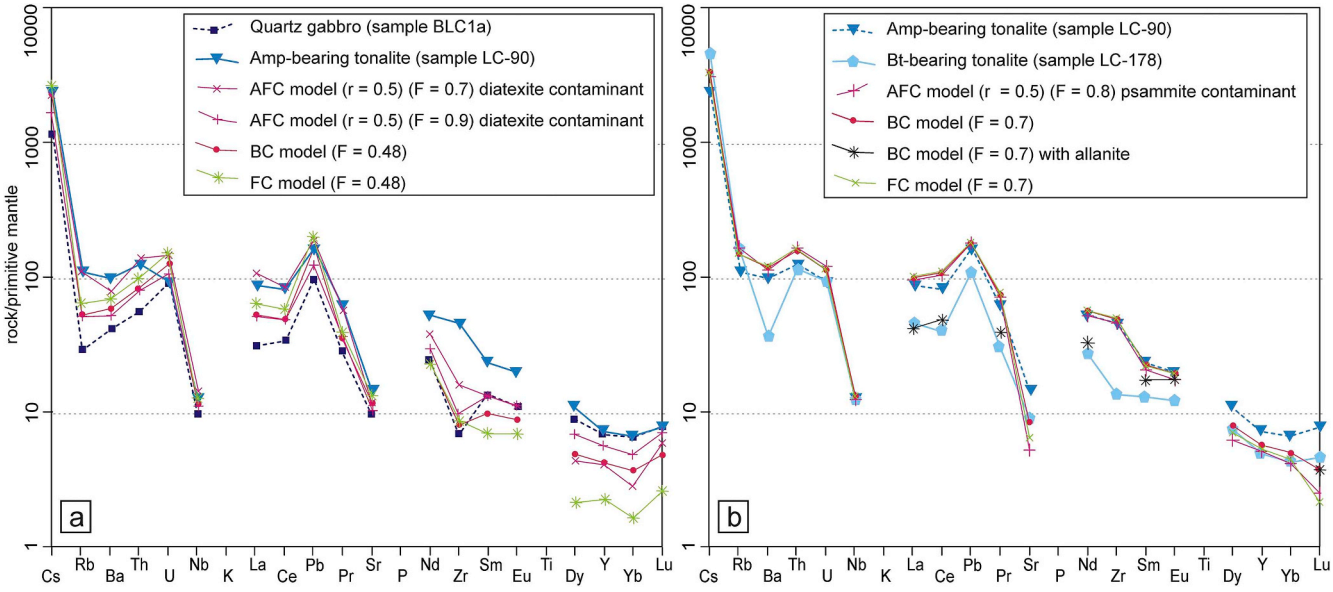

Fig. 14. Spider diagrams normalized to the primitive mantle of Sun and McDonough (1989). a) BC, FC and AFC, models to derive Amp-bearing tonalite from quartz gabbro. b) BC, CF and AFC to derive Bt-bearing tonalite from Amp-bearing tonalite.

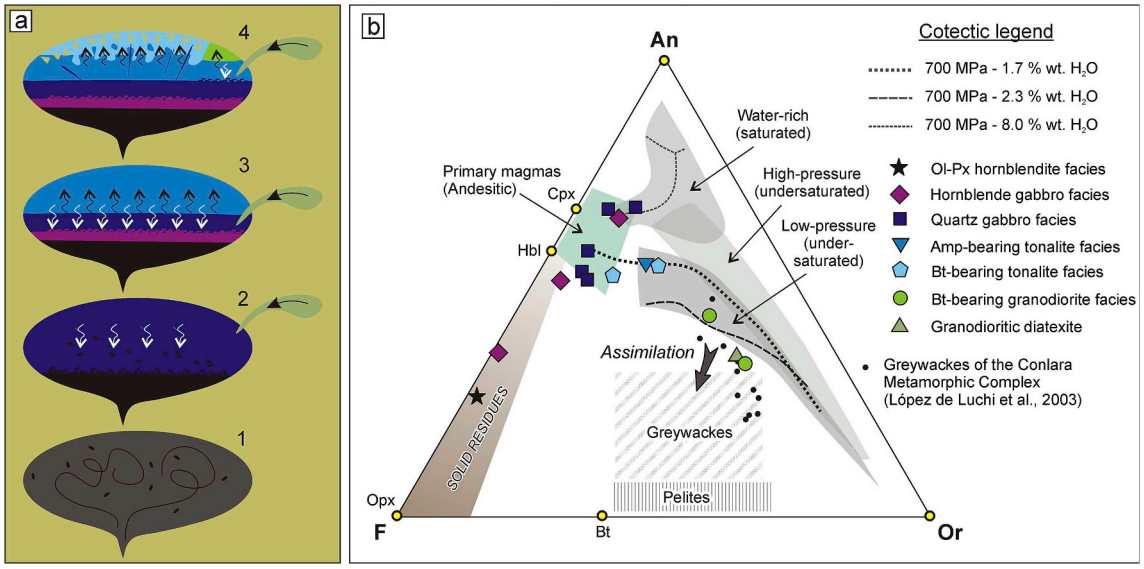

Fig. 15. a) Scheme of differentiation for the LCPC. A primary magma (1) was fractionated early to originate cumulates of Ol-Px hornblendite and produce a liquid equivalent to the quartz gabbro facies (2). Later, the development of layers of accumulated hornblende gabbros from this liquid, which in turn has be contaminated with cortical sources (diatexites), favored the generation of a residual liquid equivalent to the Amp-bearing tonalite facies (3), although part of it crystallized without being fractionated as quartz gabbros. Finally, through batch crystallization of the differentiation of Bt-bearing tonalites was produced from the immediate previous liquid (4), although part of it crystallized as Amp-bearing tonalites, or it produced a Bt-bearing granodiorites through AFC. During this last process, a remobilization of the previously fractionated magmatic mushes and the incorporation of xenoliths from the host rock would have happened. b) The F–An–Or (F = FeO + MgO + MnO; An = anorthite; Or = orthoclase) diagram synthesizing the most relevant cotectic relations fields of diorite–granite systems (after Castro, 2013). Assimilation vector are indicated in relation with metasedimentary (greywackes and pelites) sources.

Hbl and Pl, and incorporating a high proportion of metasammites (through AFC), although the behavior of some elements cannot be justified, for example, Ba, Zr, Cs and LREE. Therefore, we consider the possibility of a purely cortical source (mainly fusion of metagraywacke) for the origin of the granodiorites of the sector.

If the rocks of the area are plotted on the F-An-Or diagram, along with experimental cotectic lines (Castro, 2013), it can be proved that the Bt-bearing granodiorites facies clearly do not come from the extreme differentiation of the intermediate facies in a closed system by CF, since they diverge from the cotectic lines (Fig. 15b).

The interaction between magmas within the LCPC is not only reflected in the chemical composition of the rocks, but it is also the result of a prolonged mechanical exchange between different magmas as evidenced by complex textures in the mineral frameworks of the different facies (mixing), as well as in field evidence like mingling relationships. Some relevant observations that evidence hybridism are zoned and partially dissolved (spongy-cellular type) plagioclase and hornblende partially replaced by biotite (see Streck, 2008; Hibbard, 1995; Castro, 2001).

Geochemical modeling can quantify processes that are observed both at the field scale, for example mingling between facies, and microscopic scale, as imbalance textures in plagioclase crystals.

In several sectors of the Famatinian arc (see Otamendi et al., 2012; Bellos et al., 2015; Cristofolini et al., 2017, and citations in these), it is

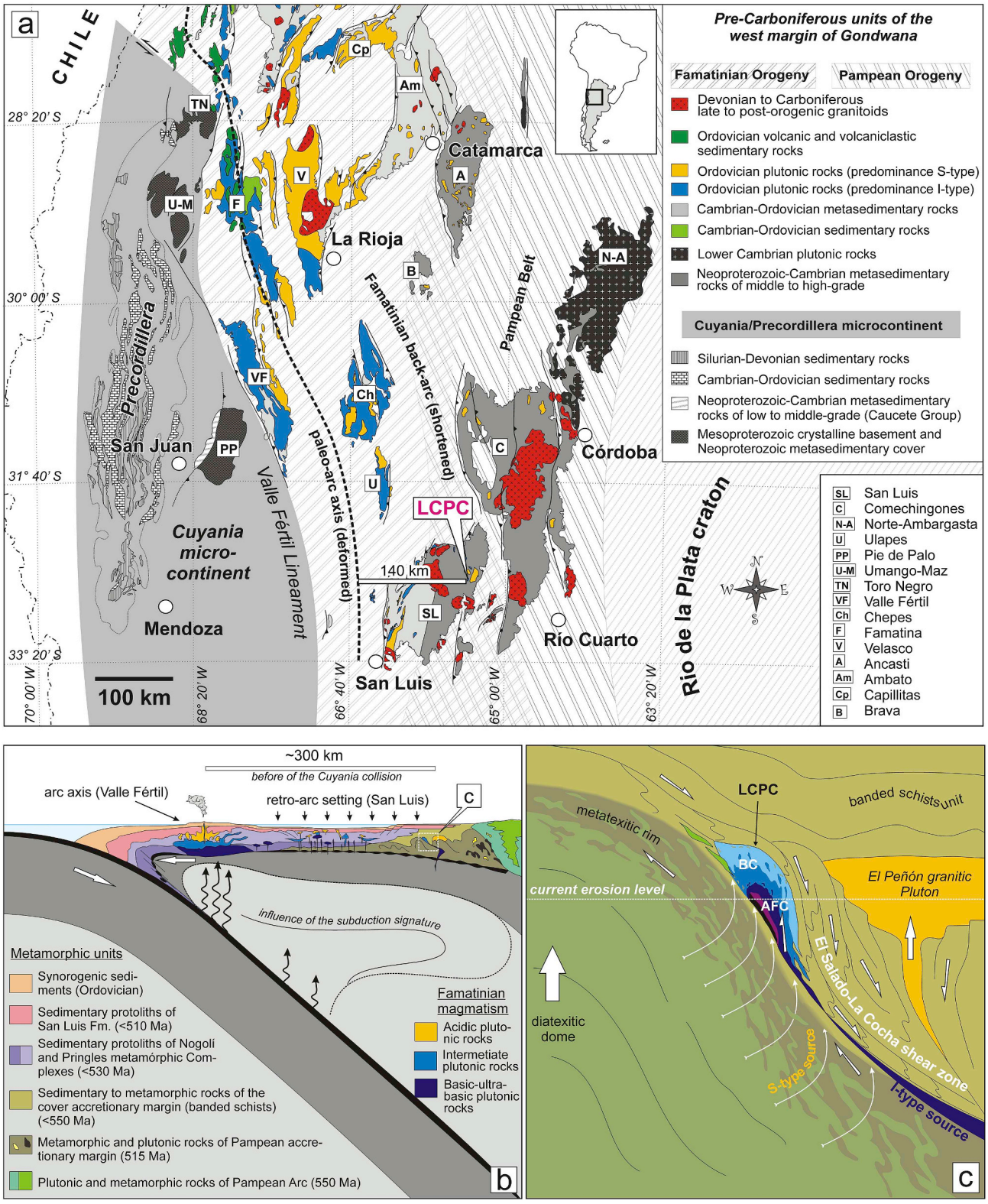

Fig. 16. a) Regional scheme of the Pampean ranges with the location of the different basement blocks. b) Subduction model for the Famatinian orogen at 470 Ma. b) Scheme on the LCPC emplacement and the petrogenetic processes involved. The El Salado-La Cocha shear zone becomes horizontal towards depth (listric normal shear). Therefore, the input of magma must have occurred through this basal detachment that typically separates the more ductile and hot (lower) crust from the colder and brittle (upper) crust.

assumed that the origin of the plutonic siliceous units (mainly granodiorites) is linked to processes of mixing and crustal assimilation in magmas, since their chemistry indicates a possible link with contamination processes of metamorphic host rocks. In the study area, our results do not escape to these interpretations, although we can not rule out the possibility of an origin associated only with crustal melting (S-type magma) for the Bt-bearing granodiorites, since they are geochemically equal to the diatexite rocks. The evolution of the LCPC rocks

indicates that probably many of the mafic-ultramafic rocks present in the Sierra de San Luis that exhibit cumular textures and high Mg#, studied as komatiites or oceanic crust rocks (eg: back-arc ophiolites), correspond to rocks fractionated early from primitive magmas of the Famatinian orogen. These were emplaced in a thick metasedimentary sequence of a marginal basin, similarly to cumulates from the Famatinian arc of the Sierra de Valle Fértil (Otamendi et al., 2009, 2010).

5.4. Geochronological significance

The crystallization age obtained in this work (470 ± 8 Ma) for the Amp-bearing tonalite facies is considered a representative age of the La Cañas plutonic complex. This age is similar to the Ordovician ages (mean of 475 ± 13 Ma) obtained by other authors in the tonalitic and granitic bodies present in the western of Sierra de San Luis (Sims et al., 1998; von Gosen et al., 2002; Steenken et al., 2006; Morosini et al., 2017). It overlaps with the range of 485–465 Ma determined in the Sierra de Valle Fértil - La Huerta (Ducea et al., 2010). However, it also coincides with an age of 474 Ma for granitic pegmatites and leucogranites of the Guacha Corral shear zone, in Sierras de Comechingones (Demartis et al., 2017). It indicates cortical anatexis related to the Famatinian cycle in very distal sites of the arc axis, implying an anomalous geothermal gradient for this orogeny at this position during the Ordovician time.

The ages of 482 to 470 Ma (U/Pb-monazite) published by Whitmeyer and Simpson (2004) for the metamorphic rocks of CMC suggest a synkinematic emplacement (470 Ma) for the LCPC respect to the metamorphic climax of the Famatinian orogeny. U–Pb zircon crystallization ages of magmatic rocks from Sierra de Valle Fértil show that this section of the arc was built over a short time interval during the Ordovician, between 485 and 465 Ma (Ducea et al., 2010). These authors demonstrated that metamorphism was synchronous with magmatic emplacement, and that inherited ages in some of the plutonic rocks as well as detrital zircons in the metasedimentary framework (clusters of ages at around 1090, 600, and 530 Ma) are typical and characteristic of three tectono-magmatic orogenic systems that were active from the Mesoproterozoic to the Early Cambrian in western Gondwana (e.g. Collo et al., 2009). This suggests that the Famatinian arc was emplaced into a Cambrian thick sequence to the thinned margin of the proto-South American continent in the Ordovician. Our results reaffirm these interpretations that are extended to the area of study, considering that inheritance ages in the dated sample (LC-90) fit previous results. Attending to the regional geological context which suggests that the Famatinian orogen didn't bear a conventional continental arc (Cristofolini et al., 2012), evidenced by the development of subaqueous volcanic systems in some places (eg: Cisterna and Coira, 2014; Armas et al., 2018), an island arc could most likely explain petrological and physical characteristics, at least in Argentina between 22° and 34° S. Therefore, this island arc and retro-arc system would have developed over an extensive marginal (ensialic) basin, deposited previously to the beginning of the Famatinian subduction, whose deeper marine deposits would have been sedimented between 550 and 510 Ma before and during the construction of the Pampean orogen. Therefore, an important section of this marginal basin filling, where the studied rocks are placed, was structured and metamorphosed previously to the Famatinian magmatism, contrarily to the arc axis, where Famatinian magmatism and metamorphism were simultaneous to sedimentation.

5.5. Geodynamic implications

The calculated temperature of 690 °C in the Bt-bearing granodiorite facies is barely higher than the temperature of 680 ± 37 °C calculated in the schists located very close to the contact with the migmatite unit and the Las Cañas Pluton. This implies that there are similarities between the obtained results and it is possible to affirm that there was no significant thermal contrast between the magmatic pulses and the hosting setting. That is, the host rock was already hot at the time of the intrusion of the LCPC, and for this reason no thermal haloes are observed. These observations allow us to infer that the intrusion would have been developed at a time close to the climax of the regional metamorphic event unless a high geothermal gradient has remained for a protracted period.

If a pressure of ~445 ± 110 MPa calculated in two samples of the Amp-bearing tonalite facies is taken into account, and interpreted as the crystallization depth of ~17 km, the emplacement must have been produced when the host rock, located immediately on the western edge of the plutons, was partially exhumed from its peak pressure, calculated at 550 ± 120 MPa, ie. ~4 km deeper than the depth at which the complex was emplaced. Although the calculated paleo-depths are statistically identical within the uncertainty, this interpretation is consistent with field relationships that indicate the presence of structured schist xenoliths (with the development of metamorphic surfaces) within the rocks of the plutonic complex. Also, they indicate that the emplacement could be synchronous with the shear bands, since they affect the igneous rocks, mainly at their edges. In this sense, the collected structural evidence suggests that the boundary between rocks of low (schist) and high metamorphic grade (migmatites) is produced through a ductile shear zone, which is propitious (e.g., Hutton, 1996) for a magma ascending from the deepest zone of the crust. The movement indicators in the El Salado-La Cocha shear zone show that the migmatitic unit corresponds to the footwall, while the schists unit makes up the hanging wall, under normal kinematics, consistent with an extension during the intrusion (Fig. 1b).

The HT/LP conditions (~32.3 °C/km) determined for the host rocks of the LCPC, are usually associated with orogens dominated by heat conduction due to the high permeation of magma in the surroundings, or highly radiogenic areas typical of extensional crust (Goscombe et al., 2005). This is evidenced by the significant amount of diatexitic rocks in the western sector of the area, which reflects an advanced degree of anatexis over the sedimentary (meta) protoliths.

The geochronological and geochemical correlation between the plutonic rocks of the LCPC and the western sector of Sierra de San Luis (Sims et al., 1998; Brogioni et al., 2005; Steenken et al., 2006; López de Luchi et al., 2007), together with those of Sierra de Valle Fértil and Velasco (Otamendi et al., 2009, 2017; Ducea et al., 2015), indicates that the Famatinian magmatism was synchronous during a short period of approximately 15 My (480-465 Ma). Additionally, and not less important, the Famatinian magmatism was extremely extended across the orogen and perpendicularly to the inferred paleo-trench. One argument that could explain this observation is to consider the development of an extensional retro-arc setting where the Ordovician plutons were emplaced, currently cropping out in the Sierras of San Luis and Córdoba, as well as in the Sierras de Ancasti and Ambato (east of the Famatinian Central Batholith; Otamendi et al., 2017), and even reaching the NW Argentina, in the Sierras de Cachi (Hongn et al., 2014). However, our results (geochemical signature of studied rocks) suggest a strong subduction signature in the I-type components of the sources.

The presence of this magmatism in all the Eastern Sierras Pampeanas (calc-alkaline plutonic rocks) suggests that the geodynamic context occurred in the western edge of Gondwana during the Ordovician period (490-465 Ma) was generalized (Pankhurst et al., 1998; Sato et al., 2003; Morosini et al., 2009, 2017; Otamendi et al., 2009; Steenken et al., 2010; Cristofolini et al., 2017). This magmatism at a regional scale is framed within the context of the Famatinian orogeny, whose maximum lithological expression (plutonic-volcanic rocks) is currently exposed in the Sierras of Valle Fértil-La Huerta, Ulapes-Chepes and Famatina (Fig. 16a, Otamendi et al., 2017), although it is widely seen throughout northern and central Argentina, from the Puna in Jujuy province to La Pampa province (see Pankhurst et al., 1998; Coira et al., 2009; Chernicoff et al., 2010; Ducea et al., 2010; Grosse et al., 2011; Otamendi et al., 2012; Cristofolini et al., 2012, 2017). Based on the aforementioned geological context and given

the existence of plutonic rocks related to a calc-alkaline magmatism exposed in the northeast of the CMC, the studied area is considered part of the Famatinian orogen, although in a setting far away from the arc axis (Fig. 16b).

In order to provide a satisfactory explanation of how arc geochemical features can be recognized at distal positions from the orogenic axis (~300 km in the paleo-reconstruction), and therefore how an asthenospheric melting wedge could have influenced the extensive retro-arc, we invoke the ridge-trench collision model of Schwartz et al. (2008). This model implies the subduction of a mid-ocean ridge as the cause of the Pampean orogeny, where synorogenic sediments (Cambrian) were deposited along an extensive marine basin above an oceanic lithosphere (Cristofolini et al., 2012), which acted as a passive margin during a protracted period of time (~25 Myr), until the restitution of the Famatinian subduction around 490 Ma. Then a uniform heat flow in the asthenospheric mantle (extended from the arc front to the continent), associated with different dehydration fronts of the oceanic slab during the Famatinian subduction, would have been the cause of magma emplacement (I-type) into a thin crust with a sedimentary cover at a long distance from the arc axis (Fig. 16b).

Differences between tonalites of the LCPC and the western sector of the Sierra de San Luis and Valle Fertil-La Huerta are related to the progressive increase in ΣREE from the arc axis to the studied area. We interpret that these are related to smaller volumes of mantle melt in the retro-arc zone, since dehydration of the deeper subducted oceanic slab was lower than in the arc axis, where the first dehydration front occurred.

6. Conclusions

The whole rock geochemistry allows us to conclude that the rocks of the Las Cañas plutonic complex correspond to arc magmas, since a strong component of subduction is evidenced in their signatures of major and trace elements. These characteristics show that the rocks are calcalkaline of medium-potassium, metaluminous and magnesian. The enrichment in some incompatible elements (Rb, Th, U, K) and negative anomalies in Nb respect to Th and Ce are interpreted as typical of subduction related arc rocks. The Pb enrichment in the basic and intermediate rocks of LCPC suggests a possible Pb input from subduction-derived fluids. However, the results of the treatment of geochemical data and the field evidences, such as the presence of zircons with inherited cores inside the rocks of the LCPC, indicate that there was a clear early cortical contamination. Assimilation and fractional crystallization processes (AFC) occurred in the initial stages of magmatic evolution in order to model the composition of the rocks. Then, in the later stages batch crystallization (BC) is a more likely process than AFC.

The relatively flat chondrite-normalized REE patterns, the low Sr/Y and $(Gd/Yb)_{C-N}$, in basic and intermediate rocks, indicate a relatively shallow fractionalization without garnet in the residue, which is in line with a pre-collisional arc stage linked to an extensive retro-arc setting.

The crystallization age obtained in the Amp-bearing tonalite facies is 470.4 ± 8.1 Ma, typically Famatinian. The inheritances of a metasedimentary source by assimilation or partial melting of the Conlara Metamorphic Complex is evidenced in ages of zircon cores from Cambrian (531 Ma, Pampean), Late Neoproterozoic (657 Ma, Brazilians) and Early Neoproterozoic (869–907 Ma, Late Grenvillian?). These protoliths can be equivalent to the Puncoviscana Formation of the NW Argentina, or to even younger units (Middle Cambrian), such as the Negro Peinado and Achavil formations of the Sierra de Famatina and Mesón Group in the Eastern Cordillera and Puna.

Besides, this study reveals that the basic and intermediate magmas had a significant amount of (meta) sedimentary components, based on a mass balance approach. The incorporation of inherited zircons must have resulted from massive partial to nearly complete melting of graweckes host rocks and subsequent assimilation into the evolving magmas.

Acknowledgments

We are grateful to the Consejo Nacional de Investigaciones Científicas y Técnicas (CONICET), the projects PROICO 03–1818 (UNSL), PROIPRO 03–1718 (UNSL), PICT-2014-0958 (UNRC), and ASEGEO (Asociación de Estudiantes de Geología - UNSL) to support this work. The authors thank for technical and human support, especially to Jose Gil Ibarguchi, provided by SGIker of UPV/EHU and European funding (ERDF and ESF). We are also grateful for the thorough review of the manuscript by Joshua J. Schwartz and Fernando Hongn, the Regional-Editor Victor Ramos and Editor-in-Chief Andrés Folguera. Finally, this paper is dedicated to the memory of Dr. Eduardo Llambías, who was one of the pioneers in the understanding of plutonic magmatism in the Sierra de San Luis.

Appendix A. supplementary data

Table A.1
Modal analysis of studied plutonic rocks.

Facies	Sample	primary minerals										secondary minerals						modal proportion		
		Ol (%)	Cpx (%)	Amp (%)	Bt (%)	Pl (%)	Kfs (%)	Qz (%)	Ttn (%)	Ap (%)	Zrn (%)	Ms (%)	Ep (%)	Chl (%)	Tlc (%)	Srp (%)	Opq (%)	Q (%)	A (%)	P (%)
Bt-bearing granodiorite	LC-176	–	–	–	20.4	42.9	8.6	25.1	–	–	0.2	1.9	–	–	–	–	0.9	32.7	11.2	56.1
	BLC-3	–	–	–	10.2	38.9	6.7	37.1	0.3	0.5	–	5.6	0.6	–	–	–	–	43.3	9.6	47.1
	LC-84	–	–	–	16.3	39.9	10.7	29.8	–	0.3	–	1.8	1.2	–	–	–	–	36.6	13.0	50.4
Bt-bearing tonalite	670	–	–	–	28.1	44.6	–	21.7	–	–	–	–	3.8	1.1	–	–	0.7	35.2	–	64.9
	N4	–	–	–	22.0	56.5	–	16.0	–	–	–	0.5	3.5	–	–	–	1.5	36.8	–	63.2
	685	–	–	–	19.0	49.9	–	29.1	–	–	–	0.8	0.7	0.5	–	–	–	31.0	–	69.0
	LC-178	–	–	–	21.7	45.1	–	19.7	–	–	–	1.7	5.5	1.8	–	–	4.5	30.4	–	69.6
	LC-S3	–	–	–	15.6	27.7	–	18.6	–	–	0.3	3.5	13.4	14.6	–	–	6.3	29.5	–	70.5
	LC-177	–	–	–	39.1	32.0	–	14.8	–	1.2	–	0.6	11.8	–	–	–	0.6	25.0	–	75.0
	E3b	–	–	–	14.3	35.7	–	14.9	0.6	1.0	0.3	1.0	12.3	13.3	–	–	6.5	23.4	–	76.6
	E2	–	–	–	17.1	43.1	–	18.7	–	0.2	0.1	1.6	5.7	8.9	–	–	4.5	28.0	–	72.0

Amp-bearing tonalite	20608	–	–	80.8	–	8.9	–	4.2	0.3	–	–	0.8	4.2	1.0	–	–	–	23.8	–	76.2
	LC-1a	–	–	2.4	11.4	53.3	–	18.3	–	–	–	5.7	5.5	1.8	–	–	1.6	21.1	–	78.9
	LC-90	–	–	6.8	15.2	49.4	–	15.5	–	–	0.1	2.5	5.7	4.2	–	–	0.7	23.7	–	76.3
	LC-180	–	–	62.0	–	23.8	–	6.6	–	–	–	1.8	3.1	2.7	–	–	–	21.7	–	78.3
	669	–	–	46.9	–	34.0	–	9.2	–	–	–	2.8	5.6	1.5	–	–	–	21.4	–	78.6
	60608	–	–	41.2	9.5	31.0	–	13.6	0.2	0.2	–	0.9	0.9	2.0	–	–	0.5	29.9	–	70.1
	N2b	–	–	27.4	5.4	43.3	–	13.5	0.7	–	–	–	2.6	1.1	–	–	6.1	22.7	–	77.3
	671	–	–	18.7	18.9	39.8	–	18.1	–	–	–	–	2.2	0.8	–	–	1.5	30.1	–	69.9
	LC-1b	–	–	9.9	7.5	48.5	–	19.4	–	–	–	4.0	4.1	5.1	–	–	1.5	26.9	–	73.1
Qtz-gabbro	LC-7	–	–	19.8	–	50.4	–	10.5	–	0.2	–	1.0	2.7	13.0	–	–	2.5	17.5	–	82.5
	BLC-1A	–	–	44.7	0.8	34.1	–	5.9	–	–	–	7.4	1.9	2.1	–	–	3.0	12.0	–	88.0
	BLC-1B	–	–	28.0	3.5	51.8	–	7.0	–	–	–	1.6	4.8	0.5	–	–	2.8	11.9	–	88.1
	LC-9	–	–	31.0	–	42.8	–	7.5	–	–	–	5.7	4.5	6.8	–	–	1.8	14.9	–	85.1
	668	–	–	15.1	22.2	50.7	–	5.8	–	–	–	–	1.6	–	–	–	4.7	10.0	–	90.0
	680	–	–	25.9	13.2	38.0	–	10.3	–	–	–	0.3	8.6	3.4	–	–	0.3	18.1	–	81.9
	LC-35	–	–	12.0	1.0	37.5	–	7.6	–	0.4	–	16.6	10.8	13.0	–	–	1.0	10.5	–	89.5
	N2a	–	–	23.6	5.6	21.9	–	4.9	–	–	–	5.8	21.2	11.9	–	–	5.1	18.2	–	81.8
	W1	–	–	40.4	–	29.0	–	5.7	–	–	–	3.0	8.1	13.2	–	–	0.6	12.4	–	87.6
	E5	–	–	41.0	–	19.5	–	4.7	–	–	–	7.6	9.0	18.0	–	–	0.3	11.4	–	88.6

Facies	Sample	primary minerals										secondary minerals						modal proportion		
		Ol (%)	Cpx (%)	Amp (%)	Bt (%)	Pl (%)	Kfs (%)	Qz (%)	Ttn (%)	Ap (%)	Zrn (%)	Ms (%)	Ep (%)	Chl (%)	Tlc (%)	Srp (%)	Opq (%)	Pl (%)	Px (%)	Hbl (%)
Hbl-gabbro																				
	010608	–	–	28.2	2.3	6.3	–	1.0	0.8	–	–	–	54.4	3.4	–	–	3.64	18.3	–	81.7
	100501	–	–	40.0	–	42.5	–	–	–	–	–	4.3	9.0	3.6	–	–	0.7	51.5	–	48.5
Ol-Px hornblendite																		Ol (%)	Px (%)	Hbl (%)
	E1	–	10.0	33.8	–	–	–	–	–	–	–	–	–	–	13.3	36.2	7.2	38.8	24.7	36.5
	S1	1.1	11.0	48.8	–	–	–	–	–	–	–	–	–	–	5.5	31.0	2.6	36.6	13.7	49.7
	N1	17.2	10.4	52.9	–	–	–	–	–	–	–	–	–	–	–	15.2	2.2	33.8	10.9	55.3
	667	15.7	6.2	27.4	–	–	–	–	–	–	–	–	–	21.7	–	25.6	3.5	34.2	11.8	54.1
	90501	0.7	22.1	42.9	–	–	–	–	–	–	–	–	–	–	4.6	25.4	4.3	28.7	26.5	44.8

Table A.2
Mineral analyses for Las Cañas plutonic complex

facies	sample	mineral- point (position)	SiO_2	TiO_2	Al_2O_3	FeO	Cr_2O_3	MnO	MgO	CaO	Na_2O	K_2O	NiO	BaO	F	Cl	Total
Ol-Px hornblendite	N1	Ol-1 (r)	38.95	0.02	0.02	16.84	0.04	0.28	44.43	0.03	0.03		0.16				100.63
Ol-Px hornblendite	N1	Ol-2 (c)	38.36	0.01		17.64	0.02	0.30	44.00	0.06	0.02		0.24				100.59
Ol-Px hornblendite	N1	Ol-3 (c)	36.18	0.03	0.01	17.51	0.02	0.29	43.73	0.03	0.01		0.20				97.96
Ol-Px hornblendite	N1	Ol-4 (c)	36.15	0.03		17.72	0.01	0.26	43.59	0.02	0.02		0.16				97.96
Ol-Px hornblendite	N1	Ol-5 (c)	36.51	0.01	0.03	17.28	0.00	0.29	43.67	0.03	0.03		0.17				98.03
Ol-Px hornblendite	N1	Ol-6 (c)	37.02	0.01	0.02	17.23	0.01	0.25	44.19	0.03			0.13				98.82
Ol-Px hornblendite	N1	Ol-7 (c)	37.31	0.01	0.01	17.20	0.05	0.26	44.51		0.02		0.18				99.52
Ol-Px hornblendite	N1	Ol-8 (c)	36.93	0.01	0.02	17.20	0.01	0.34	44.30		0.01		0.17				98.97
Ol-Px hornblendite	N1	Ol-9 (r)	37.69	0.01		17.05	0.02	0.31	44.87	0.04	0.02		0.14				100.08
Ol-Px hornblendite	N1	Amp-1 (a)	43.65	0.66	14.23	7.18		0.11	16.03	12.63	1.62	0.65			0.03	0.07	96.87
Ol-Px hornblendite	N1	Amp-2 (a)	44.51	0.64	12.60	7.22		0.10	16.05	12.72	1.53	0.38			0.03	0.06	95.83
Ol-Px hornblendite	N1	Amp-3 (a)	44.55	0.24	13.26	6.53		0.10	17.10	12.66	1.63	0.11			0.03	0.05	96.26
Ol-Px hornblendite	N1	Mag-1 (a)				95.52											95.52
Ol-Px hornblendite	E1	Px-1 (a)	48.53	0.11	2.66	4.05	0.27	0.15	16.33	23.69	0.14		0.02				95.90
Ol-Px hornblendite	E1	Px-2 (a)	47.95	0.21	3.76	3.87	0.55	0.16	16.12	23.69	0.15		0.05				96.51
Ol-Px hornblendite	E1	Px-3 (a)	48.72	0.09	2.56	3.81	0.16	0.16	16.26	24.21	0.10		0.03				96.10
Ol-Px hornblendite	E1	Px-4 (a)	48.22	0.22	4.55	3.78		0.12	16.48	26.63							100.25
Ol-Px hornblendite	E1	Mag-1 (a)	0.49	0.45		94.64											95.59
Ol-Px hornblendite	E1	Mag-2 (a)	0.34			94.92											95.26
Ol-Px hornblendite	E1	Srp-1 (a)	41.26		4.16	7.69			39.08								92.18
Ol-Px hornblendite	E1	Spl-1 (a)	2.93	2.40	15.2	59.37	15.24		2.98	1.61							99.74
Hbl-gabbro	100501	Amp-1 (a)	43.16	1.12	13.59	12.66		0.13	12.45	11.47	1.75	0.23			0.05	0.08	96.69
Hbl-gabbro	100501	Amp-2 (a)	43.22	1.38	13.97	12.68		0.19	12.26	11.52	1.75	0.32			0.15	0.02	97.47
Hbl-gabbro	100501	Pl-1 (d-c)	55.79		28.21	0.01				10.04	5.77	0.07					99.9
Hbl-gabbro	100501	Pl-2 (d-c)	53.87		29.63					11.43	4.95	0.05					99.9
Hbl-gabbro	100501	Pl-3 (d-c)	52.47		30.79	0.10				12.75	4.46	0.03					100.6
Hbl-gabbro	100501	Pl-4 (c)	45.35		35.69	0.02				18.24	0.98						100.3
Hbl-gabbro	100501	Pl-5 (c)	45.55		35.71	0.08				18.31	1.16						100.8
Hbl-gabbro	100501	Pl-6 (m)	54.60		28.77	0.10				10.88	5.39	0.04					99.8
Hbl-gabbro	100501	Pl-7 (m)	54.70		29.47	0.06				11.11	5.34	0.07					100.7
Hbl-gabbro	100501	Pl-8 (d-c)	52.98		30.89	0.08				12.87	4.18	0.06					101.1
Hbl-gabbro	100501	Pl-9 (d-c)	52.19		30.41	0.11				12.86	4.31	0.04					99.9

Qz-gabbro	N2a	Amp-1 (a)	44.69	0.62	13.04	15.10	0.42	11.67	11.26	1.37	0.23		0.15	0.04	98.58
Qz-gabbro	N2a	Amp-2 (a)	43.47	0.41	14.01	15.23	0.44	11.15	11.30	1.69	0.29		0.16	0.05	98.20
Qz-gabbro	N2a	Pl-1 (d-c)	54.05		30.31	0.06			12.47	4.63	0.05				101.6
Qz-gabbro	N2a	Pl-2 (c)	46.41		35.21	0.03			18.26	1.53	0.02				101.4
Qz-gabbro	N2a	Pl-3 (m)	54.84		28.83	0.01			11.13	5.50	0.04				100.3
Qz-gabbro	N2a	Pl-4 (m)	54.84		29.63	0.11			11.07	5.11	0.04				100.8
Qz-gabbro	N2a	Pl-5 (m)	52.33		31.79	0.24			13.50	3.96					101.8
Qz-gabbro	N2a	Mag-1 (a)				96.81									96.81
Qz-gabbro	W1	Amp-1 (a)	45.11	0.67	12.10	11.52	0.21	14.24	11.43	1.45	0.12		0.05	0.01	96.90
Qz-gabbro	W1	Amp-2 (a)	46.39	0.44	10.96	10.75	0.20	14.49	12.09	1.14	0.17		0.16	0.00	96.78
Qz-gabbro	W1	Amp-3 (a)	49.70	0.19	7.30	13.55	0.61	17.00	7.47	0.91	0.07		0.03	0.03	96.87

Position: (c) core, (m) mantle, (r) rim, (d-c) dissolved core, (d-m) dissolved mantle, (a) aleatory

facies	sample	mineral-point (position)	SiO_2	TiO_2	Al_2O_3	FeO	Cr_2O_3	MnO	MgO	CaO	Na_2O	K_2O	NiO	BaO	F	Cl	Total
Qz-gabbro	W1	Pl-2 (m)	54.39		30.56	0.03				12.14	4.80	0.05					102.0
Qz-gabbro	W1	Pl-3 (d-m)	62.48		24.87	0.06				5.55	8.43	0.12					101.5
Qz-gabbro	W1	Pl-5 (d-c)	53.63		30.74	0.02				12.45	4.77	0.05					101.7
Qz-gabbro	W1	Pl-6 (d-c)	57.63		27.92	0.01				8.07	6.25	0.07					99.9
Qz-gabbro	W1	Pl-7 (d-c)	55.98		28.68	0.01				10.13	5.80	0.06					100.7
Qz-gabbro	W1	Pl-8 (d-c)	54.18		30.56	0.02				12.04	4.82	0.02					101.6
Qz-gabbro	W1	Pl-9 (d-c)	56.41		29.08	0.02				10.53	5.61	0.03					101.7
Qz-gabbro	W1	Pl-10 (m)	53.72		29.55	0.12				12.15	5.05	0.04					100.6
Qz-gabbro	W1	Pl-11 (m)	58.54		26.90	0.05				8.36	6.88	0.09					100.8
Qz-gabbro	W1	Pl-12 (m)	53.58		29.90	0.08				11.97	4.63	0.09					100.2
Qz-gabbro	W1	Pl-13 (d-c)	59.70		26.20	0.09				7.01	7.31	0.09					100.4
Qz-gabbro	W1	Pl-14 (d-m)	64.09		22.84	0.07				3.59	9.27	0.03					99.9
Qz-gabbro	LC-35	Amp-1 (a)	51.34	0.16	4.31	19.43		0.71	17.82	2.90	0.57	0.03			0.10	0.01	97.39
Qz-gabbro	LC-35	Pl-1 (c)	47.84		33.80	0.02				16.72	2.17	0.06					100.6
Qz-gabbro	LC-35	Pl-2 (c)	48.37		34.14	0.01				16.54	2.19	0.05					101.3
Qz-gabbro	LC-35	Pl-3 (c)	50.32		32.21	0.09				15.06	3.23	0.06					101.0
Qz-gabbro	LC-35	Pl-4 (m)	54.78		29.67	0.02				11.44	5.10	0.04					101.1
Qz-gabbro	LC-35	Pl-5 (m)	53.22		28.15	0.06				10.50	5.23	0.05					97.2
Amp tonalite	20608	Amp-1 (c)	44.42	0.91	12.27	11.99		0.22	13.38	11.60	1.15	0.38			0.02	0.02	96.35
Amp tonalite	20608	Amp-2 (m)	46.72	0.42	9.40	10.99		0.32	15.11	11.45	0.97	0.21			0.03	0.03	95.65
Amp tonalite	20608	Amp-3 (r)	45.41	0.47	10.82	11.88		0.29	13.90	11.62	1.40	0.17			0.13	0.01	96.10
Amp tonalite	20608	Amp-4 (r)	50.76	0.13	3.59	9.48		0.22	17.53	12.79	0.30	0.06			0.10	0.01	94.98
Amp tonalite	20608	Amp-5 (c)	46.88	0.50	9.70	10.91		0.23	15.07	11.65	1.01	0.18			0.15	0.03	96.32
Amp tonalite	20608	Amp-6 (m)	42.90	1.07	12.54	11.78		0.22	13.60	11.64	1.51	0.41			0.01	0.03	95.72
Amp tonalite	20608	Amp-7 (r)	46.14	0.48	10.40	11.75		0.26	13.97	11.70	1.36	0.18			0.05	0.02	96.32
Amp tonalite	20608	Bt-1 (a)	36.41	1.35	16.70	16.60		0.18	13.36	0.07	0.11	9.10		0.15	0.22	0.09	94.32
Amp tonalite	20608	Bt-2 (a)	36.54	1.70	16.94	16.80		0.19	13.31	0.04	0.14	9.28		0.20	0.13	0.10	95.38
Amp tonalite	20608	Bt-3 (a)	38.08	1.39	17.11	16.32		0.21	13.63	0.02	0.12	9.68		0.22	0.09	0.05	96.91
Amp tonalite	20608	Bt-4 (a)	36.71	1.33	17.27	16.71		0.21	13.58	0.03	0.08	9.52		0.23	0.19	0.07	95.91
Amp tonalite	20608	Pl-2 (a)	56.60		28.51	0.02				9.94	5.82	0.04					100.9
Amp tonalite	60608	Amp-1 (r)	42.69	0.77	13.77	15.17		0.72	11.33	10.88	1.57	0.25			0.07	0.05	97.27
Amp tonalite	60608	Amp-2 (r)	42.93	0.55	13.21	15.06		0.64	11.60	10.92	1.60	0.23			0.07	0.02	96.81
Amp tonalite	60608	Amp-3 (c)	42.30	0.83	12.75	15.23		0.74	11.59	10.14	1.72	0.21			0.03	0.04	95.59
Amp tonalite	60608	Pl-1 (d-c)	55.45		29.21	0.03				10.76	5.53	0.07					101.1
Amp tonalite	60608	Pl-2 (c)	50.05		32.43	0.04				15.04	3.16	0.02					100.7
Amp tonalite	60608	Pl-3 (d-c)	57.99		27.79	0.02				9.08	6.53	0.03					101.4
Amp tonalite	60608	Pl-4 (c)	51.64		31.98	0.06				14.01	3.76	0.02					101.5
Amp tonalite	60608	Pl-5 (m)	56.30		29.08	0.10				10.06	5.81	0.06					101.4
Amp tonalite	60608	Pl-2 (m)	55.96		28.80	0.09				10.47	5.80	0.01					101.1
Amp tonalite	60608	Pl-3 (m)	56.75		28.66					9.94	5.87	0.04					101.3
Amp tonalite	60608	Pl-4 (c)	51.26		32.28	0.04				14.21	3.41	0.03					101.2
Amp tonalite	60608	Pl-5 (d-c)	57.21		28.16					9.74	6.03	0.04					101.2
Amp tonalite	60608	Pl-6 (c)	51.65		32.28					14.17	3.60	0.04					101.7

Position: (c) core, (m) mantle, (r) rim, (d-c) dissolved core, (d-m) dissolved mantle, (a) aleatory

facies	sample	mineral-point (position)	SiO_2	TiO_2	Al_2O_3	FeO	Cr_2O_3	MnO	MgO	CaO	Na_2O	K_2O	NiO	BaO	F	Cl	Total
Amp tonalite	60608	Mag-1 (a)				93.81											93.81
Amp tonalite	60608	Ilm-1 (a)	0.43	49.5	0.40	44.12		5.16	0.46	0.36							100.4
Amp tonalite	60608	Ttn-1 (a)	30.21	37.2	2.06	0.55				35.11							105.1
Amp tonalite	LC-90	Bt-1 (a)	37.47	1.91	17.18	17.03		0.17	12.78	0.00	0.17	9.34		0.17	0.16	0.04	96.43
Amp tonalite	LC-90	Bt-2 (a)	37.03	2.05	17.25	16.86		0.20	12.73	0.01	0.16	9.33		0.16	0.25	0.03	96.07
Amp tonalite	LC-90	Pl-1 (c)	51.35		32.16	0.12				14.41	3.49	0.06					101.6
Amp tonalite	LC-90	Pl-2 (m)	54.60		30.34	0.05				11.61	4.93	0.05					101.6
Amp tonalite	LC-90	Pl-3 (m)	55.06		29.79	0.08				11.11	5.25	0.07					101.4
Amp tonalite	LC-90	Pl-4 (m)	53.51		30.73	0.09				12.12	4.78	0.04					101.3
Amp tonalite	LC-90	Pl-5 (m)	57.26		28.29	0.11				9.52	6.18	0.06					101.4
Amp tonalite	LC-90	Pl-6 (r)	64.84		23.74	0.21				4.03	9.82	0.06					102.7
Bt tonalite	LC-S3	Bt-1 (a)	36.84	1.51	16.79	16.73		0.20	12.63	0.11	0.12	8.98		0.19	0.13	0.10	94.31
Bt tonalite	LC-S3	Bt-2 (a)	36.01	1.68	16.54	17.62		0.18	12.39	0.17	0.10	8.57		0.21	0.16	0.10	93.72
Bt tonalite	LC-S3	Pl-1 (c)	54.18		29.57	0.04				11.17	5.04	0.04					100.0

Bt tonalite	LC-S3	Pl-2 (c)	54.68		29.65	0.05			11.35	5.10	0.06				100.9
Bt tonalite	LC-S3	Pl-3 (c)	55.18		29.44	0.02			11.14	5.34	0.05				101.2
Bt tonalite	LC-S3	Pl-4 (m)	50.68		31.97	0.06			14.28	3.48	0.04				100.5
Bt tonalite	LC-S3	Pl-5 (r)	55.16		29.24	0.03			11.21	5.46	0.07				101.2
Bt tonalite	LC-178	Bt-1 (a)	36.95	1.74	17.21	17.88	0.24	12.24	0.02	0.12	9.57	0.14	0.04		96.14
Bt tonalite	LC-178	Bt-2 (a)	37.22	1.64	16.66	18.46	0.24	12.27	0.01	0.08	9.38	0.16	0.12	0.01	96.23
Bt tonalite	LC-178	Pl-1 (d-c)	50.77		32.92	0.06			14.55	3.27	0.06				101.6
Bt tonalite	LC-178	Pl-2 (c)	47.59		34.00	0.02			16.55	2.12	0.04				100.3
Bt tonalite	LC-178	Pl-3 (c)	48.90		33.50	0.03			15.63	2.50	0.02				100.6
Bt tonalite	LC-178	Pl-4 (c)	49.05		33.08				15.38	2.85	0.03				100.4
Bt tonalite	LC-178	Pl-5 (c)	48.48		34.59	0.05			16.69	2.07					101.9
Bt tonalite	LC-178	Pl-6 (m)	53.69		30.16	0.07			11.98	4.57	0.04				100.5
Bt tonalite	LC-178	Pl-7 (m)	54.76		30.01	0.05			11.49	5.14	0.05				101.5
Bt tonalite	LC-178	Pl-8 (r)	56.82		28.50	0.10			10.07	6.00	0.05				101.6
Bt tonalite	LC-178	Pl-9 (r)	57.28		27.64	0.11			9.03	6.37	0.06				100.5
Bt tonalite	E3b	Bt-1 (a)	37.15	1.24	17.38	16.55	0.19	12.97	0.09	0.09	8.81	0.17	0.21	0.09	94.932
Bt tonalite	E3b	Bt-2 (a)	37.29	1.75	17.58	16.88	0.19	13.24	0.06	0.12	8.96	0.13	0.29	0.07	96.549
Bt tonalite	E3b	Pl-1 (c)	54.05		29.77	0.02			11.76	4.94	0.08				100.6
Bt tonalite	E3b	Pl-2 (c)	54.88		29.81	0.03			11.42	5.24	0.02				101.4
Bt tonalite	E3b	Pl-3 (m)	49.85		32.76	0.02			15.10	2.80	0.04				100.6
Bt tonalite	E3b	Pl-4 (r)	55.55		28.97	0.02			10.69	5.40	0.03				100.7
Bt granodiorite	LC-176	Bt-1 (a)	35.30	3.23	17.30	21.36	0.48	8.86	0.01	0.11	9.75	0.05	0.20	0.03	96.66
Bt granodiorite	LC-176	Bt-2 (a)	35.54	2.67	17.03	21.11	0.46	8.84	0.03	0.08	9.61	0.18	0.11	0.02	95.67
Bt granodiorite	LC-176	Pl-1 (d-c)	56.88		28.03	0.08			9.83	5.92	0.11				100.8
Bt granodiorite	LC-176	Pl-2 (d-c)	57.72		27.53	0.00			8.81	6.49	0.10				100.7
Bt granodiorite	LC-176	Pl-3 (d-c)	57.98		26.94	0.12			8.58	6.74	0.17				100.5
Bt granodiorite	LC-176	Pl-4 (d-c)	57.97		28.10	0.04			9.09	6.28	0.08				101.6
Bt granodiorite	LC-176	Pl-5 (c)	50.96		32.09	0.01			14.40	3.40	0.05				100.9

Position: (c) core, (m) mantle, (r) rim, (d-c) dissolved core, (d-m) dissolved mantle, (a) aleatory

facies	sample	mineral-point (position)	SiO_2	TiO_2	Al_2O_3	FeO	Cr_2O_3	MnO	MgO	CaO	Na_2O	K_2O	NiO	BaO	F	Cl	Total
Bt granodiorite	LC-176	Pl-6 (d-c)	56.46		28.84	0.10				9.87	5.93	0.09					101.3
Bt granodiorite	LC-176	Pl-7 (c)	53.13		30.43	0.01				12.21	4.46	0.10					100.3
Bt granodiorite	LC-176	Pl-8 (m)	57.81		26.73	0.05				8.43	6.58	0.14					99.7
Bt granodiorite	LC-176	Pl-9 (m)	58.51		26.86	0.03				8.37	6.92	0.13					100.8
Bt granodiorite	LC-176	Pl-10 (m)	59.27		26.49	0.06				7.78	7.06	0.11					100.8
Bt granodiorite	LC-176	Kfs-2 (r)	65.13		18.78						0.66	15.68		0.39			100.62
Bt granodiorite	LC-176	Kfs-3 (r)	64.98		18.86	0.04				0.01	0.79	15.50		0.96			101.14
Bt granodiorite	LC-176	Kfs-4 (c)	65.00		19.17	0.02					0.75	15.48		0.79			101.20
Bt granodiorite	LC-176	Kfs-5 (r)	65.73		19.06	0.01					0.88	15.41		0.92			102.01
Bt granodiorite	LC-84	Ms-1 (a)	45.98	0.33	34.57	3.44		0.04	0.81		0.32	10.65		0.15	0.15	0.01	96.45
Bt granodiorite	LC-84	Ms-2 (a)	46.85	1.03	32.99	3.63		0.02	1.18	0.04	0.34	10.44		0.30	0.03		96.79
Bt granodiorite	LC-84	Bt-1 (a)	36.22	2.71	17.80	20.19		0.45	9.73	0.02	0.06	9.67		0.22	0.17	0.01	97.24
Bt granodiorite	LC-84	Bt-2 (a)	36.62	2.74	17.32	19.66		0.41	9.46	0.03	0.06	9.37		0.07	0.18	0.01	95.93
Bt granodiorite	LC-84	Pl-1 (m)	61.21		25.87	0.08				6.59	7.92	0.18					101.8
Bt granodiorite	LC-84	Pl-2 (m)	61.46		25.36	0.02				6.37	8.07	0.12					101.4
Bt granodiorite	LC-84	Pl-3 (c)	58.02		27.70	0.03				8.75	6.56	0.06					101.1
Bt granodiorite	LC-84	Pl-4 (c)	58.53		27.42	0.04				8.67	6.84	0.09					101.6

Position: (c) core, (m) mantle, (r) rim, (d-c) dissolved core, (d-m) dissolved mantle, (a) aleatory

Table A.3
Results of the GJ-1 and Plešovice zircon standards

Spot name	Data for Wetherill plot					Data for Tera-Wasserburg plot					Dates (Ma)				Elemental concentration (μg g-1) a			% Concb
	$^{207}Pb/^{235}U$	2s (abs)	$^{206}Pb/^{238}U$	2s (abs)	Rho	$^{238}U/^{206}Pb$	2s (abs)	$^{207}Pb/^{206}Pb$	2s (abs)	Rho	$^{207}Pb/^{235}U$	2s (abs)	$^{206}Pb/^{238}U$	2s (abs)	U	Th	Pb	
GJ-1	0.809	0.013	0.09760	0.00100	0.54223	10.24590	0.104979	0.06017	0.0013	0.14056	601.8	7.6	600.0	5.9	398	11.22	23.40	100%
GJ-1	0.810	0.011	0.09754	0.00097	0.33581	10.25220	0.101955	0.06015	0.0013	0.34610	601.4	6.3	599.9	5.7	389	11.11	22.65	100%
GJ-1	0.811	0.011	0.09789	0.00099	0.38165	10.21555	0.103314	0.06006	0.0013	0.31190	602.4	6.4	602.0	5.8	371	10.68	23.30	100%
GJ-1	0.806	0.013	0.09740	0.00110	0.37944	10.26694	0.115951	0.06020	0.0014	0.26919	599.3	7.4	599.1	6.4	384	11.06	22.89	100%
GJ-1	0.814	0.016	0.09770	0.00100	0.28259	10.23541	0.104764	0.06030	0.0015	0.27691	603.9	8.9	600.7	6.1	385	11.03	23.00	99%
GJ-1	0.804	0.018	0.09750	0.00120	0.26690	10.25641	0.126233	0.06000	0.0017	0.25505	598.0	10.0	599.7	6.9	384	11.00	23.00	100%
GJ-1	0.810	0.020	0.09770	0.00140	0.25584	10.23541	0.146669	0.06010	0.0018	0.32080	603.0	11.0	600.6	8.1	384	10.98	23.00	100%
GJ-1	0.809	0.019	0.09750	0.00120	0.27513	10.25641	0.126233	0.06020	0.0017	0.26981	600.0	11.0	599.7	7.3	384	11.02	23.10	100%
GJ-1	0.805	0.017	0.09770	0.00110	0.24396	10.23541	0.115240	0.05990	0.0016	0.24452	597.4	9.8	600.9	6.4	384	11.01	23.00	101%
GJ-1	0.814	0.017	0.09730	0.00110	0.24824	10.27749	0.116190	0.06040	0.0016	0.29550	604.1	9.5	598.6	6.3	384	10.96	22.90	99%
Plešovice	0.3990	0.0094	0.0532	0.0011	0.45279	18.79699	0.388660	0.0549	0.0014	0.33288	340.5	7.0	334.2	6.6	809	63.0	68.6	98%
Plešovice	0.3890	0.0200	0.0538	0.0018	0.63125	18.58736	0.621882	0.0531	0.0017	0.38681	332.6	15.0	337.9	11.0	1019	80.6	92.9	102%
Plešovice	0.3856	0.0200	0.0521	0.0016	0.63890	19.19386	0.589447	0.0533	0.0017	0.29199	330.1	15.0	327.2	9.8	973	74.4	83.2	99%

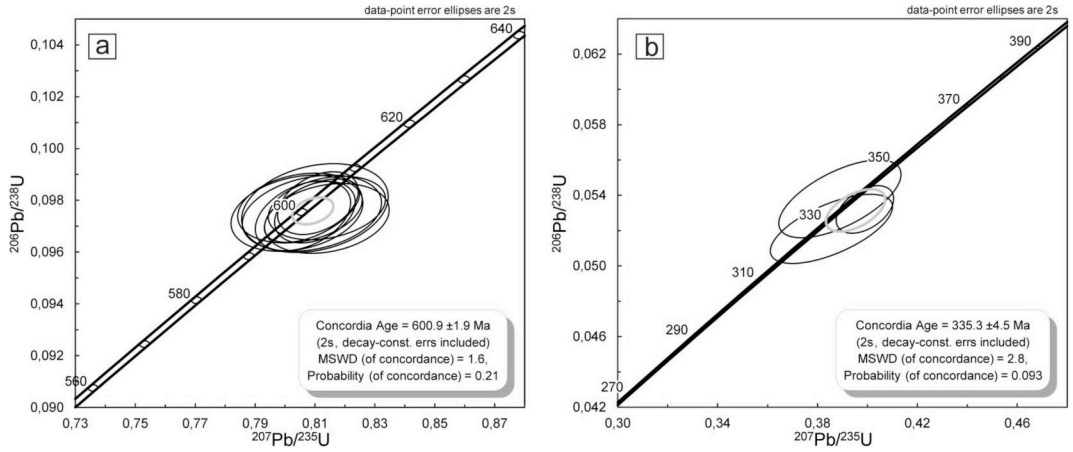

Fig. A.1. Conventional concordia diagrams from **a)** GJ-1 zircon standard (Jackson et al., 2004) for calibration, and **b)** Plešovice zircon (Sláma et al., 2008) as secondary standard.

Table A.4
Representative mineral analysis used for calculation of reactions in a quartz-biotitic schist

mineral	Biotite		Muscovite	Garnet				Plagioclase		
point	Bt 1	Bt 2	Ms 1	Grt 1	Grt 2	Grt 3	Grt 4	Pl 1	Pl 2	Pl 3
wt.%										
SiO_2	35,3	32,8	44.68	35.2	35.1	35.8	36.4	61.0	60.6	59.8
TiO_2	1.77	1.45	0.28	0.14	0.07	0.01	0.03	–	–	–
Al_2O_3	19.2	18.9	36.15	22.5	22.2	22.5	22.9	25.4	25.3	25.6
Cr_2O_3	–	–	–	0.01	0.02	0.02	0.02	–	–	–
FeO	18.2	18.8	2.46	28.6	28.9	28.7	28.3	0.07	0.03	0.05
MnO	0.14	0.19	0.02	8.35	8.42	8.42	8.83	–	–	–
MgO	11.6	12.1	0.55	3.99	3.89	3.90	3.88	0.06	0.03	0.02
CaO	0.04	0.01	0.01	1.14	1.19	1.40	1.42	6.38	6.39	6.39
BaO	0.25	0.15	0.64	–	–	–	–	0.09	0.04	0.00
Na_2O	0.26	0.25	1.30	0.05	0.07	0.03	0.02	7.79	7.74	7.73
K_2O	8.90	7.93	9.35	–	–	–	–	0.04	0.06	0.01
F	0.37	0.34	0.08	–	–	–	–	–	–	–
Cl	0.07	0.12	0.01	–	–	–	–	–	–	–
total	96.2	93.1	95.6	100.1	100.0	100.8	101.8	100.9	100.2	99.6
a.p.f.u.	x 24 oxygen equivalent			x 12 oxygen				x 8 oxygen		
Si	5.32	5.13	6.00	2.816	2.815	2.841	2.86	2.696	2.695	2.671
Al	3.41	3.50	5.71	2.124	2.102	2.103	2.12	1.324	1.327	1.350
Ti	0.20	0.17	0.03	0.008	0.004	0.001	0.00	–	–	–
Cr	–	–	–	0.001	0.001	0.001	0.00	–	–	–
Fe	2.23	2.46	0.27	1.913	1.940	1.908	1.86	0.003	0.001	0.002
Mn	0.02	0.02	0.00	0.565	0.571	0.566	0.59	–	–	–
Mg	2.60	2.82	0.11	0.475	0.465	0.462	0.45	0.004	0.002	0.001
Ca	0.01	0.00	0.00	0.098	0.102	0.119	0.12	0.302	0.304	0.306
Na	0.07	0.07	0.32	–	–	–	–	0.667	0.667	0.670
K	1.71	1.58	1.60	–	–	–	–	0.002	0.003	0.001
Ba	0.01	0.01	0.03	–	–	–	–	0.002	0.001	–
Cl	0.02	0.03	0.002	–	–	–	–	–	–	–
OH cal	3.81	3.80	3.97	–	–	–	–	–	–	–
F	0.18	0.17	0.032	–	–	–	–	–	–	–

End-members (mols%)

–	–	–	alm	62.70	63.04	62.46	61.5	an	31.06	31.21	31.33
–	–	–	py	15.57	15.10	15.12	15.1	ab	68.70	68.46	68.59
–	–	–	gr	3.20	3.31	3.88	3.94	or	0.24	0.33	0.08
–	–	–	sp	18.53	18.55	18.54	19.4		–	–	–

Tabla A.5
P-T results obtained from combinations between mineral analysis points in a quartz-biotitic schist

#	Analysis	P (MPa)	Sd (P)	T (°C)	sd (T)	Cor.	fit	RI
15	Bt 2 Ms 1 Grt 2 Pl 1	530	120	682	37	0.757	0.04	4

11	Bt 1 Ms 1 Grt 4 Pl 3	570	120	677	36	0.751	0.17	4
average of 24 combinations		550	120	680	37	0.753	0.22	4

Set of reactions represented in blue lines of Fig. 7e and f (abbreviations according to THERMOCALC)

2) 2pa + gr + 3q = 3an + 2 ab + $2H_2O$

3) 3aest + 6q = phl + 2mu + py

7) ann + 3an = mu + gr + alm

19) 3mu + 4pa + 2py + 3gr = 3east + 9an + 4 ab + $4H_2O$

#15: combination that uses analysis of the internal sector of the garnet and the biotite furthest away to this.

#11: combination that uses analysis of the external sector of garnet (diffusion) and of the biotite closest to it.

Fluids present in the calculation: $xH_2O = 0.9$; $xCO_2 = 0.1$

Appendix B. Supplementary data

Supplementary data to this article can be found online at https://doi.org/10.1016/j.jsames.2019.04.028.

References

Abdel-Rahman, A.F.M., 1994. Nature of biotites from alkaline, calc-alkaline, and peraluminous magmas. J. Petrol. 35 (2), 525–541.

Aceñolaza, F., Aceñolaza, G., 2005. La formación Puncoviscana y unidades estratigráficas vinculadas en el Neoproterozoico - Cámbrico Temprano del Noroeste Argentino. Lat. Am. J. Sedimentol. Basin Anal. 12 (2), 65–87.

Armas, P., Cristofolini, E.A., Otamendi, J.E., Tibaldi, A.M., Barzola, M.G., Camilletti, G.C., 2018. Geochronology and facies analysis of subaqueous volcanism of lower ordovician, Famatinian arc, Argentina. J. South Am. Earth Sci. 84, 255–265.

Astini, R.A., Dávila, F.M., 2004. Ordovician back arc foreland and Ocloyic thrust belt development on the western Gondwana margin as a response to Precordillera terrane accretion. Tectonics 23, TC4008. https://doi.org/10.1029/2003TC001620.

Bahlburg, H., 1998. The geochemistry and provenance of Ordovician turbidites in the Argentine Puna. In: In: Pankhurst, R.J., Rapela, C.W. (Eds.), The Proto-Andean Margin of Gondwana, vol. 142. Geological Society. London, Special Publication, pp. 127–142.

Baier, J., Audétat, A., Keppler, H., 2008. The origin of the negative niobium tantalum anomaly in subduction zone magmas. Earth Planet. Sci. Lett. 267, 290–300.

Baldo, E., Rapela, C.W., Pankhurst, R.J., Galindo, C., Casquet, C., Verdecchia, S., Murra, J., 2014. Geocronología de las Sierras de Córdoba: revisión y comentarios. In: Relatorio del XIX Congreso Geológico Argentino: Geología y Recursos Naturales de la Provincia de Córdoba, pp. 845–868.

Barbosa, E.S.R., Brod, J.A., Junqueira-Brod, T.C., Dantas, E.L., Cordeiro, P.F.D.O., Gomide, C.S., 2012. Bebedourite from its type area (Salitre I complex): a key petrogenetic series in the Late-Cretaceous Alto Paranaíba kamafugite carbonatite-phoscorite association, Central Brazil. Lithos 144, 56–72.

Batchelor, R., Bowden, P., 1985. Petrogenetic interpretation of granitoid rock series using multicationic parameters. Chem. Geol. 48, 43–55.

Bellos, L., Castro, A., Díaz-Alvarado, J., Toselli, A., 2015. Multi-pulse cotectic evolution and in-situ fractionation of calc-alkaline tonalite–granodiorite rocks, Sierra de Velasco batholith, Famatinian belt, Argentina. Gondwana Res. 27 (1), 258–280.

Boynton, W.V., 1984. Cosmochemistry of the rare earth elements: meteorite studies. In: Henderson, P. (Ed.), Rare Earth Element Geochemistry. Elsevier, Amsterdam, pp. 63–114.

Brogioni, N., 1994. Petrología de la faja de rocas máficas y ultramáficas de la Sierra de San Luis, Argentina. 7° Congreso Geológico Chileno, Actas 2, 967–971 (Concepción, Chile).

Brogioni, N., Parrini, P., Pecchioni, E., 2005. Petrología del magmatismo de arco predeformacional en el cordón del Realito y la zona norte del Plutón La Escalerilla. Sierra de San Luis. Rev. Asoc. Geol. Argent. 60 (3) 495-412.

Caminos, R., 1979. Sierras Pampeanas noroccidentales. Salta, Tucumán, Catamarca, La Rioja y san juan. In: En, Turner, J.C.M. (Eds.), Geología Regional Argentina. Academia Nacional de Ciencias, Córdoba, pp. 225–291.

Carugno Durán, A., 1998. Geología y petrografía de la Sierra de Socoscora. Provincia de San Luis. República Argentina. 2° Congreso Uruguayo de Geología, Punta del Este, pp. 108–112.

Castro, A., 2001. Plagioclase morphologies in assimilation experiments. Implications for disequilibrium melting in the generation of granodiorite rocks. Mineral. Petrol. 71, 31–49.

Castro, A., 2013. Tonalite-granodiorite suites as cotectic systems: a review of experimental studies with applications to granitoid petrogenesis. Earth Sci. Rev. 124, 68–95.

Chapman, J.B., Ducea, M.N., DeCelles, P.G., Profeta, L., 2015. Tracking changes in crustal thickness during orogenic evolution with Sr/Y: an example from the North American Cordillera. Geology 43 (10), 919–922.

Chernicoff, C., Zappettini, E., Santos, J., Allchurch, S., McNaughton, N., 2010. The southern segment of the Famatinian magmatic arc, La Pampa province, Argentina. Gondwana Res. 17, 662–675.

Chiaradia, M., 2015. Crustal thickness control on Sr/Y signatures of recent arc magmas: an Earth scale perspective. Sci. Rep. 5, 8115. https://doi.org/10.1038/srep08115.

Cisterna, C.E., Coira, B., 2014. Subaqueous eruption-fed mass-flow deposits: records of the Ordovician arc volcanism in the Northern Famatina Belt; Northwestern Argentina. J. South Am. Earth Sci. 49, 73–84.

Claeson, D.T., Meurer, W.P., 2004. Fractional crystallization of hydrous basaltic “arc-type” magmas and the formation of amphibole-bearing gabbroic cumulates. Contrib. Mineral. Petrol. 147, 288–304.

Coira, B., Kay, S.M., Pérez, B., Woll, B., Hanning, M., Flores, P., 1999. Magmatic sources and tectonic setting of Gondwana margin Ordovician magmas, northern Puna of Argentina and Chile. In: In: Ramos, V., Keppie, J. (Eds.), Laurentia-Gondwana Connections before Pangea, vol. 336. Geological Society of America Special Paper, pp. 145–170.

Coira, B., Koukharsky, M., Ribeiro Guevara, S., Cisterna, C., 2009. Puna (Argentina) and northern Chile Ordovician Basic magmatism: a contribution to the tectonic setting. J. South Am. Earth Sci. 27, 24–35.

Collo, G., Astini, R., Cawood, P.A., Buchan, C., Pimentel, M., 2009. U–Pb detrital zircon ages and Sm-Nd isotopic features in low-grade metasedimentary rocks of the Famatina belt: implications for late Neoproterozoic–early Palaeozoic evolution of the proto-Andean margin of Gondwana. J. Geol. Soc. 166, 303–319.

Cristofolini, E., Otamendi, J., Ducea, M., Peason, D., Tibaldi, A., Baliani, I., 2012. Detrital zircon U-Pb ages of metasedimentary rocks from the Sierra de Valle Fértil: revealing entrapment of late Cambrian marine successions into the deep roots of the early Ordovician Famatinian Arc. J. South Am. Earth Sci. 37, 77–94.

Cristofolini, E., Otamendi, J., Walker Jr., B., Tibaldi, A., Armas, P., Bergantz, G., Martino, R., 2014. A middle paleozoic shear zone in the sierra de Valle Fértil, Argentina: records of a continent-arc collision in the famatinian margin of Gondwana. J. South Am. Earth Sci. 56, 170–185.

Cristofolini, E., Barzola, M., Otamendi, J., Tibaldi, A., Morosini, A., Armas, P., Camilletti, G., 2017. Caracterización petrológica y geoquímica de las rocas plutónicas de la Sierra de La Aguada, Provincia de San Luis, Argentina: implicaciones genéticas con el arco magmático Famatiniano. Estud. Geol. 73 (1), e065. https://doi.org/10.3989/egeol.42711.440.

Dahlquist, J.A., Rapela, C.W., Pankhurst, R.J., Baldo, E., Saavedra, J., Alasino, P.H., 2005. Los granitoides de la sierra de Chepes y su comparación con granitoides paleozoicos de las Sierras Pampeanas: implicancias para el orógeno famatiniano. In: In: Dahlquist, J.A., Baldo, E.G., Alasino, P.H. (Eds.), Geología de la provincia de La Rioja, Precámbrico-Paleozoico Inferior. Asociación Geológica Argentina, Serie D, vol. 8. Publicación Especial, pp. 87–108.

Demartis, M., Jung, S., Berndt, J., Aragón, E., Sato, A.M., Radice, S., Maffini, M.N., Coniglio, J.E., Pinotti, L.P., D'Eramo, F.J., Agulleiro Insúa, L.A., 2017. Famatinian inner arc: petrographical observations and geochronological constraints on pegmatites and leucogranites of the Comechingones pegmatitic field (Sierras de Córdoba, Argentina). J. South Am. Earth Sci. 79, 239–253.

De Paolo, J., 1981. Trace element and isotopic effects of combined wall-rock assimilation and fractional crystallization. Earth Planet. Sci. Lett. 53, 189–202.

Dolivo-Dobrovolsky, D., 2012-2013. TriQuick©. Personal web-pages. http://www.dimadd.ru/en/content/triquick.

Dolivo-Dobrovolsky, D., 2015. TC_Comb© v1.1. Personal web-pages. http://www.dimadd.ru/en/Programs/tccomb.

Drobe, M., López de Luchi, M.G., Steenken, A., Frei, R., Naumann, R., Wemmer, K., Siegesmund, S., 2009. Provenance of the late proterozoic to early Cambrian metaclastic sediments of the sierra de San Luis (eastern sierras Pampeanas) and Cordillera oriental, Argentina. J. South Am. Earth Sci. 28, 239–262.

Drobe, M., López de Luchi, M.G., Steenken, A., Wemmer, K., Naumann, R., Frei, R., Siegesmund, S., 2011. Geodynamic evolution of the eastern sierras Pampeanas (central Argentina) based on geochemical, Sm–Nd, Pb–Pb and SHRIMP data. Int. J. Earth Sci. 100, 631–657.

Ducea, M.N., Otamendi, J.E., Bergantz, G., Stair, K.M., Valencia, V.A., Gehrel, G.E., 2010. Timing constraints on building an intermediate plutonic arc crustal section: U-Pb zircon geochronology of the Sierra Valle F_ertileLa Huerta, Famatinian arc, Argentina. Tectonics 29, TC4002. https://doi.org/10.1029/2009TC002615.

Ducea, M.N., Otamendi, J.E., Bergantz, G.W., Jianu, D., Petrescu, L., 2015. The origin and petrologic evolution of the Ordovician Famatinian-Puna arc. In: In: DeCelles, P.G., Ducea, M.N., Carrapa, B., Kapp, P.A. (Eds.), Geodynamics of a Cordilleran Orogenic System: the Central Andes of Argentina and Northern Chile, vol. 212. Geological Society of America Memoir, pp. 125–138.

El Bouseily, A.M., El Sokkary, A.A., 1975. The Relation between Rb, Ba y Sr in granitic rocks. Chem. Geol. 16 (3), 207–219.

Elliott, T., Plank, T., Zindler, A., White, W., Bourdon, B., 1997. Element transport from slab to volcanic front at the Mariana arc. J. Geophys. Res.-Solid Earth 102, 14991–15019.

Ferracutti, G., Bjerg, E., Mogessie, A., 2007. Metales base y preciosos en Las Águilas,

Sierra de San Luis: Mineralogía, génesis y evolución. Rev. Asoc. Geol. Argent. 62 (3), 434–446.
Ferracutti, G., Bjerg, E., Hauzenberger, C., Mogessie, A., Cacace, F., Asiain, L., 2017. Meso to Neoproterozoic layered mafic-ultramafic rocks from the Virorco back-arc intrusion, Argentina. J. South Am. Earth Sci. 79, 489–506.
Frost, B.R., Barnes, C.G., Collins, W.J., Arculus, R.J., Ellis, D.J., Frost, C.D., 2001. A geochemical classification for granitic rocks. J. Petrol. 42 (11), 2033–2048.
Galliski, M.A., 1994. La Provincia Pegmatítica Pampeana. I. Tipología y distribución de sus distritos económicos. Revista Asociación Geológica Argentina 49, 99–112.
González, P., Sato, A., Llambías, E., 2002. The komatiites and associated mafic to ultramafic metavolcanic rocks of western Sierra de San Luis. Actas 15° Congreso Geológico Argentino (El Calafate) 2, 87–90 (Buenos Aires).
González, P., Sato, A., Llambías, E., Vlach, S., 2004. Early paleozoic structural and metamorphic evolution of western sierra de San Luis (Argentina), in relation to Cuyania accretion. Gondwana Res. 7 (4), 1157–1170.
Goscombe, B., Gray, D., Carson, C., Groenewald, B., Scrimgeour, I., 2005. Classification of metamorphic gradients and their utilization as indicators of tectonic regimes. In: Geological Society of Australia, Specialist Group in Tectonics and Structural Geology, Conference Abstracts, Townsville.
Grosse, P., Bellos, L., Camilo, R., Larrovere, M., Rossi, J., Toselli, A., 2011. Across-arc variation of the Famatinian magmatic arc (NW Argentina) exemplified by I-, S-and transitional I/S-type Early Ordovician granitoids of the Sierra de Velasco. J. South Am. Earth Sci. 32 (1), 110–126.
Hauzenberger, C., Mogessie, A., Hoinkes, G., Felfernig, A., Bjerg, E., Kostadinoff, J., Delpino, S., Dimieri, L., 2001. Metamorphic evolution of the Sierras de San Luis, Argentina: granulites facies metamorphism related to mafic intrusions. Mineral. Petrol. 71, 95–126.
Hawthorne, F.C., Oberti, R., Harlow, G.E., Maresch, W.V., Martin, R.F., Schumacher, J.C., Welch, M.D., 2012. Nomenclature of the amphibole supergroup. Am. Mineral. 97 (11–12), 2031–2048.
Hermann, J., Spandler, C., Hack, A., Korsakov, A., 2006. Aqueous fluids and hydrous melts in high-pressure and ultra-high pressure rocks: implications for element transfer in subduction zones. Lithos 92, 399–417.
Hibbard, M.J., 1995. Petrography to Petrogenesis. Prentice Hall, Englewood Cliffs, New Jersey.
Holland, T., Blundy, J., 1994. Non-ideal interactions in calcic amphiboles and their bearing on amphibole-plagioclase thermometry. Contrib. Mineral. Petrol. 116, 433–447.
Holland, T., Powell, R., 1998. An internally consistent thermodynamic data set for phases of petrological interest. J. Metamorph. Geol. 16, 309–343.
Hongn, F.D., Tubía, J.M., Esteban, J.J., Aranguren, A., Vega, N., Sergeev, S., Larionov, A., Basei, M., 2014. The Sierra de Cachi (Salta, NW Argentina): geological evidence about a Famatinian retro-arc at mid crustal levels. J. Iber. Geol. 40 (2), 225–240.
Hutton, D.H.W., 1996. The “space problem” in the emplacement of granite. Episodes 19 (4), 114–119.
Irvine, T.M., Baragar, W.R., 1971. A guide to the chemical classification of common volcanic rocks. Can. J. Earth Sci. 8, 523–548.
Jackson, S.E., Pearson, N.J., Griffin, W.L., Belousova, E.A., 2004. The application of laser ablation–inductively coupled plasma–mass spectrometry to in situ U-Pb zircon geochronology. Chem. Geol. 211, 47–69.
Kelemen, P.B., Hanghøj, K., Greene, A.R., 2003. One view of the geochemistry of subduction-related magmatic arcs, with emphasis on primitive andesite and lower crust. In: In: Holland, H.D., Turekian, K.K. (Eds.), Treatise on Geochemistry, vol. 3. Elsevier-Pergamon, Oxford, pp. 596–659 Rudnick, R. (Ed.), The Crust.
Kleine, T., Mezger, K., Zimmermann, U., Münker, C., Bahlburg, H., 2004. Crustal evolution along the Early Ordovician Proto-Andean margin of Gondwana: trace element and isotope evidence from the complejo igneo Pocitos (Northwestern Argentina). J. Geol. 112, 503–520.
Larrovere, M.A., de los Hoyos, C.R., Toselli, A.J., Rossi, J.N., Basei, M.A.S., Belmar, M.E., 2011. High T/P evolution and metamorphic ages of the migmatitic basement of northern Sierras Pampeanas, Argentina: characterization of a mid-crustal segment of the Famatinian belt. J. South Am. Earth Sci. 31 (2–3), 279–297.
Le Maitre, R.W., 2002. Igneous Rocks a Classification and Glossary of Terms Recommendations of the International Union of Geological Sciences, Sub-commission on the Systematics of Igneous Rocks. Cambridge University Press, pp. 236.
Llambías, E., Sato, A.M., Ortiz Suárez, A., Prozzi, C., 1998. The granitoids of the sierra de San Luis. Geological society of London. Special publication Nº 142. In: In: Pankhurst, R.J., Rapela, C.W. (Eds.), The Proto-Andean Margin of Gondwana, vol. 142. Geological Society, London, Special Publication, pp. 325–341.
Locock, A.J., 2014. An Excel spreadsheet to classify chemical analyses of amphiboles following the IMA 2012 recommendations. Comput. Geosci. 62, 1–11.
López de Luchi, M.G., Cerredo, M.E., Siegesmund, S., Steenken, A., Wemmer, K., 2003. Provenance and tectonic setting of the protoliths of the metamorphic complexes of sierra de San Luis. Rev. Asoc. Geol. Argent. 58 (4), 525–540.
López de Luchi, M.G., Siegesmund, S., Wemmer, K., Steenken, A., Naumann, R., 2007. Geochemical constraints on the petrogenesis of the paleozoic granitoids of the sierra de San Luis, sierras Pampeanas, Argentina. J. South Am. Earth Sci. 24, 138–166.
Lucassen, F., Franz, G., 2005. The early Palaeozoic orogen in the Central Andes: a non-collisional orogen comparable to the Cenozoic high plateau? In: In: Vaughan, A., Leat, P., Pankhurst, R. (Eds.), Terrane Processes at the Margins of Gondwana, vol. 246. Geological Society of London Special Publication, pp. 257–373.
Ludwig, K.R. (Ed.), 2003. Isoplot 3.00, vol. 4. Berkeley Geochronology Center, California, pp. 0–70 (Special Publication).
Mannhein, R., Miller, H., 1996. Las rocas volcánicas y subvolcánicas eopaleozoicas del Sistema de Famatina. In: In: Aceñolaza, F.G., Miller, H., Toselli, A. (Eds.), Geología del Sistema de Famatina A19. Münchner Geologische Hefte, Münchner, pp. 159–186.
Martino, R.D., Guereschi, A.B., Sfragulla, J.A., 2009. Petrology, structure and tectonic significance of the Tuclame banded schists in the Sierras Pampeanas of Córdoba and its relationship with the metamorphic basement of northwestern Argentina. J. South Am. Earth Sci. 27, 280–298.
Meinhold, G., Kostopoulos, D., Frei, D., Himmerkus, F., Reischmann, T., 2010. U–Pb LASF-ICP–MS zircon geochronology of the Serbo-Macedonian Massif, Greece: palaeotectonic constraints for Gondwana-derived terranes in the Eastern Mediterranean. Int. J. Earth Sci. 99, 813–832.
Miyashiro, A., 1974. Volcanic rock series in island arcs and active continental margins. Am. J. Sci. 274, 321–355.
Mogessie, A., Hauzenberger, Ch, Hoinkes, G., Felfernig, A., Stumpfl, E.F., Bjerg, E.A., Kostadinoff, J., 2000. Genesis of platinum group minerals in the Las Águilas mafic-ultramafic rocks, San Luis Province, Argentina: textural, chemical and mineralogical evidence. Mineral. Petrol. 68, 85–114.
Morosini, A., 2011. El Granito La Escalerilla, Provincia de San Luis. Ph.D. thesis. Universidad Nacional de San Luis, pp. 434 (unpublished).
Morosini, A., Ortiz Suárez, A., 2015. Propuesta de clasificación del magmatismo Ordovícico en la Sierra de San Luis. In: 3° Simposio de Petrología Ígnea y Metalogénesis Asociada. General Roca, Río Negro, Actas 124-125.
Morosini, A., Ortiz Suárez, A., Ramos, G., 2009. Los Granitoides Famatinianos del sector suroccidental de la Sierra de San Luis: Clasificación y Geotermometría. Rev. Asoc. Geol. Argent. 64 (3), 253–266.
Morosini, A., Ortiz Suárez, A., Otamendi, J., Pagano, D., Ramos, G., 2017. La Escalerilla pluton, San Luis Argentina: the orogenic and post-orogenic magmatic evolution of the famatinian cycle at Sierras de San Luis. J. South Am. Earth Sci. 73, 100–118.
Mulcahy, S.R., Roeske, S.M., McClelland, W.C., Ellis, J.R., Jourdan, F., Renne, P.R., Vujovich, G.I., 2014. Multiple migmatite events and cooling from granulite facies metamorphism within the Famatina arc margin of northwest Argentina. Tectonics 33. https://doi.org/10.1002/2013TC003398.
Oberti, R., Cannillo, E., Toscani, G., 2012. How to name amphiboles after the IMA2012 report: rules of thumb and a new PC program for monoclinic amphiboles. Period. Mineral. 81 (2), 257–267.
Ortiz Suárez, A., 1988. El basamento de Las Aguadas, provincia de San Luis. Rev. Asoc. Argent. Mineral. Petrol. Sedimentol. 19 (1–4), 13–24.
Ortiz Suárez, A., Prozzi, C., Llambías, E., 1992. Geología de la parte Sur de la Sierra de San Luis y granitoides asociados, Argentina. Revista de estudios geológicos 48, 269–277 (Madrid).
Ortiz Suárez, A., Ulacco, H., Zaccarini Garuti, F., Garuti, G., 2001. Sperrylite from Sulfides of Las Cañas (Sierra de San Luis): the Second Argentinian occurrence. VII Congreso Argentino de Geología Económica, Salta, Actas1, pp. 169–172.
Ortiz Suárez, A., Morosini, A., Ulacco, H., Carugno Durán, A., 2012. Geología y geofísica del cuerpo máfico-ultramáfico Las Cañas, Provincia de San Luis. Ser. Correlación Geol.: Aporte al magmatismo y metalogénesis asociada de la República Argentina II 28 (2), 151–166.
Otamendi, J.E., Tibaldi, A.M., Vujovich, G.I., Viñao, G.A., 2008. Metamorphic evolution of migmatites from the deep famatinian arc crust exposed in sierras Valle Fértil–La Huerta, san juan, Argentina. J. South Am. Earth Sci. 25, 313–335.
Otamendi, J.E., Vujovich, G.I., de la Rosa, J.D., Castro, A., Tibaldi, A., Martino, R., Pinotti, L., 2009. Geology and petrology of a deep crustal zone the famatinian paleoarc, sierras Valle Fértil – La Huerta, san juan, Argentina. J. South Am. Earth Sci. 27, 258–279.
Otamendi, J.E., Cristofolini, E.A., Tibaldi, A.M., Quevedo, F.I., Baliani, I., 2010. Petrology of mafic and ultramafic layered rocks from the Jaboncillo Valley, Sierra de Valle Fértil, Argentina: implications for the evolution of magmas in the lower crust of the Famatinian arc. J. South Am. Earth Sci. 29, 685–704.
Otamendi, J.E., Ducea, M., Bergantz, G., 2012. Geological, petrological and geochemical evidence for progressive construction of an arc crustal section, Sierra de Valle Fertil, Famatinian Arc, Argentina. J. Petrol. 53 (4), 761–800.
Otamendi, J.E., Ducea, M.N., Cristofolini, E.A., Tibaldi, A.M., Camilletti, G.C., Bergantz, G.W., 2017. U-Pb ages and Hf isotope compositions of zircons in plutonic rocks from the central Famatinian arc, Argentina. J. South Am. Earth Sci. 76, 412–426.
Pankhurst, R.J., Rapela, C.W., Saavedra, J., Baldo, E., Dahlquist, J., Pascua, I., Fanning, C.M., 1998. The Famatinian magmatic arc in the central Sierras Pampeanas: an Early to Mid-Ordovician continental arc on the Gondwana margin. In: In: Pankhurst, R., Rapela, C. (Eds.), The Proto-Andean Margin of Gondwana, vol. 142. Geological Society of London, Special Publications, London, pp. 343–367.
Patiño Douce, A.E., Beard, J.S., 1995. Dehydration melting of biotite gneiss and quartz amphibolite from 3 to 15 kbar. J. Petrol. 36, 707–738.
Paton, C., Hellstrom, J., Paul, B., Woodhead, J., Hergt, J., 2011. Iolite: freeware for the visualization and processing of mass spectrometric data. J. Anal. Atom. Spectrosc 26, 2508–2518.
Pearce, J.A., 1982. Trace element characteristics of lavas from destructive plate boundaries. In: Thorpe, R.S. (Ed.), Andesites. John Wiley, pp. 525–548.
Pearce, J.A., Harris, N.W., Tindle, A.G., 1984. Trace element discrimination diagrams for the tectonic interpretation of granitic rocks. J. Petrol. 25, 956–983.
Pearce, J.A., 1996. A user's guide to basalt discrimination diagrams. In: In: Wyman, D.A. (Ed.), Trace Element Geochemistry of Volcanic Rocks: Applications for Massive Sulphide Exploration, Geological Association of Canada, Short Course Notes, vol. 12. pp. 79–113.
Peccerillo, A., Taylor, S.R., 1976. Geochemistry of Eocene calc-alkaline volcanic rocks from the Kastamonu area, Northern Turkey. Contrib. Mineral. Petrol. 58, 63–81.
Petrus, J.A., Kamber, B.S., 2012. VizualAge: a novel approach to laser ablation ICP-MS U-Pb geochronology data reduction. Geostand. Geoanal. Res. 36, 247–270.
Poma, S., Quenardelle, S., Litvak, V., Maisonnave, E.B., Koukharsky, M., 2004. The sierra de Macon, plutonic expression of the ordovician magmatic arc, salta province Argentina. J. South Am. Earth Sci. 16 (7), 603–613.

Powell, R., Holland, T.J.B., 1988. An Internally consistent dataset with uncertainties and correlations; 3, Applications to geobarometry, worked examples and a computer program. J. Metamorph. Geol. 6, 173–204.
Prozzi, C., y Ramos, G., 1988. La formación San Luis. I Jornadas de Trabajo de Sierras Pampeanas. San Luis. Actas 1, San Luis.
Putirka, K., 2016. Amphibole thermometers and barometers for igneous systems and some implications for eruption mechanisms of felsic magmas at arc volcanoes. Am. Mineral. 101, 841–858.
Ramos, V.A., 2004. Cuyania, an exotic block to Gondwana: review of a historical success and the present problems. Gondwana Res. 7, 1009–1026.
Rapela, C.W., Verdecchia, S.O., Casquet, C., Baldo, E.,G., Galindo, C., Murra, J.A., Dahlquist, J.A., 2015. Identifying Laurentian and SW Gondwana sources in the neoproterozoic to early paleozoic metasedimentary rocks of the sierras Pampeanas: paleogeographic and tectonic implications. Gondwana Res. 32, 193–212.
Rapela, C.W., Coira, B., Toselli, A.J., Saavedra, J.E., 1992. The lower paleozoic magmatism of southwestern Gondwana and the evolution of the famatinian orogen. Int. Geol. Rev. 34, 1081–1142.
Ridolfi, F., Renzulli, A., Puerini, M., 2010. Stability and chemical equilibrium of amphibole in calc-alkaline magmas: an overview, new thermobarometric formulations and application to subduction-related volcanoes. Contrib. Mineral. Petrol. 160 (1), 45–66.
Roeder, P.L., Emslie, R.F., 1970. Olivine-liquid equilibrium. Contrib. Mineral. Petrol. 29, 275–289.
Roquet, M.B., 2010. Mineralogía, geoquímica tipología y relación con los granitoides de las pegmatitas del grupo Villa Praga-Las Lagunas, distrito Conlara, sierra de San Luis. Universidad Nacional de Córdoba, pp. 439 (unpublished) Ph.D. thesis.
Rossi, N., 1966. Distrito Pegmatítico Conlara, Provincia de San Luis. Dirección Nacional de Geología y Minería, Buenos Aires, pp. 171 (unpublished).
Sato, A.M., Ortiz Suárez, A., Llambías, E., Cavarozzi, C., Sánchez, V., Varela, R., Prozzi, C., 1996. Los plutones pre-oclóyicos de la Sierra de San Luis: arco magmático al inicio del ciclo famatiniano. XIII Congreso Geológico Argentino y III Congreso de Exploración de Hidrocarburos, Actas V, Buenos Aires, pp. 259–272.
Sato, A.M., González, P.D., Llambías, E.J., 2003. Evolución del orógeno Famatiniano en la Sierra de San Luis: magmatismo de arco, deformación y metamorfismo de bajo a alto grado. Rev. Asoc. Geol. Argent. 58 (4), 487–504.
Schwartz, J.J., Gromet, L.P., Miro, R., 2008. Timing and duration of the calc-alkaline arc of the pampean orogeny: implications for the late neoproterozoic to Cambrian evolution of western Gondwana. J. Geol. 116 (1), 39–61.
Shand, S.J., 1943. Eruptive Rocks. Their Genesis, Composition, Classification, and Their Relation to Ore Deposits with a Chapter on Meteorite, second ed. John Wiley & Sons, New York, NY, pp. 1–444.
Siegesmund, S., Steenken, A., Martino, R.D., Wemmer, K., López de Luchi, M.G., Frei, R., Guereschi, A., 2010. Time constraints on the tectonic evolution of the eastern sierras Pampeanas (central Argentina). Int. J. Earth Sci. 99 (6), 1199–1226.
Sims, J., Ireland, T., Camacho, A., Lyons, P., Pieters, P., Skirrow, R., Stuart-Smith, P., Miró, R., 1998. U-Pb, Th-Pb and Ar-Ar geochronology from the southern Sierras Pampeanas, Argentina: implications for the Paleozoic tectonic evolution of the western Gondwana margin. In: In: Pankhurst, R.J., Rapela, C.W. (Eds.), The Proto-Andean Margin of Gondwana, vol. 142. Geological Society. London, Special Publication, pp. 256–281.
Sláma, J., Košler, J., Condon, D.J., Crowley, J.I., Gerdes, A., Hanchar, J.M., Horstwood, M.S.A., 2008. Plešovice zircon: a new natural reference material for U-Pb and Hf isotopic microanalysis. Chem. Geol. 249, 1–35.
Steenken, A., Siegesmund, S., Lopez de Luchi, M.G., Frei, R., Wemmer, K., 2006. Neoproterozoic to early palaeozoic events in the sierra de San Luis: implications for the famatinian geodynamics in the eastern sierras Pampeanas (Argentina). J. Geol. Soc. 163, 965–982.
Steenken, A., López de Luchi, M.G., Martínez Dopico, C., Drobe, M., Wemmer, K., Siegesmund, S., 2010. The neoproterozoic-early paleozoic metamorphic and magmatic evolution of the eastern sierras Pampeanas: an overview. Int. J. Earth Sci. 1–24. https://doi.org/10.1007/s00531-010-0624-0.
Steenken, A., López de Luchi, M.G., Martínez Dopico, C., Drobe, M., Wemmer, K., Siegesmund, S., 2011. The neoproterozoic-early paleozoic metamorphic and magmatic evolution of the eastern sierras Pampeanas: an overview. In: In: Siegesmund, S., Basei, M., Oyhantcabal, P. (Eds.), Multiaccretional Tectonics at the Rio de La Plata Margins. International Journal Earth Sciences, vol. 100. pp. 465–488 2.
Streck, M.J., 2008. Mineral textures and zoning as evidence for open system processes. Rev. Mineral. Geochem. 69 (1), 595–622.
Sun, S.S., McDonough, W., 1989. Chemical and isotopic systematics of oceanic basalts: implications for mantle composition and processes. In: Geological Society, London, Special Publications, vol. 42. pp. 313–345 1.
Thomas, W.A., Astini, R.A., 1996. The Argentine precordillera: a traveler from the Ouachita embayment of North American Laurentia. Science 273 (5276), 752–757.
Thomas, W.A., Astini, R.A., Mueller, P.A., McClelland, W.C., 2015. Detrital-zircon geochronology and provenance of the Ocloyic synorogenic clastic wedge, and Ordovician accretion of the Argentine Precordillera terrane. Geosphere 11, 1749–1769.
Tibaldi, A.M., Otamendi, J.E., Cristofolini, E.A., Baliani, I., Walker Jr., B.A., Bergantz, G.W., 2013. Reconstruction of the Early Ordovician Famatinian arc through thermobarometry in lower and middle crustal exposures, Sierra de Valle Fértil, Argentina. Tectonophysics 589, 151–166.
Tunheng, A., Hirata, T., 2004. Development of signal smoothing device for Laser Ablation-ICP-mass spectrometer. J. Anal. At. Spectrom. 19, 932–934.
Turner, J.C., 1960. Estratigrafía de la Sierra de Santa Victoria y adyacencias. Bol. Acad. Nac. Cienc. Córdoba 42, 163–206.
von Gosen, W., Loske, W., Prozzi, C., 2002. New isotopic dating of intrusive rocks in the Sierra de San Luis (Argentina): implications for the geodinamic history of the Eastern Sierras Pampeanas. J. South Am. Earth Sci. 15, 237–250.
Viramonte, J.M., Becchio, R., Viramonte, J., Pimentel, M., Martino, R., 2007. Ordovician igneous and metamorphic units in southeastern Puna: new U-Pb and Sm-Nd data and implications for the evolution of northwestern Argentina. J. South Am. Earth Sci. 24, 167–183.
Wager, L., Brown, G., Wadsworth, W., 1960. Types of igneous cumulates. J. Petrol. 1, 73–85.
Whitmeyer, S.J., Simpson, C., 2004. Regional deformation of the sierra de San Luis, Argentina: implications for the paleozoic development of western Gondwana. Tectonics 23, 1–16. https://doi.org/10.1029/2003TC001542.
Whitney, D.L., Evans, B.W., 2010. Abbreviations for names of rock-forming minerals. Am. Mineral. 95, 185–187.
Whitney, J.A., Stormer, J.C., 1977. The distribution of NaAlSi3O8 between coexisting microcline and plagioclase and its effect on geothermometric calculations. Am. Mineral. 62, 687–691.